NASS
NAN YANG ACADEMY OF SCIENCES

SUSTAINABLE MARINE STRUCTURES

Volume 3·Issue 1·January 2021 ISSN 2661-3158(Online)

AOSCI Asia-Pacific Science Citation Index · creative commons · CNKI 中國知網 www.cnki.net 中国知识基础设施工程 · Google scholar · Crossref · MyScienceWork

NASS
NAN YANG ACADEMY OF SCIENCES

Editorial Board

Editor-in-Chief

Associate Editors

Editorial Board Member

ISSN: 2661-3158 (Online)
Volume 3 Issue 1 January 2021

SUSTAINABLE MARINE STRUCTURES

Editor-in-Chief
S. Surendran
IIT Madras, India

NASS
NAN YANG ACADEMY OF
SCIENCES (SINGAPORE)

NASS
NAN YANG ACADEMY OF SCIENCES

Volume 3 | Issue 1 | January 2021 | Page 1-55
Sustainable Marine Structures

Contents

ARTICLE

Sustainable Marine Structures
http://ojs.nassg.org/index.php/sms/index

ARTICLE

Analyzing Potential Water Harvesting from Atmosphere in Near Coastal Area

Ida Bagus Mandhara Brasika[1,2*] **Putra Bagus Panji Pamungkas**[2]

1. Department of Marine Sciences, Universitas Udayana, Jl. Raya Kampus Unud, Jimbaran, Kuta Selatan, Badung, Bali, 80361, Indonesia
2. Center of Remote Sensing and Ocean Science (CReSOS), Universitas Udayana, Jl. P.B. Sudirman, Denpasar, Bali, 80234, Indonesia

ARTICLE INFO

Article history
Received: 26 April 2021
Accepted: 18 May 2021
Published Online: 30 May 2021

Keywords:
Water scarcity
Intrusion
Water vapor density
Atmospheric water generator

ABSTRACT

Water is a basic need. However there are many near coastal regions which have very limited access to fresh water. The water in area close to coastal is mainly affected by ocean, indirectly by weather/climate conditions and directly from seawater intrusion. While abundant fresh water is actually available in the atmosphere in the form of moisture. Recent technology, such as Atmospheric Water Generator (AWG), is a possible solution to gain water from our atmosphere. However, comprehensive study is needed to understand the potential water harvesting in our atmosphere. Here, we examine the water availability in the atmosphere based on several parameters like temperature and humidity. The data are collected from observation using WS1040 Automatic Weather Station in a year of 2020 with a half-hour interval. Then, we calculate the availability of water content during each season, especially in dry conditions. We also simulate the water harvesting to fulfil daily basic need of fresh water. The atmospheric parameters have shown a monsoonal pattern. Water content decrease in atmosphere during the dry season but the water deficit occurs after the dry season. Although water harvesting able to supply daily freshwater need, it is not recommended to be a single source as it requires massive water storage and high-efficient AWG.

1. Introduction

Water scarcity or drought is a growing issue in many regions. There is no standard for drought definition [1], but in general drought is the dry condition longer than normal and causes the availability of water below the need [2]. There are more than 4.3 billion people or 71% of the global population living under conditions of moderate to severe water scarcity at least 1 month of the year [3]. The report from the World Economic Forum stated that water crises as the largest global risk in terms of potential impact [4]. The water scarcity might be caused by the high demand or limited access of water.

In the case of Bali, the water crisis is dominantly caused by the conflict of different user groups [5]. The factor of growing tourism has a significant role. However, some areas like Karangasem (East Bali) have limited ac-

---

**Corresponding Author:*
Ida Bagus Mandhara Brasika,
Department of Marine Sciences & Center of Remote Sensing and Ocean Science (CReSOS), Universitas Udayana, Jl. Raya Kampus Unud, Jimbaran, Kuta Selatan, Badung, Bali, 80361, Indonesia;
Email: mandharabrasika@unud.ac.id

DOI: http://dx.doi.org/10.36956/sms.v3i1.354

cess to water [6] due to their geographical condition. Due to several research, 260 of 400 rivers in Bali had run dry and the largest lake had dropped 3.5 metres [7]. The climate has worsened the condition.

Some climate variability like El Nino Southern Oscillation (ENSO) has a significant role. Indonesia precipitation is strongly correlated with ENSO variations in the Pacific basin [8]. There are 43 drought events in Indonesia during 1884-1998, only 6 of them are not correlated with El Nino [9]. Meteorological role is more common in Bali during moderate and strong El Nino [10]. Rainfall pattern in Bali is categorized as the Monsoonal season which has the driest and longest dry season in Indonesia, compared to other types of season. The minimum mean of rainfall might reach 100 mm/month with the driest months between July and September [11]. El Nino has a significant impact on dry conditions in Bali, mainly between June-October [12]. El Nino Modoki (tripole mode of El Nino) has decreased rainfall in Bali for 8-16% [13].

Bali is a relatively small island which most of their population lives near the coastal area. The near coastal region with a high population has been threatened by saltwater intrusion. This characteristic can be found in south Bali such as Denpasar, Kuta, Jimbaran and others. For example in Jimbaran (our observation station located) has several coastal close by and the closest one is less than 3 km away. The salt groundwater in this region is mainly caused by seawater and hydrogeochemical influence [14]. In other similar near coastal region with a high population like Semarang city, salt water intrusion affects 3,44 km region from coastline [15]. However, this region might change over time depending on several factors such as aquifer withdrawal, hydraulic properties and the confining unit of coastal area [16].

There are many solutions offered to combat this water crisis. Some like rainwater harvesting, greywater reuse and solar desalination [17,18,19]. Other potential solution is harvesting the water directly from the atmosphere as our air contains lots of water. On land surface, satellite can detect the amount of water in our air is about 3,42 g/cm^2, with standard deviation 1.82 g/cm^2 [20]. However, we need tools to collect the water from the atmosphere, it is known as Atmospheric Water Generator (AWG). AWG has a similar principle with Refrigerator and Air Conditioner which is cooling through evaporation [21]. But before developing AWG, we have to understand our weather condition. How much the real water content in our area. When is the optimum condition for water harvesting. In this research we observe several atmospheric parameters. Then calculate water availability. Lastly it is simulated to model the potential of water harvesting to fulfil daily water needs.

2. Data and Method

2.1 Atmospheric Observation using WS1040

In this research we observe the atmospheric condition in our station at the Faculty of Marine Science and Fisheries, Udayana University. The observation utilizes Automatic Weather Station (AWS) as a data collector. The AWS is WS-1040 which is produced by Shenzen TianKan Electronic Technology Co., Ltd. WS-1040 is a series of wireless weather station with solar power and PC link. This can be seen in Figure 1 [22].

Figure 1. Installation of WS1040 Weather Station on Udayana University

With this equipment, we can observe several atmospheric parameters such as Temperature, Humidity, Pressure, Wind Speed, Wind Direction and Rainfall in 30 minutes timestep. The WS-1040 is placed in the open-air area with a radius of minimum 30 meters to the closest building. This is to reduce the bias of data caused by the effect of building or other possible disturbance such as trees, animals and humans.

Figure 2 shows the location of the weather station. It is located in the open area of Faculty Marine Sciences and Fisheries, Udayana University. The closest coast is less than 3 km away and there are many beaches in the radius 5 km. Thus, the potential of seawater intrusion is high and atmospheric condition is mainly affected by ocean.

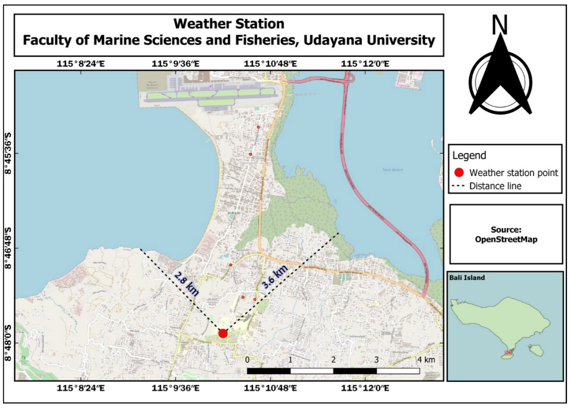

Figure 2. Location of Weather Station: Faculty of Marine Sciences and Fisheries, Udayana University

DOI: http://dx.doi.org/10.36956/sms.v3i1.354

The observation was started in November 2019. However, the data that will be used in this research is from 01 January 2020 to 31 December 2021. We only focus on 3 parameters, Station Pressure (mBar), Ambient Temperature (C) and Relative Humidity (%). As they are considered in optimization design of Atmospheric Water Generator [23,24,25].

The daily, monthly and seasonally pattern of these atmospheric parameters will be observed to gain a general understanding of the condition in our station. For the season, we divide it into 2 season, dry and rainy. This is due to the classification of Indonesia's rainy season. Bali is located in the area with Monsoonal season [11]. Dry season is in April-September, while the rainy season is October-March.

2.2 Water Content at Atmosphere

To measure the amount of water in the air, we calculate it from several atmospheric parameter such as temperature and relative humidity. From research by [26], the absolute humidity is calculated as below:

$$\rho_v = \frac{e_a M_w}{R \times T_k}$$

e_a and e_s is given by:

$$e_a = RH \times e_s$$

$$e_s = 0.611 \times \exp(\frac{b \times T}{c + T})$$

Where: ρ_v is absolute humidity or vapor pressure (g/m^3), e_a is vapor pressure (kPA), e_s is saturation vapor pressure (kPA), M_w is molecular weight of water (g/mol) equal to 18.02 g/mol, R is universal gas constant (J/ mol K) equal to 8.31 J/mol K. T is temperature in Celcius (^{o}C) while Tk is in Kelvin (^{o}K). RH is relative humidity (%). b and c both are constant, b = 17.502 and c = 240.97 for liquid.

2.3 Model of Water Surplus/ Deficit

By calculating the amount of water content in the atmosphere, we can address fluctuation of potential water harvesting. However, this information is insufficient to explain the possibility of water harvesting from the atmosphere to fulfil the daily water need. We have to consider the minimum need and optimum need of water per person.

We model this condition by fitting the gap between water harvesting and water need in daily time-series. The surplus and deficit of water can be seen on our model. We simulate the extra water of each day being stored in water storage. So, the surplus/deficit water is calculated based on cumulative sum. The surplus day is when the cumulative sum is positive (above 0) and the deficit is negative (below 0). In this model we assume there is 100% efficiency and 10.000 m^3 of air is processed in a day. The sum of surplus and deficit is also calculated to evaluate the annual condition. This can address the strategy of water storage.

3. Result and Discussion

3.1 Atmosphere Variability

a. Daily and Monthly Atmosphere Variability

First, we want to understand the general variability of several atmosphere parameters during our observation time. Figure 3 shows the daily and monthly timeseries of Temperature, Humidity and Absolute Pressure in 2020 at the Faculty of Marine Sciences and Fisheries Campus using weather station WS1040. The daily mean illustrates clearly the oscillation of its variability. The monthly timeseries can show the general condition but fail to detect the detail. For example, humidity between October-December is low in monthly average but if we see the daily average it increases in general. This is because during this month the humidity is more unstable which causes more significant changes day by day.

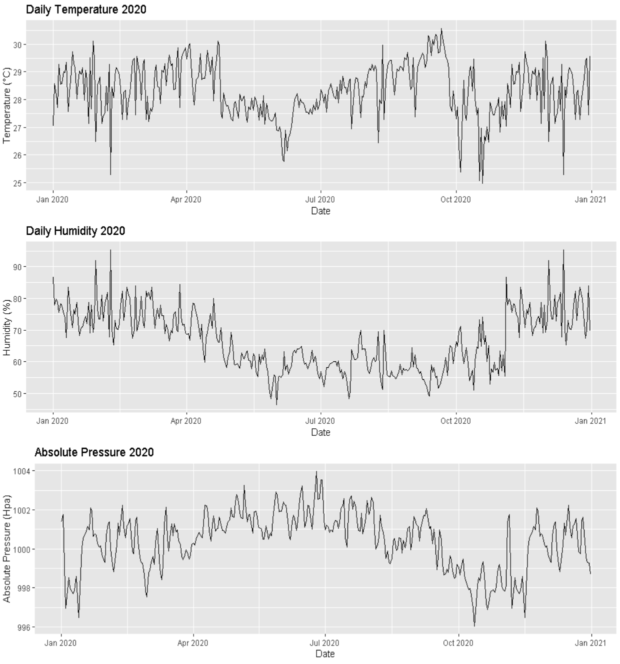

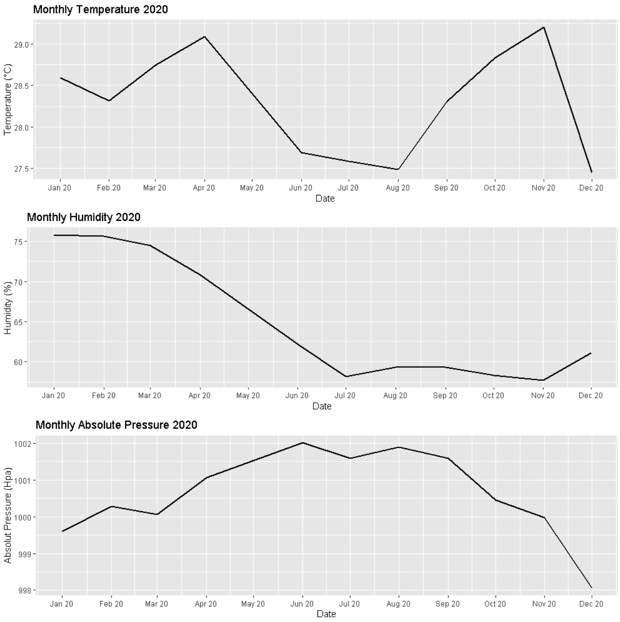

Figure 3. Daily and Monthly timeseries of Temperature, Humidity and Absolute Pressure from 01 January 2020 to 31 December 2020

Temperature has two peaks in April and November, with the lowest point in August. In general during the dry season (April-September), the temperature is dominantly low. Compared with the dry season, it has higher unstable monthly temperature. This is very clear when November mean temperature reaches more than 29^{o}C, then it drastically drops to less than 27,5 ^{o}C in December. For humidity, it starts to decrease in April (dry season) and remains low until December. So, it is generally low humidity during the dry season. The absolute pressure has an opposite pattern. It is dominantly high during the dry season between April-September. However, these three patterns have shown the similarity of unstable conditions between October-December. It is clear when we compare daily average and monthly average. While the monthly average is going down, the daily average is generally increasing.

b. Day-night Mean during Rainy Season

To get a deeper understanding of when is the optimum time to generate water from the atmosphere. Here we compare the day-night mean of atmosphere parameters in the rainy and dry season with a 30 minutes interval. We calculate the mean of parameter at the same time during a season. For example, the mean temperature at 7 a.m. in the morning in each day during the rainy season. The dry season will be discussed in the next section. Day-night mean in the rainy season (October-March) can be seen in Figure 4 as below:

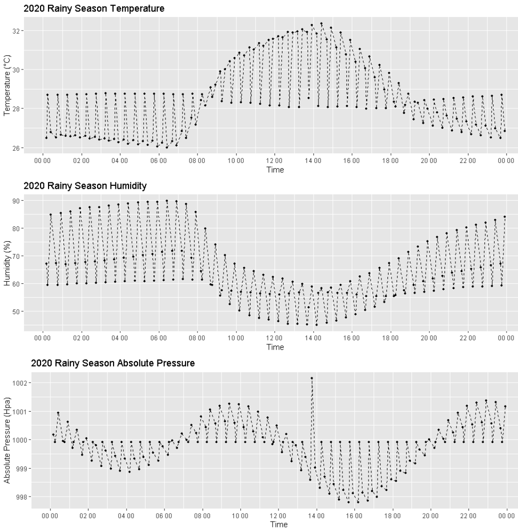

Figure 4. Day-night mean variability of Temperature, Humidity and Absolute Pressure during Rainy season

General day-night variability is clearly shown for all parameters in the rainy season. Temperature and Humidity have an opposite pattern. While temperatures increase between 08.00 to 14.00, humidity decreases exactly at the same time. Then temperature decreases from 14.00 to 19.00 and humidity increases. At night (19.00-08.00), both temperature and humidity day-night mean are constant. The absolute pressure is oscillating the peak around 09.00 and 23.00, the lowest point around 16.00.

c. Day-night Mean during Dry Season

Figure 5 shows day-night mean during the dry season between October-March. In general there are no significant differences between the rainy season and dry season. The cycle of increasing and decreasing temperature appears between 07.00-19.00. While the humidity shows the opposite pattern with temperature.

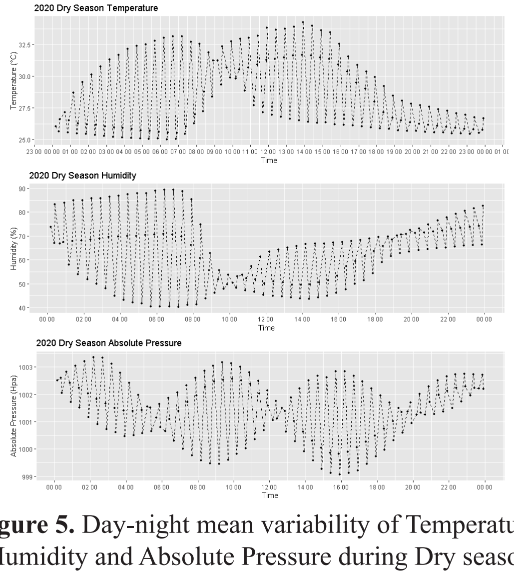

Figure 5. Day-night mean variability of Temperature, Humidity and Absolute Pressure during Dry season

DOI: http://dx.doi.org/10.36956/sms.v3i1.354

There are slight differences in the ranges. For example, in dry seasons humidity might occur less than 40%. Temperature, humidity and absolute pressure are also more unstable in the dry season compared with the rainy season. There is a typical stable time for the parameter. Temperature and Humidity are relatively stable from 09.00 to 10.00. The absolute pressure is more stable around 12.00.

3.2 Optimum Water Generation

By calculating absolute humidity, we get the amount of water in every cubic of air in the atmosphere. Although not all 100% water content can be extracted into fresh water due to the limitation of technology, we can still understand its potential by analysing the variation of absolute humidity. Here Figure 6 simulates the daily mean of water content of every 10.000 m^3 air for each month. As water is a daily need, we need water availability on a daily basis. Here we plot daily mean of water content, based on absolute humidity calculation, in Figure 6.

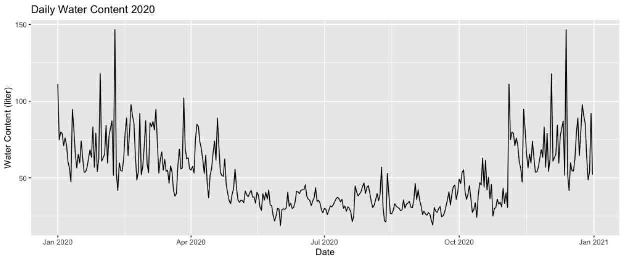

Figure 6. Daily mean of absolute humidity

Here we can see the detailed daily water content. Although the monthly mean is high, it does not mean that the water is available in the very high concentration every day. For example, between January and March the water content is changing drastically day-by-day. The highest reaches almost 150 litres per day, while the lowest is less than 25 litres per day. In the dry season, the variation of water content is lower. It is constant around 20-50 litres per day.

To collect water from the atmosphere, AWG (Atmospheric Water Generator) is the tool. There are many types of AWG. However, the efficiency of water generation is mainly caused by 3 factors, Temperature, Humidity and Flow rate. For example, AWG with a thermoelectric cooling method able to produce 11-25 gram/hour [27]. The water generation increases with humidity and air flow rate, optimum in 90% RH and 30 m^3/h flow rate [28].

3.3 Daily Fresh Water Simulation

To fulfil their fundamental water need, humans require about 50 litres of water per person per day, although in humid climates humans can survive with 10 to 20 litres per person per day [29]. In Figure 7, we illustrate the gap between daily water need (50 litres/day/person) and daily water supply/availability. We assume there is water storage which is able to store all surplus water in previous days. So we can understand the surplus (positive) and the deficit (negative) of water on a daily basis.

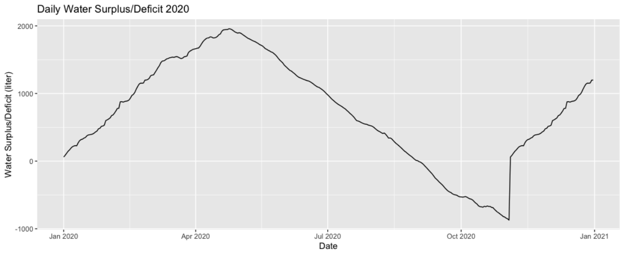

Figure 7. water surplus/deficit simulation

Between January and May, the water supply is higher than water demand. The excess water can be stored in water storage. The minimum capacity of water storage needed is 2.000 litres which is seen from the peak of the graph. Then in the period May-November, the water supply decreases below the daily fundamental water need. This caused a drop in water storage until the water deficit in September-November. The water deficit is not in the dry season, but months after the dry season.

In total, we can extract 14.528 litres of water in a year if we process 10.000 m^3 of air every day and gain 100% efficiency. Unfortunately, it is not enough to fulfil water needs of a person in a year, as it still deficit around 871 litres of water.

4. Conclusions

Our atmosphere observation with WS1040 automatic weather station has shown the variability of several parameters in our location. The data with intervals 30 minutes provide detailed observation. Temperature is more stable during the dry season from April to September which increases periodically every month. While in the rainy season, the unstable condition might be caused by some disturbance such as heavy rain or strong wind. The humidity has the opposite general pattern with temperature during the dry season. However in the rainy season, both temperature and humidity are generally high.

These two parameters are utilized to calculate the water content in atmosphere. Between January and May is the highest water content in the atmosphere. The daily water content in November-May fluctuates heavily in the day to day basis, while in other months it is consistently low.

The water harvesting potential might reach as high as 100 litres per day.

Our model shows that harvesting 100% water from 10.000 m^3 air per day is not sufficient to fulfil a person's fundamental daily water need (50 litres/person/day) between September and November. In the other months, we need water storage with a minimum capacity of 2.000 litres to save the water surplus. However, with this simulation, humans in the near coastal region of south Bali are able to survive by harvesting water from the atmosphere although not all of their fundamental daily water needs are fulfilled. The use of water harvesting methods as a single source of water is not recommended.

References

[1] J. Dracup, "Drought monitoring," Stochastic Hydrology and Hydraulics 5, pp. 261-266, 1991.

[2] R. Nagarajan, "Drought assesment," Springer, Dordecht-Netherlands, 2009.

[3] M. M. Mekonnen and A. Y. Hoekstra, "Four billion people facing severe water scarcity," Science Advance, 2016.

[4] World Economic Forum, "Global Risks," World Economic Forum, Geneva, 2015.

[5] S. Straus, "Water Conflicts among Different User Groups in South Bali, Indonesia," Human Ecology, pp. 69-79, 2011.

[6] G. A. Bawantu, I. G. B. S. Dharma and N. N. Pujianiki, "Potensi Air Permukaan Daerah Aliran Sungai Unda Untuk Memenuhi Kebutuhan Air Domestik dan Non Domestik di Kabupaten Karangasem," Jurnal Spektran, pp. 38-49, 2018.

[7] L. Samsura, "aljazeera.com," 1 12 2019. [Online]. Available: https://www.aljazeera.com/news/2019/12/1/bali-the-tropical-indonesian-island-that-is-running-out-of-water.

[8] Hendon, "Indonesian rainfall variability: impacts of ENSO and local air-sea interaction," Journal of Climate, pp. 1775-1790, 2003.

[9] B. Irawan, "Multilevel impact assesment and coping strategies againts El Nino: case of food crops in Indonesia," Working Papers 32714, United Nations Centre for Allevation of Poverty Through Secondary Crops Development in Asia and the Pacific (CAPSA), p. 105pp, 2003.

[10] A. M. Setiawan, W.-S. Lee and J. Rhee, "Spatio-temporal characteristics of Indonesian drought related to El Nino events and its predictability using multi-model ensemble," International Journal of Climatology, 2017.

[11] E. Aldrian and R. D. Susanto, "Identification of Three Dominant Rainfall Regions Within Indonesia and Their Relationship to Sea Surface Temperature," International Journal of Climatology, pp. 1435-1452, 2003.

[12] I. W. Nuarsa, I. W. S. Adnyana and A. R. As-syakur, "Pemetaan daerah rawan kekeringan di Bali-Nusa Tenggara dan hubungannya dengan ENSO menggunakan aplikasi data penginderaan jauh," Jurnal Bumi Lestari, pp. 20-30, 2015.

[13] I. B. M. Brasika, "Ensemble Model of Precipitation Change Over Indonesia Caused by El Nino Modoki," Journal of Marine Research and Technology, pp. 77-81, 2021.

[14] M. Bahar, R. Mezbaul and M. Salim, "Hydrochemical characteristics and quality assessment of shallow groundwater in a coastal area of Southwest Bangladesh," Environment Earth Science, pp. 1065-1073, 2010.

[15] N. Rahmawati, J.-F. Vuillaume and I. L. S. Purnama, "Sea intrusion in Coastal and Lowland areas of Semarang City," Journal of Hydrology, pp. 146-159, 2013.

[16] K. Rotzoll, D. S. Oki and A. I. El-Kadi, "Changes of freshwater-lens thickness in basaltic island aquifers overlain by thick coastal sediments," Hydrogeology Journal, pp. 1425-1436, 2010.

[17] I. N. Norken, I. K. Suputra, I. B. N. Purbawijaya and I. B. P. Adnyana, "Rainwater Harvesting for Drinking Water in Bali: Indonesia," Engineering and Technology Quarterly Reviews, 2019.

[18] A. Khatun and M. Amin, "Greywater reuse: a sustainable solution for water crisis in Dhaka, Bangladesh," in 4th Annual Paper Meet and 1st Civil Engineering Congress, Dhaka, 2011.

[19] S. Gorjian and B. Ghobadian, "Solar desalination: A sustainable solution to water crisis in Iran," Renewable and Sustainable Energy Reviews, pp. 571-584, 2015.

[20] N. C. Grody, "Remote Sensing of Atmospheic Water Content from Satellites Using Microwave Radiometry," Transactions on Antennas and Propagation, p. 24, 1976.

[21] A. Tripathi, S. Tushar, S. Pal, S. Lodh, S. Tiwari and P. R. Desai, "Atmospheric Water Generator," International Journal of Enhanced Research in Science, Technology and Engineering, 2016.

[22] Dongguan Meteorology Electronic Technology Co., Ltd., "meteorologyhk.com," 20 02 2021. [Online]. Available: http://www.meteorologyhk.com/en/displayproduct.html?id=2855714227421508#.

[23] S. Suryaningsih and O. Nurhilal, "Optimal Design of an Atmospheric Water Generator (AWG) based

DOI: http://dx.doi.org/10.36956/sms.v3i1.354

on thermo-electric cooler (TEC) for Drought in Rural Area," in AIP Conference Proceeding, Bandung, 2016.

[24] K. Pontious, B. Weidner, N. Guerin, A. Dates, O. Pierrakos and K. Altaii, "Design of an Atmospheric Water Generator: Harvesting Water out of Thin Air," in IEEE Xplore, Charlottesville, 2016.

[25] T. Anbarasu and S. Pavithra, "Vapour compression regrigeration system generating fresh water from humidity in the air," in SEISCON, Chennai, 2011.

[26] C. Campbell, "Environmental Biophysics," 19 December 2019. [Online]. Available: https://www.environmentalbiophysics.org/chalk-talk-how-to-calculate-absolute-humidity/.

[27] S. Liu, W. He, D. Hu, S. Lv, D. Chen, X. Wu, F. Xu and S. Li, "Experimental analysis of a portable atmospheric water generator by thermoelectric cooling method," in 9th International Conference on Applied Energy, Cardiff, 2017.

[28] W. He, P. Yu, Z. Hu, S. Lv, M. Qin and C. Yu, "Experimental Study and Performance Analysis of a Portable Atmospheric Water Generator," Energies, p. 73, 2019.

[29] P. H. Gleick, "Basic Water Requirements for Human Activities: Meeting Basic Needs," Water International, pp. 83-92, 2009.

DOI: http://dx.doi.org/10.36956/sms.v3i1.354

Sustainable Marine Structures
http://ojs.nassg.org/index.php/sms/index

ARTICLE

Non-linearity Analysis of Ship Roll Gyro-stabilizer Control System

Sathit P.[1*] **Chatchapol C.**[2] **Phansak I.**[3]

1. Department of Maritime Engineering, Faculty of International Maritime Studies, Kasetsart University, Chonburi, 20230, Thailand
2. Department of Mechanical Engineering, Faculty of Engineering, Kasetsart University, Bangkok, 10900, Thailand
3. Department of Nautical Science and Maritime Logistics, Faculty of International Maritime Studies, Kasetsart University, Chonburi, 20230, Thailand

ARTICLE INFO

Article history
Received: 19 January 2021
Accepted: 24 May 2021
Published Online: 30 May 2021

Keywords:
Active gyro-stabilizer
Twin gyro-stabilizer
Ship large roll motion
System identification
Inverse problems
Non-linear damping moment
Non-linear restoring moment

ABSTRACT

A gyro-stabilizer is the interesting system that it can apply to marine vessels for diminishes roll motion. Today it has potentially light weight with no hydrodynamics drag and effective at zero forward speed. The twin-gyroscope was chosen. Almost, the modelling for designing the system use linear model that it might not comprehensive mission requirement such as high sea condition. The non-linearity analysis was proved by comparison the results between linear and non-linear model of gyro-stabilizer throughout frequency domain also same wave input, constrains and limitations. Moreover, they were cross checked by simulating in time domain. The comparison of interested of linear and non-linear close loop model in frequency domain has demonstrated the similar characteristics but gave different values at same frequency obviously. The results were confirmed again by simulation in irregular beam sea on time domain and they demonstrate the difference of behavior of both systems while the gyro-stabilizers are switching on and off. From the resulting analysis, the non-linear gyro-stabilizer model gives more real results that correspond to more accuracy in a designing gyro-stabilizer control system for various amplitudes and frequencies operating condition especially high sea condition.

1. Introduction

Of the six modes of motions of marine vessel, roll motion is the important mode to be realized. It is the greatest reason to capsize also affect to operation of crews, passengers comfortable and cargos damage, when a vessel is excited by wave load at high sea. In order to diminish amplitude of roll motion, roll stabilizer system becomes an important role.

More than 100 years, many types of roll stabilizer have been engineered by many researchers and designer. The following example, bilge keels, sloshing, sliding weight, gyro, u-tube, sea-ducted, variable angle fins, hydro-foil keel fin and rotating cylinder etc.

Since 1995, Chadwick [1] had gathered types of roll stabilizers and it has been classified by control method to be passive and active control. The passive control is the control system does not require any external power source to operate the control device but the active control system does opposite way [2]. Some types of stabilizer are only passive control as bilge keels and sloshing. Some types are only active control such as variable angle fins and rotating cylinder. And some types are both as sliding weight,

---

**Corresponding Author:*
Sathit P.,
Department of Maritime Engineering, Faculty of International Maritime Studies, Kasetsart University, Chonburi, 20230, Thailand;
Email: sathit.pon@ku.th

DOI: http://dx.doi.org/10.36956/sms.v3i1.316

u-tube, sea-ducted and gyro.

Another way, Haghighi and Jahed-Motlagh [3] have mentioned classification of system control types that can be classified as either external or internal control systems. The external control system is systems generate resisting load (forces and moments) outside a ship hull and the internal control system is systems generate resisting load inside [4]. The principal advantages of internal systems are not hydrodynamic drag and effective zero forward but it has heavyweight, volume penalty and there are limited in stabilisation capability. The external systems have lightweight but it creates hydrodynamic drag and ineffective at zero forward speed [5,6]. The following above mention and nowadays technology, a gyro-stabilizer become to be an interesting system at present. Because it has a combination of internal and external control system advantages: potentially light weight with no hydrodynamic drag and is effective at zero forward speed.

A gyro-stabilizer system is to use resisting moments, which moments are the cross product between angular momentum vector of flywheel and angular velocity vector around precession axis. The resisting moment is applied to vehicle or other to resist external excitation moments that are keeping minimal oscillatory amplitude of rolling vehicle. However, this paper focus on a gyro-stabilizer is applied to small ships.

Background stories of gyro-stabilizers, it has been applied to various inventions. The first gyro-stabilizer application was invented by Brennan [7]. Brennan used twin gyro that it had counter-rotating flywheels to stabilize unstable vehicle (two-wheel monorail car). This invention had similar patents [8,9,10]. More researches, gyro-stabilizers were applied to stabilize to two-wheel vehicles such as a bicycle [11] and motorcycles [12]. In 1996, Brown and his team published about the using gyro-stabilizer that provides mechanical stabilization and steering a single-wheel robot [13]. Another field, NASA used the advantage of gyro-stabilizer to control attitude of large space structures or satellite [14]. In additional, gyro-stabilizers have been applied to maritime field, e.g., autonomous under water vehicle [15,16], torpedo [17] and free surface vehicle etc. The first record of a gyro-stabilizer in marine vehicles was found accidentally, Howell torpedo, it was installed rapid rotation of fly-wheel. There was 16 inches a steel wheel diameter and was spun up to 16,000 rpm. The torpedo was experimented for locking target on U.S. Navy boat [17]. For the first time of free surface vehicle, a gyro-stabilizer device was passive system that it was utilized to diminish roll motion [18,19,20]. Active gyro-stabilizer systems were developed from passive systems. The first system was proposed by Elmer Sperry in 1908 [21].

Recently, many researchers have proposed related new researches of gyro-stabilizer with novel control methods. Townsend et al. [4] published a new active gyrostabiliser system for ride control of marine vehicle. McGookin et al. [22] published application of MPC and sliding mode control to IFAC benchmark models. Perez and Steinmann [23] demonstrated analysis of ship roll gyrostabilizer control that revisited the modelling of coupled vessel-gyrostabilizer and also describes design trade-offs under performance limitation. Haghighi and Jahed-Motlagh [3] proposed ship roll stabilization via sliding mode control and gyrostabilizer.

For designing ship roll gyro-stabilizers, a preliminary design is important thing. In order to design it, designers need to know wave loads, ship motion (ship model) and actuator characteristics (gyro-stabilizer model). Almost, modelling of designing uses an equation of motion in linear model that it may not comprehensive mission requirement, such as large roll motion from both high amplitudes and frequencies of waves. Normally, these have to be non-linear model under limitations that have more correction and accuracy also failure cases from system instability. The failure cases may not occur in linear modelling but it was found in non-linear. From these reasons, it becomes the motivation of this study. Both linear and non-linear model of gyro-stabilizer and ship were concerned.

Non-linear system modelling of gyro-stabilizer was comprised of ship rolling model and single axis gimbal gyroscope model (non-linear equation of motion). Normally, non-linearity of gyro-stabilizer model appears in restoring term and exciting moment term. However non-linearity of ship roll model able to appear all terms of equation of motion (term of inertia, damping, restoring and exciting moment).

In order to formulate non-linear ship roll model, the system identification method is used to find non-linear coefficients of added inertia, damping and restoring term of ship. The system identification methods of ship roll motion can be found in many papers such as Masri et al. (1993) [24], Chassiakos and Marsi (1996) [25], Liang et al. (1997) [26], Liang et al. (2001) [27], Jang et al. (2009) [28], Jang et al. (2010) [29], Jang (2011) [30] and Jang et al. (2011) [31] etc. However, in this paper uses method of Pongdung et al. [32] which is the novel method and able to find all of non-linear terms of ship model.

The objective of this presentation is to analyse non-linearity of ship roll twin gyro-stabilizer control system under limitations of wave load and precession angle via frequency domain analysis and time domain simulation.

2. Principals and Theories

Analysis of gyro-stabilizer system has three parts that is realised. It comprised of water wave model, ship

DOI: http://dx.doi.org/10.36956/sms.v3i1.316

model and gyro-stabilizer model. In order to reach the present objective, the regular and irregular deep water wave models are selected to set simulation cases. The ship and gyro-stabilizer models is concerned both linear and non-linear model to observe and analyze effects of system non-linearity from simulation results.

The general principle of gyroscopic stabilization, its torque is produced by gyro-stabilizer that installed in a ship opposes roll exciting moment from water wave. This exciting moment disturbs the angular momentum of flywheel such that develops precession motion. The cross product of flywheel angular momentum and precession rate induces moment to resist the exciting moment in opposite direction [33]. Figure 1 explains working principle of gyro-stabilizer that is installed in a marine vessel. At present, twin-flywheels are selected, and there are spinning and precession angle rotate in opposite direction. Its result cancels the side effect of gyroscopic moments in the other directions (normally in pitch and yaw of ship). Figure 2 displays the working of twin gyro-stabilizer.

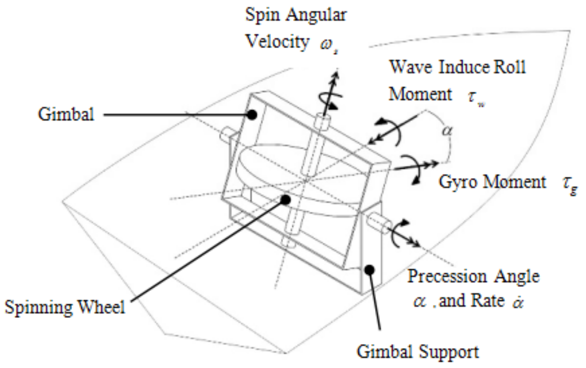

Figure 1. Illustration single gyro-stabilizer installation and its working principle

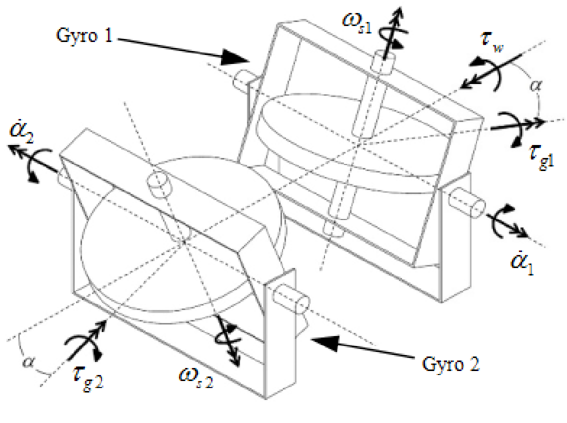

Figure 2. Demonstration working principle of twin gyro-stabilizer and elimination of its side effect of gyro-stabilisation moment

2.1 Full Non-linear Gyro-stabilizer Model

The prediction of gyro-stabilizer performances was modelled via the two equations of motions. The first equation is the ship model and the second equation is gyro-stabilizer model.

Consideration a ship motion, while it is excited by water wave that is demonstrated in Figure 3. Instantaneous, the ship is rolled by moment of inertia in counter clockwise and is acted by wave, which wave free surface has β (wave slope angle) against horizontal line. The y axis of body fix frame has ϕ (roll angle) against horizontal line. Thus θ is relative angle between roll and wave slope angle. The following Newton's second law, the equation of motion of ship can be written as

$$(I_{44}+I_{44a}(\ddot{\theta}))\ddot{\theta}+B_{44}(\dot{\theta})\dot{\theta}+C_{44}(\theta)\theta=0 \tag{1}$$

where I_{44} is moment of inertia of ship that is a constant value. $I_{44a}(\ddot{\theta})$ is non-linear added moment of inertia function. $B_{44}(\dot{\theta})$ is non-linear damping moment function and $C_{44}(\theta)$ is non-linear restoring moment function. In order to find non-linear functions, non-parametric system identification method is used.

Briefly, Pongdung's method [32] is chosen to determine non-linear functions because it able to find all non-linear functions in Equation 1 synchronously. The method needs measured motion data from free roll decay experiment or CFD (Computational fluid dynamics) to formulate inverse problem. Actually, the responses are outputs and are calculated via equation of motion that the non-linear functions of each term are known variable values. On the other hand, the responses become to input (measured data) in inverse problem and the non-linear functions become to output (unknown variables). Each moment terms are solved by inverse problem formalism and stabilized by Landweber's regularization method. Its solutions are chosen the optimal solution through L-curve criterion. Finally, the zero-crossing detection technique of measured data is compared with that solution for identifying each moment function and reconstruction them. For more detail can see in Pongdung et al. [32].

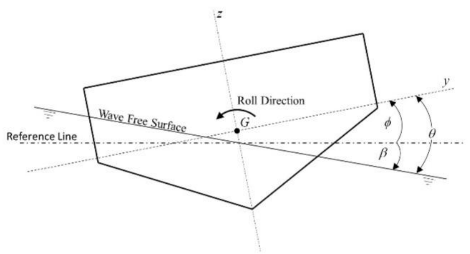

Figure 3. Rolling of ship on water wave free surface

When all non-linear functions is known, substituting

$\theta = \phi - \beta$ into Equation 1, it becomes

$$[I_{44} + I_{44a}(\ddot{\phi} - \ddot{\beta})](\ddot{\phi} - \ddot{\beta}) + [B_{44}(\dot{\phi} - \dot{\beta})](\dot{\phi} - \dot{\beta}) \\ +[C_{44}(\phi - \beta)](\phi - \beta) = 0 \tag{2}$$

Rearranging Equation 2, it yields

$$\left[I_{44} + I_{44a}\left(\ddot{\phi} - \ddot{\beta}\right)\right]\ddot{\phi} + \left[B_{44}\left(\dot{\phi} - \dot{\beta}\right)\right]\dot{\phi} \\ +\left[C_{44}\left(\phi - \beta\right)\right]\phi = [I_{44} + I_{44a}(\ddot{\phi} - \ddot{\beta})]\ddot{\beta} \\ +[B_{44}(\phi - \beta)]\dot{\beta} + [C_{44}(\phi - \beta)]\beta \tag{3}$$

Equation 3 is the full nonlinear ship motion: left-hand side is ship moment and right-hand side is exciting moment. The Equation 3 has the same coefficient function in the same term of inertia, damping and restoring: the roll angle and wave slope are equal values at steady state on time domain, but at transient are not.

Thus, define

$$\tau_w = [I_{44} + I_{44a}(\ddot{\theta})]\ddot{\beta} + [B_{44}(\dot{\theta})]\dot{\beta} + [C_{44}(\theta)]\beta \tag{4}$$

The wave slope β is determined from Equation 5, which it is regular linear wave (deep water wave).

$$\eta(x,t) = \eta_0 \sin(kx - \omega t) \tag{5}$$

where η_0 is wave amplitude, k is wave number, x is distance in x direction, ω is angular frequency and t is time. When differentiate Equation 4 with x, it becomes to wave slope equation follow as Equation 6. Then wave slope velocity and acceleration are Equation 7 and 8 respectively.

$$\frac{d\eta(x,t)}{dx} = \beta = \eta_0 k \cos(-\omega t) \tag{6}$$

$$\dot{\beta} = \eta_0 k \omega \sin(-\omega t) \tag{7}$$

$$\ddot{\beta} = -\eta_0 k \omega^2 \cos(-\omega t) \tag{8}$$

Thus, a model for motion of the ship in roll together with and n-spinning-wheel gyro-stabilizer can be expressed follows as block diagram in Figure 4. Then it can be formulated in equation of motion follow as Equation 9 and 10.

$$I_{44} + I_{44a}(\ddot{\theta})\ddot{\phi} + B_{44}(\dot{\theta})\dot{\phi} + C_{44}(\theta)\phi = \tau_w - \tau_g \tag{9}$$

$$I_g \ddot{\alpha} + B_g \dot{\alpha} + C_g \sin\alpha = \tau_s - \tau_p \tag{10}$$

where α, $\dot{\alpha}$ and $\ddot{\alpha}$ in Equation 9 are precession angle, precession rate and precession acceleration respectively. The following Equation 10 I_g, and C_g are moment of inertia, damping and restoring coefficient of gyro-stabilizer about precession axis.

Equation 9 represents the full non-linear ship roll dynamics, while Equation 10 represents the non-linear dynamics of gyro-stabilizer about the precession axis. The following Equation 9 and Equation 10 associate coupled system, the wave-induce roll moment (τ_w) excite the ship rolling. When roll motion develops, the roll rate induces a moment about the precession axis of spinning wheels (τ_s). And then the spinning wheels develop precession, its reaction moment resists on the ship with opposes direction of the wave-induce moment (τ_g).

$$\tau_s = K_g \dot{\phi} \cos\alpha \tag{11}$$

$$\tau_g = n K_g \dot{\alpha} \cos\alpha \tag{12}$$

where K_g is spinning angular momentum ($K_g = \omega_{spin} I_{spin}$)

The roll stabilization moment for passive system can be modified the precession damping and stiffness as well as leave the gyro to free work. For an active system, it is controlled through the precession dynamics via the precession control moment that is PD controller and expressed follow

$$\tau_p = K_p \alpha + K_d \dot{\alpha} \tag{13}$$

where K_p is proportional control gain and K_d is derivative control gain. The advantage of this control law is no needing ship roll sensors.

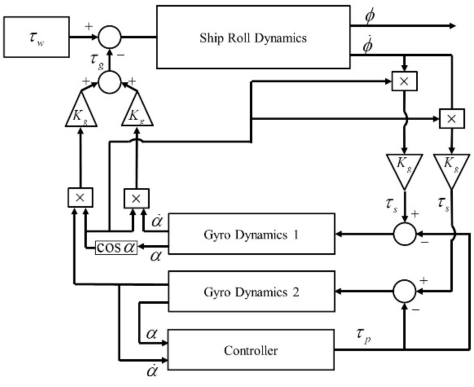

Figure 4. Block diagram of full non-linear twin gyro-stabilizer model

DOI: http://dx.doi.org/10.36956/sms.v3i1.316

2.2 Linear Gyro-stabilizer Model

In the past, analysis any control systems via equation of motions were treated to be linear differential equation. There are reduced complexity and able to transform to s-domain, and then change s-domain to be frequency domain. At steady state, the analysis control systems through frequency domain are proper. This section uses almost equation from Perez and Steinmann (2009) [23]

From Equation 9 and Equation 10, the models are linearized: for small angle of roll and precession, the coefficients of left-hand side are constant value. However, let define,

$$\dot{\phi}\cos\alpha \approx \dot{\phi} \tag{14}$$

$$\dot{\alpha}\cos\alpha \approx \dot{\alpha} \tag{15}$$

and

$$\sin\alpha \approx \alpha \tag{16}$$

Hence, the linear equation expressed as follow:

$$\left(I_{44}+I_{44a}\right)\ddot{\phi}+B_{44}\dot{\phi}+C_{44}\phi=\tau_w-\tau_g \tag{17}$$

$$I_g\ddot{\alpha}+B_g\dot{\alpha}+C_g\alpha=\tau_s-\tau_p \tag{18}$$

$$\tau_w=\left(I_{44}+I_{44a}\right)\ddot{\beta}+B_{44}\dot{\beta}+C_{44}\beta \tag{19}$$

$$\tau_s=K_g\dot{\phi} \tag{20}$$

$$\tau_g=nK_g\dot{\alpha} \tag{21}$$

Note that, τ_p no changes in linear model. And linear gyro-stabilizer system is demonstrated in Figure 5.

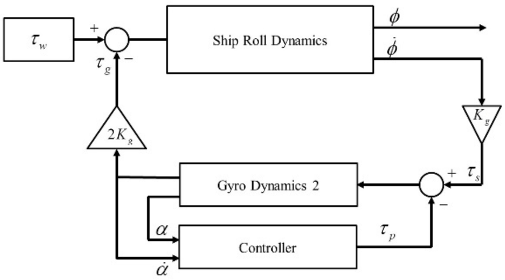

Figure 5. Block diagram linear twin gyro-stabilizer model

From zero condition, thus the open loop transfer function is

$$H_{ol}\left(s\right)=\frac{\phi_{ol}\left(s\right)}{\tau_w\left(s\right)}=\frac{1}{(I_{44}+I_{44a})s^2+B_{44}s+C_{44}} \tag{22}$$

The close loop transfer function is

(23)

where $\phi_{ol}\left(s\right)$ and $\phi_{cl}\left(s\right)$ are Laplace transforms open and close loop roll angle respectively. And the transfer function of precession angle to roll angle is

$$H_{cl}\left(s\right)=\frac{\phi_{cl}\left(s\right)}{\tau_w\left(s\right)}=\frac{I_gs^2+B_g^{'}s+C_g^{'}}{\left(I_{44}s^2+B_{44}s+C_{44}\right)\left(I_gs^2+B_g^{'}s+C_g^{'}\right)+nK_g^2s^2}$$

$$H_{pr}\left(s\right)=\frac{\alpha\left(s\right)}{\phi\left(s\right)}=\frac{\dot{\alpha}\left(s\right)}{\dot{\phi}\left(s\right)}=\frac{K_gs}{I_gs^2+B_g^{'}s+C_g^{'}} \tag{24}$$

where

$$B_g^{'}=B_g+K_d \tag{25}$$

$$C_g^{'}=C_g+K_p \tag{26}$$

The transfer function of precession angle to wave exciting roll moment that is the result from Equation 23 and 24 is

$$\begin{aligned}H_{pw}\left(s\right)&=\frac{\alpha\left(s\right)}{\tau_w\left(s\right)}=H_{pr}\left(s\right)H_{cl}\left(s\right)\\&=\frac{K_gs}{\left(I_{44}s^2+B_{44}s+C_{44}\right)\left(I_gs^2+B_g^{'}s+C_g^{'}\right)+nK_g^2s^2}\end{aligned} \tag{27}$$

Rearranging Equation 24, it yields

$$H_{pr}\left(s\right)=\left(\frac{K_g}{I_g}\right)\left(\frac{s}{s^2+\frac{B_g^{'}}{I_g}+\frac{C_g^{'}}{I_g}}\right) \tag{28}$$

and the roots are

$$p_{1,2}=-\frac{B_g^{'}}{I_g}\pm\sqrt{\left(\frac{B_g^{'}}{I_g}\right)^2-4\frac{C_g^{'}}{I_g}} \tag{29}$$

Both roots are negative real roots (stability condition) if and only if, $B_g'>0$, $C_g'>0$ also constraint of

$$\left(\frac{B_g^{'}}{I_g}\right)^2 > 4\frac{C_g^{'}}{I_g} \tag{30}$$

The following Equation 13, the proportional term is set during design due to centre of mass location, normally locate below the precession axis, which like a pendulum, the C'_g value is fixed. Thus, the control moment becomes

$$\tau_p = K_d\dot{\alpha} \tag{31}$$

From Equation 30, it able to formulate the condition of two poles to be real root:

$$B_g^{'} > \sqrt{4C_g^{'}I_g} \tag{32}$$

It can set as

$$B_g^{'} = \gamma\sqrt{4C_g^{'}I_g}, r > 1 \tag{33}$$

Then substitute Equation 33 in to Equation 25, it become

$$K_d = \gamma\sqrt{4C_g^{'}I_g - B_g}, r > 1 \tag{34}$$

This derivative control gain is used through under constrained performance follow section 2.4

2.3 Control Performance and Limitations

In order to observe the objective performance, the output sensitivity function is defined as:

$$S(s) \triangleq \frac{\phi_{cl}(s)}{\phi_{ol}(s)} \tag{35}$$

The Bode's integral constraint is

$$\int_0^\infty \log\left|S(j\omega)\right| d\omega = 0 \tag{36}$$

and the roll reduction (complementary sensitivity function) is defined as

$$RR(\omega) = 1 - \left|S(j\omega)\right| = \frac{\left|\phi_{ol}(j\omega)\right| - \left|\phi_{cl}(j\omega)\right|}{\left|\phi_{cl}(j\omega)\right|} \tag{37}$$

the integral constrain becomes

$$\int_0^\infty \log\left|1 - RR(j\omega)\right| d\omega = 0 \tag{38}$$

Another form of roll reduction function is

$$RR(\omega) = \left(1 - \frac{\left|H_{cl}(j\omega)\right|}{\left|H_{ol}(j\omega)\right|}\right) \tag{39}$$

Note that, the roll reduction values possible to be negative or positive values but less than 1 along interested range of frequency. The meaning of negative value is roll amplification. The meaning of positive value is roll reduction. Then the roll reduction close to 1, it has better performance.

2.4 Constrained Performance

The additional constrain is cause by the precession angle limiting due to mechanical design. If the precession angle reaches this limit, the device may get damage or deteriorate. Additionally, it may causes of roll amplification rather than roll reduction of ship: phase of resisting moment cannot eliminate wave induce roll moment.

For a regular wave of frequency ω^0 and wave height H_s^0, it induces roll exciting moment amplitude τ_w^0. The following Equation 27, it can be obtained the amplitude of precession angle:

$$\bar{a}^0 = \left|H_{pw}\left(j\omega^0\right)\right|\bar{\tau}_w^0 \tag{40}$$

The given constrain is the maximum precession angle $\alpha_{\max}$, it can be obtained the optimal of B'_g that it take the precession angle close to its limit:

$$\gamma^*\left(\omega^0\right) = \arg\min_{\gamma>0}\left|\alpha_{\max} - \left|\left(H_{pw}\left(j\omega^0, B'_g(\gamma)\right)\right)\right|\bar{\tau}_w^0\right| \tag{41}$$

3. Cases Study Configurations and Numerical Experiment Setup

To carry out the aim of this presentation, the non-linear gyro-stabilizer system is validated with linear gyro-stabilizer system to observe and analyze its performance at the same environment and limitation. The vessel was set to zero speed and moved against beam sea direction. In order to determine the system design point, assume that the system was designed for deep water wave, significant wave height of 0.04 m, all frequency of its.

In order to observe and analyze non-linearity of a gyro-stabilizer system, this present, V-hull section was selected because it is a general section profile of high-speed boat and small ship that are suited. The dimensions of selected V-hull are demonstrated in Figure 6. Both linear and non-linear equation of motion was found via measured data that were the result from CFD method, XFLOW commercial program. The simulations are set to be unsteady flow. There is free roll decay method, which was set initial condition of roll angles are 5, 10, 15, 20, 25 and 30 degrees. According to CFD simulation results, the example of measured data from simulation case, which was set 30 degree of initial condition was demonstrated in Figure 7.

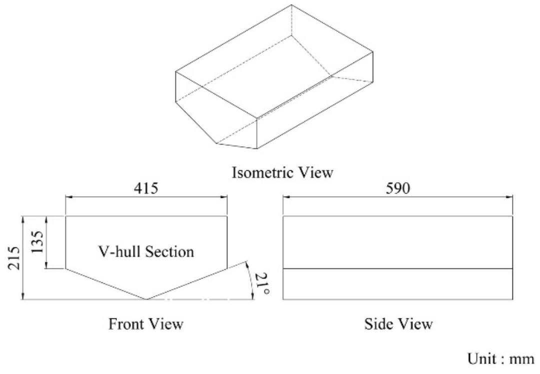

Figure 6. The V-hull Geometry and dimension for simulation

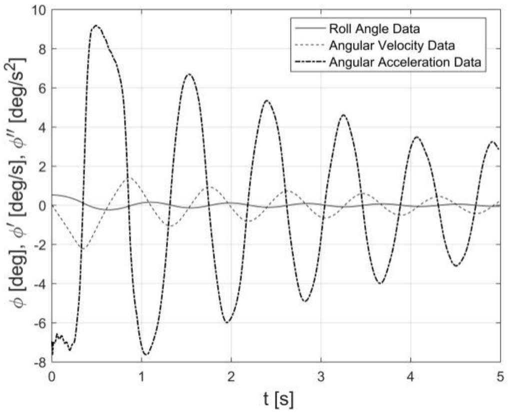

Figure 7. Measured Data from CFD of Initial Condition 30 Degree

The linear ship model was formulated from logarithmic decrement method. The method appropriates to small roll motion less than 8 degree. It requires only roll angle data (measured data from CFD) to detect maxima or minima values, where are used to find estimated exponential function. The function leads to determine the damping ratio and natural frequency. There can be converted to add moment of inertia, damping coefficient. However, restoring coefficient can be found from inclination calculation. According to this method, the details of calculation were omitted in this presentation.

For this paper, the simulation of 5 degree of initial condition was used. The estimating of exponential function was shown on Figure 8. According to estimated exponential function the linear ship model is

$$0.3255\ddot{\phi}+0.0494\dot{\phi}+19.7321\phi=0 \tag{42}$$

Note that, in free roll motion test $\theta=\phi$, there are not have relative motion between free surface and roll motion angle and $I_{44}=0.26$.

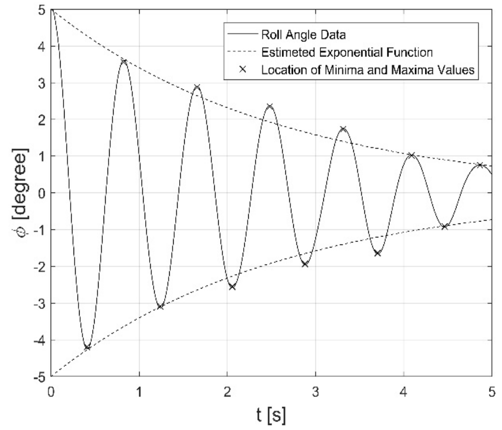

Figure 8. Determination of exponential function from roll angle data of 5 degree initial condition

The non-linear ship model was formulated by reconstruction non-linear damping coefficient and added moment of inertia via systems identification method that used all of measured data (roll angle, angular velocity and angular acceleration) and all initial condition from CFD method.

The non-linear restoring coefficient function was known via inclination calculation. The calculation result was fitted by polynomial function follow as Equation 43 and its curve was shown at the top of Figure 9.

$$\begin{aligned}C_{44}(\phi)&=-19.7321\phi^{18}+108.8680\phi^{16}-258.2096\phi^{14}\\&+344.3239\phi^{12}-283.2101\phi^{10}+148.2937\phi^{8}\\&-49.4689\phi^{6}+10.4220\phi^{4}-1.4402\phi^{2}+0.1454\end{aligned} \tag{43}$$

The non-linear damping coefficient function was found by accumulating the damping moment data point from system identification method, and there were taken by curve fitting method which is shown in the middle of Figure 9. Then the moment function was divided by ϕ, thus the non-linear damping coefficient is

$$B_{44}(\dot{\phi})=0.1588\dot{\phi}^{2}+0.1391 \tag{44}$$

From the same procedure of formulating non-linear damping moment, the added moment of inertia fitting curve is shown at the bottom of Figure 9 and its average

DOI: http://dx.doi.org/10.36956/sms.v3i1.316

value is

$$I_{44a}\left(\ddot{\phi}\right) = 0.066 \tag{45}$$

The full non-linear ship model was simulated on free decay motion with 30 degree initial condition to verify its accuracy. The simulated result of roll angle via Equation 1 was plotted in Figure 10 also result from linear model and measured roll angle from CFD. It proves that the non-linear model is better accuracy more than linear model, when both results were compared with measured roll angle from CFD. Hence, the non-linear ship model has enough accuracy and can be used in this presentation.

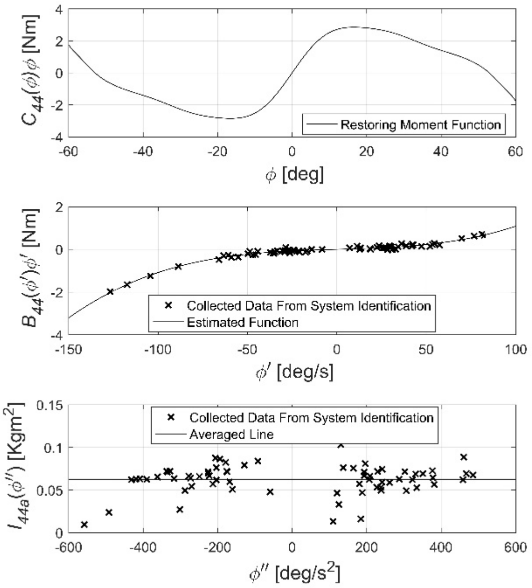

Figure 9. The Estimating functions of restoring moment (top), damping moment (middle) and added moment of inertia (bottom)

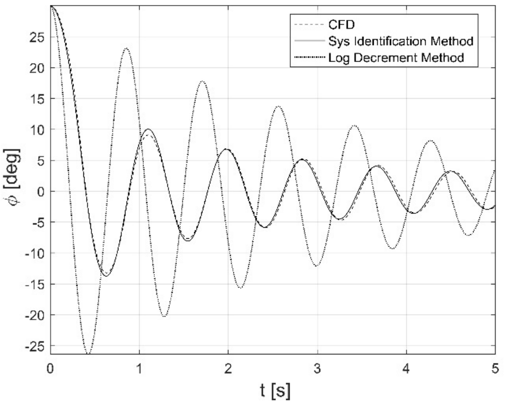

Figure 10. The comparison of simulations between results of non-linear ship model (system identification method) and linear ship model (logarithmic decrement method) with measured data from CFD

The non-linear and liner gyro-stabilizer model was used according to Equation10 and Equation 18 respectively. There have same characteristic coefficients. The gyro-stabilizer was assumed that its speed is constant at 300 rpm (ω_{spin}), the moment of inertia about spin axis is 0.0125 kg-m^2 (I_{spin}) and the moment of inertia about precession axis is 0.0005 kg-m^2 (I_g). The damping coefficient is zero $B_g = 0$, there is on friction about precession axis. The restoring coefficient is zero; the center of gravity position was located at middle of spin and precession axis (no effect of pendulum).

The following Equation 13, the proportional gain K_p is fixed value of 0.1. The derivative gain was determined via Equation 34 and Equation 41.

Both linear and non-linear systems were determined through frequency domain and simulated with regular waves, which the range of frequencies is 0 to 14.84 rad/s. The simulation cases of linear system were varied wave amplitudes from η_0 = 0.02 m up to $1.5\eta_0$. The linear simulation case of η_0 was set to be reference case. The γ^* of each wave amplitude of simulation cases follow Equation 41 were gathered, and then they were used in simulation cases of full non-linear system. The full non-linear system was simulated in time domain with only amplitude of η_0. Moreover, in order to find a design trade-off, the γ^* of each wave amplitude of linear system were used. The name of simulation cases are described in Table 1.

Table 1. The description of simulation cases

Case Name	Description	Gyro-model	Ship-model
LSOL	Linear open loop system	-	Linear
LSCL	Linear close loop system	Linear	Linear
LSCL @ $c\eta_0$	Linear close loop system that determined with wave amplitudes of $c\eta_0$ (c =1.1, 1.2, 1.3, 1.4 and 1.5)	Linear	Linear
FNSOL	Full non-linear open loop system	-	Non-linear
FNSCL	Full non-linear close loop system	Non-linear	Non-linear
FNSCL@ $c\eta_0$	Full non-linear close loop system with the γ^* values of each wave amplitude of LSOL (c =1.1, 1.2, 1.3, 1.4 and 1.5)	Non-linear	Non-linear

4. Results and Discussions

In order to examine the characteristics of performances of non-linear gyro-stabilizer system, the linear system was determined first. The following Figure 11 – 14, they show the results of linear gyro-stabilizer characteristics.

Figure 11 show exciting moment (input), the result from Equation 19. The graph was also plotted Stokes limit; the exciting moment cannot exceed this line at upper side. Stokes and exciting moment line of amplitude 0.02 m intersect at 14.84 rad/s, which it was set to be maximum value of frequency range. All lines have tough at ω = 7.786 rad/s that is natural frequency of linear vessel model because it has the same coefficients. And then, when frequencies increase, the exciting moment rapidly increase. It is obviously the increasing of wave amplitudes correspond to increasing exciting moment.

Figure 12 and 13 are they were γ^* values and precession angles of each wave amplitude respectively. They simultaneously determined via Equation 27 and 41.

Figure 12 shows the minimum γ^* values of each wave amplitude. All wave amplitudes gave γ^* values of 1 until the system gets the exciting frequency that makes the precession angle reach its limit value (60 degree, also observe Figure 13). It has been called critical point. From this point γ^* value rapidly increasing to keep precession angle does not exceed 60 degree. As the higher wave amplitude, the critical points have appeared at lower frequency.

Figure 13 shows the precession angles in frequency domain. The trend of precession angle resembles the pose of exciting moment in Figure 11. However, the crests of all lines about exciting frequency value of 2 were affected from turning proportional gain K_p that was fixed value of 0.1. And the higher wave amplitude gives the higher precession angle. The flat band at high exciting frequency that has constant value of 60 degree is explained as above paragraph.

Figure 14 shows the roll angle responses. At the lower exciting frequency from critical point, the result trends resemble precession angle but it rapidly increases when the exciting frequency increase from critical point. The increasing rapidly of roll angle from the critical point is caused by the precession angle reach its limit, which it cannot have more precession rate to create resisting moment for cancel exciting moment. Moreover, at the higher wave amplitude gives the higher roll angle response.

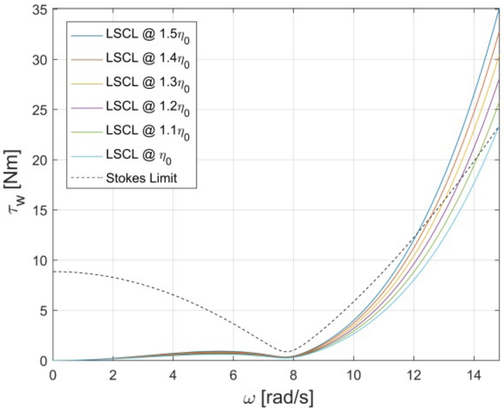

Figure 11. Exciting moment of the linear gyro-stabilizer model

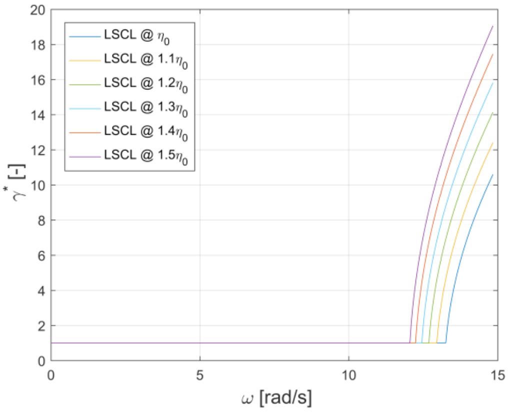

Figure 12. Estimating of γ^* values each wave amplitude from Equation 41

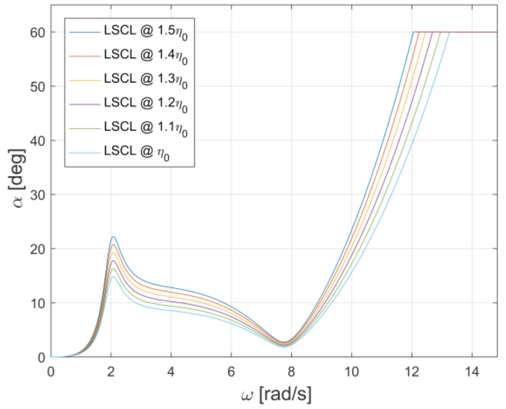

Figure 13. Precession angles of linear gyro-stabilizer model so that determined via Equation 27 and 41 with the following γ^* values each wave amplitude in Figure 12

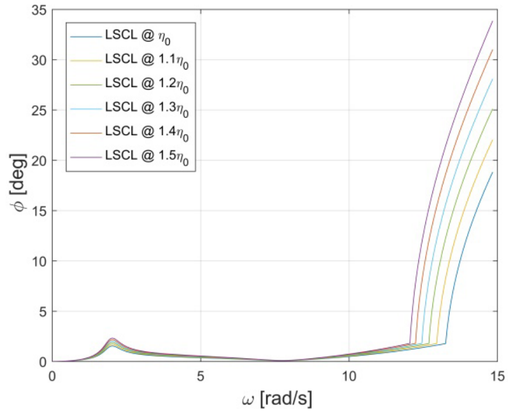

Figure 14. Roll angle responses of linear gyro-stabilizer model each wave amplitude via Equation 23

The following linear model results consistent and reasonable to each other. They can be used to compare with the non-linear system in the same wave condition. However, according to section 3, the non-linear gyro-stabilizer system model was assumed as it was designed to operate in beam sea that it has significant wave height ($H_{1/3}$) of 0.04 m (η_0 = 0.02 m). But it cannot directly determine γ^* through transfer function like linear system model. Thus the γ^* values each wave amplitude from linear model were applied to non-linear model. The non-linear system needs to simulate in time domain and collected the amplitude simulation results at steady state. Hence, Figure 15 - 18 illustrate the comparison between linear and non-linear model. Some data of non-linear model disappear because of its solutions became unstable (no steady state) when the precession angle reached the limit angle.

Figure 15 shows the exciting moments both open and close loop of linear and non-linear system. They have the trend like exciting moments of linear system. Linear open loop and close loop exciting moments are same line because they have same coefficients of vessel model. The all non-linear exciting moment lines are above liner exciting moment at high frequencies from around the natural frequency. The difference of exciting moment values causes of the coefficient functions follow as Equation 4 that related to θ , $\dot{\theta}$ and $\ddot{\theta}$.

Figure 16 shows the precession angle result that all non-linear precession angles have the same line until they reach to a limited angle at the exciting frequency value of 11.85 rad/s. And almost values are above linear system. The cause of all non-linear precession angles has the same values. They used same γ^* =1 as following Figure 12. After they reach the limited angle at higher frequencies, the data lost because the system became unstable so that it now has steady state. However, the non-linear system back to stable at the end of lines because of the increasing of γ^* value (see Figure 12) able to reduce the precession angles below limited angle. And then, they obviously show the higher γ^* each wave amplitude gave lower precession angle at the higher frequencies.

The following Figure 17, roll angle responses of the open and closed-loop of linear and non-linear systems are shown. The comparison between open-loop of linear and non-linear system obviously difference behavior along frequencies range; the linear open-loop system is fair curve, while the non-linear closed-loop system has the apex at the frequency value of 6 rad/s. This is the important cause to deep studying throughout non-linear gyro-stabilizer system; a difference response behavior will give the difference a system design point. The linear and non-linear closed-loop systems have a same trend. All non-linear roll angle responses have same values until they reach the frequency of 11.85 rad/s and almost roll angle responses values are above the linear line. The closed-loop non-linear system uses more precession angle than linear system but they give more roll angle responses than linear system. After the critical point of linear closed loop system, all lines of roll angle responses increase and approach to open-loop systems because precession angles were forced and reduced to constant in linear model and non-linear model respectively. This reason refers to inefficiency of the systems, when the precession angle reaches the limited angle.

Figure 18 explains the responses in view of a relative roll angle response and can say that are the inverse behavior of a roll angle response. While the stabilizer attempt to keep roll angle approach to zero, the difference between a wave slope and roll angle increase (see relation in Figure 3).

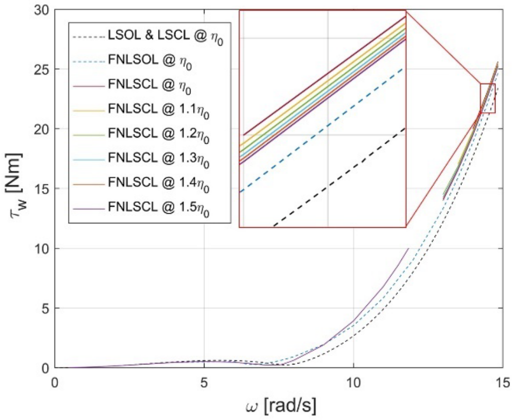

Figure 15. Comparison exciting moments between non-linear and linear gyro-stabilizer models; the linear model of η_0 was set to be the reference

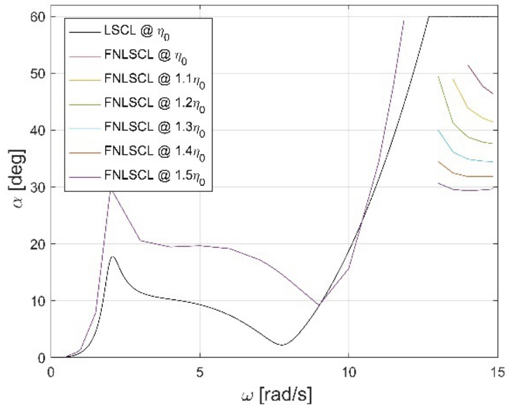

Figure 16. Comparison precession angle responses between non-linear and linear gyro-stabilizer models; the linear model of η_0 was set to be the reference

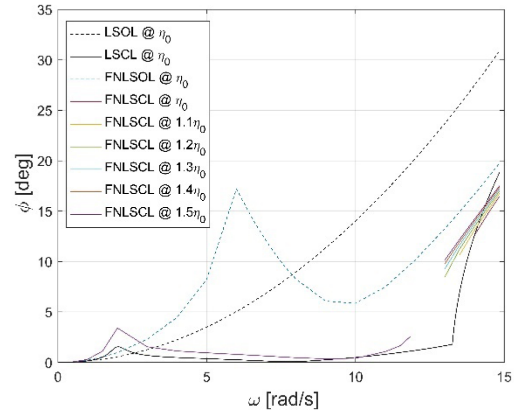

Figure 17. Comparison roll angle responses between non-linear and linear gyro-stabilizer models; the linear model of η_0 was set to be the reference

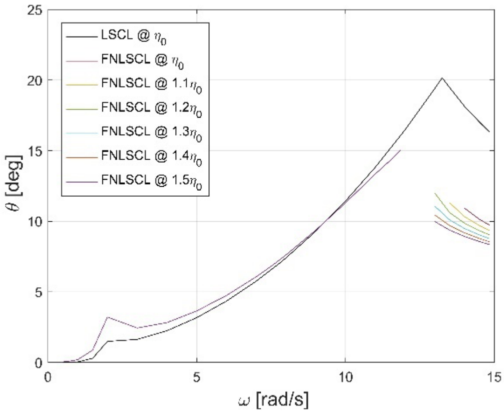

Figure 18. Comparison relative roll angle responses between non-linear and linear gyro-stabilizer models; the linear model of wave amplitude η_0 was set to be the reference

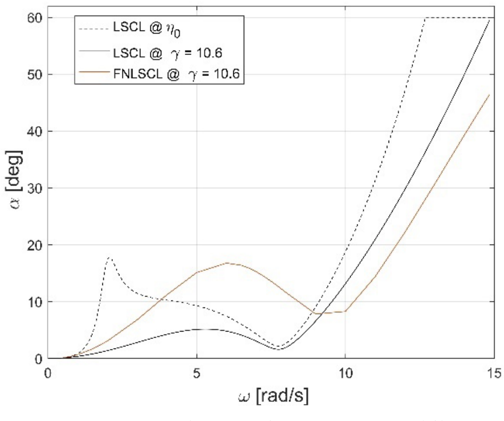

Figure 19. Precession angle responses of linear and non-linear gyro-stabilizer model of wave amplitude η_0 and fix γ =10.6

The non-linear behaviors were analysed and explained throughout frequency domain as they were mentioned above. However, in reality, a γ^* value cannot adjust base on frequency domain as following Figure 12; a frequency cannot know immediately in time domain. Thus a γ^* will be selected only one value from Figure 12 so that appropriate with operation requirements. The γ^* value of 10.6 was selected. It locates at the right end of line LSCL @ η_0. The value is the highest value, which forces the precession angle to work do not exceed the limited angle throughout the frequency range. Then the selected value was used for both linear and non-linear gyro-stabilizer system. The results were plotted follow as Figure 19 - 22 in frequency domain. In order to examine the effect of non-linearity, linear and non-linear gyro-stabilizer system model were simulated in irregular wave model of Bretschneider's [34] method that it has significant wave height of 0.04 m and the results were plot in Figure 23.

The following Figure 19, the precession angles of non-linear system work under the limited angle throughout frequency range. It has same characteristic of linear system but has different values. Hence, the roll angle response in Figure 20 is consequence of precession angle. The roll angle response of non-linear system has same characteristic of linear system but has different values as well.

Figure 21 shows the frequency response results. The peak of frequency response of non-linear open-loop system that refers to the natural frequency of vessel is different from linear open-loop system. The curve of linear closed-loop system is fair curve and approach to zero throughout the frequency range. The curve of non-linear closed-loop system has same behaviour of open-loop and its peak is lower. According to Figure 22, the reduction rates of linear and non-linear system are shown. The reduction rate refers to the efficiency of the stabilizer system. The non-linear system has the reduction rate values near linear system at the frequencies lower than 6 rad/s. But at the higher frequencies value, the reduction rate values of non-linear system are lower.

According to the previous results, the γ^* value was selected and fixed. They are made to clearly understand and proved that the non-linearity of non-linear model give a lot of different results at all. Thus, the designing base on linear model may give the wrong respond in reality. In order to prove again, the linear and non-linear gyro-stabilizer system models were simulated in same irregular beam sea on time domain. Assume that, precession angle is limited by mechanism at 90 degree but the γ^* value was selected from the limited angle at 60 degree of regular wave amplitude in order to let it has margin to prevent a

DOI: http://dx.doi.org/10.36956/sms.v3i1.316

damage when the gyro-stabilizer system get higher amplitude in irregular wave.

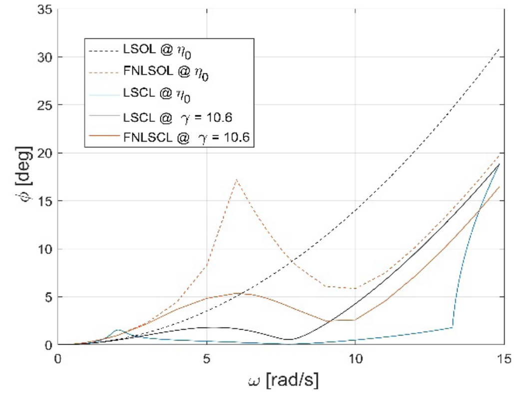

Figure 20. Roll angle responses of open and close loop condition of linear and non-linear gyro-stabilizer model of wave amplitude η_0 that the close loop model was set the fix value of γ =10.6

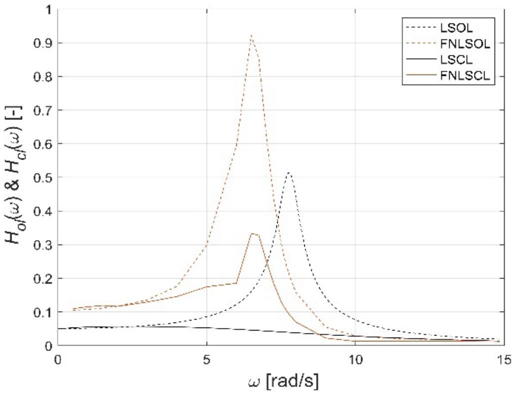

Figure 21. Comparison of frequency responses of open and close loop condition of linear and non-linear gyro-stabilizer model of wave amplitude η_0 that the close loop models were set the fix value of γ =10.6

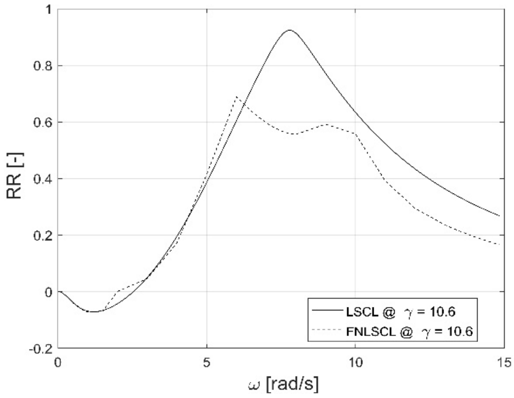

Figure 22. Comparison of reduction rate between linear and non-linear gyro-stabilizer model of wave amplitude η_0 that the close loop models were set the fix value of γ =10.6

In the following Figure 23, the setting of gyro-stabilizer simulation cases (linear and non-linear system) were simulated in irregular wave model. The gyro-stabilizers were switched off first, and then begin to switched on at 20 second of simulation time to observe the difference of behaviors when the gyro-stabilizer models were switch off and on. The systems performances were gathered and shown in Table 2 in root mean square. At the top of Figure 23, the exciting moments of linear and non-linear system were shown. They were induced from the same irregular wave model but it gave exciting moment amplitude and phase shift slightly difference. The RMS of exciting moment of linear model has the value less than non-linear model so that accord to Figure 15. When the stabilizer switched off, the vessel did not stabilize. The roll angle response of linear model shown at the middle of Figure 23 has the RMS value more than non-linear model slightly. These results accord to Figure 20. When the gyro-stabilizers were switched on, the precession began to move for stabilize the vessel, the roll angle responses were reduced. The precession angle responses were shown at the bottom of Figure 23. As the gyro-stabilizer switched on, the precession angle of linear model has RMS value more than non-linear accord to Figure 19. And the roll angle response of linear model has RMS value lower than non-linear model. However, the reduction rate (RR) of linear system has RMS value more than non-linear system and so very different.

As the mentioned these results, they clearly show that the designing via the linear model cloud makes the gyro-stabilizer system miss the design point of mission requirements. On the other hand, the non-linear system model cloud gives more approach to reality for designing follow mission requirements.

Table 2. The root mean square values (RMS) of gyro-stabilizer system performances in irregular beam sea according to Figure 23; the significant wave height and average wave frequency is 0.04 m and 10.68 rad/s respectively.

Model	τ_w [Nm]	α [deg]	ϕ [deg]	RR [-]
LSOL	14.5	-	21.56	-
FNLSOL	15.38	-	18.57	-
LSCL	14.5	32.03	4.75	0.78
FNLSCL	15.05	31.13	11.46	0.38

DOI: http://dx.doi.org/10.36956/sms.v3i1.316

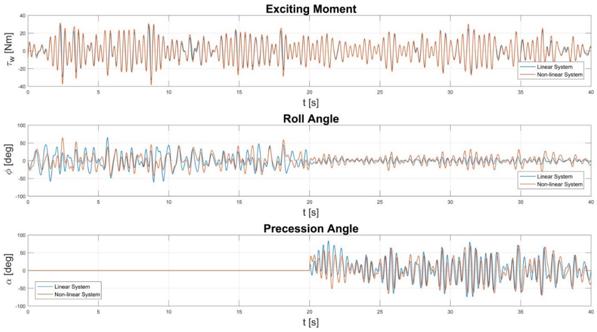

Figure 23. Comparision of linear and non-linear gyrostabilizer system model when they are swicthed off and on in irregular wave with γ =10.

5. Conclusions

A gyro-stabilizer is the interesting system that it can apply to marine vessels for diminishes roll motion. Today it has potentially light weight with no hydrodynamics drag and effective at zero forward speed. The twin-gyroscope was chosen for this presentation because of it not has side effect moment. Almost, the modelling for designing the system use linear model that it might not comprehensive mission requirement such as high sea condition (high wave amplitude and various frequencies). Thus, the non-linear model becomes important role because it able to give the interested results approach to reality more than linear model. The non-linearity analysis was proved by comparison the results between linear and non-linear model of gyro-stabilizer throughout frequency domain also same wave input, constrains and limitations. Moreover, they were cross-checked by simulating in time domain.

Actually, controller gains of the non-linear model cannot directly determine the appropriated turning gain K_d via frequency domain analysis. Hence the K_d of non-linear model was approximated by selecting the γ^* value so that resulted to K_d from linear model at the highest frequency value of selected wave amplitude. The comparison of interested results as wave exciting moment τ_w, precession angle α, roll angle response ϕ and reduction rate of linear and non-linear close loop model in frequency domain has demonstrated the similar characteristics but gave different values at same frequency obviously. The results were confirmed again by simulation in irregular beam sea on time domain and they demonstrate the difference of behavior of both systems while the gyro-stabilizer was switching on and off.

From the resulting analysis, the non-linear gyro-stabilizer model gives the results closer to realistic that correspond to more accuracy in a designing gyro-stabilizer control system for various amplitudes and frequencies operating condition especially high sea condition.

References

[1] Chadwick, J.H. (1955), “On the stabilization of roll”, Trans. Soc. Naval Arch. Marine Eng, 63, 237-280.

[2] Marzouk, O.A. and Nayfeh, A.H. (2009), “Control of ship roll using passive and active anti roll tanks”, Ocean Engineering, 36(9), 661-671.

[3] Haghighi, H. and Jahed-Motlagh, M.R. (2012), "Ship roll stabilization via Ssliding mode control and gyrostabilizer", Bul. inst. politeh. iai Autom. control Comput. sci. sect. J, 1, 51-61.

[4] Townsend N.C., Murphy, A.J. and Shenoi, R.A. (2007), “A New Active Gyrostabiliser System for Ride Control of Marine Vehicles”. Ocean Engineering, 34 (11-12), 1607-1617.

[5] Lewis, V.E. (1986), “Principles of Naval Architecture”. The Society of Naval Architects and Marine Engineers. Chapter IX.

[6] Lloyd, A.R.J.M. (1998), “Seakeeping Ship Behaviour in Rough Weather”. Ellis Horwood Ltd.

[7] Brennan, L. (1905), "Means for Imparting Stability to Unstable Bodies", US Patent 796893.

[8] Sperry, E.A. (1908), “Steadying device for vehicles”, Patent US 907907.

[9] Schilovski, P.P. (1909), “Gyrocar”, Patent GB 12021.

[10] Schilovski, P.P. (1914), “Gyrocar”, Patent GB 12940.

[11] Beznos, A.V., Formal’sky, A.M., Gurfinkel, E.V., Jicharev, D.N., Lensky, A.V., Savitsky, K.V. and Tchesalin, L.S. (1998). “Control of autonomous motion of twowheel bicycle with gyroscopic stabilization”, Proceedings—IEEE International Conference on Robotics and Automation 3, 2670-2675.

[12] Karnopp, D. (2002), “Tilt control for gyro-stabilized two-wheeled vehicles”. Vehicle System Dynamics, 37 (2), 145-156.

[13] Brown, H.B., Jr. and Xu, Y. (1996), "A Single-Wheel, Gyroscopically Stabilized Robot", Proc. of the 1996 IEEE Int. Conf. on Rob. And Autom, Minneapolis, Minnesota.

[14] Aubrun, J.N. and Margulies, G. (1979). “Gyrodampers for large scale space structures”, Technical Report, NASA CR-159 171.

[15] Woolsey, C.A. and Leonard, N.E. (2002), “Stabilizing underwater vehicle motion using internal rotors”, Automatica, 38 (12), 2053-2062.

[16] Schultz, C. and Woolsey, C.A. (2003), “An experimental platform for validating internal actuator control strategies”, In: IFAC Workshop on Guidance and Control of Underwater Vehicles, April 2003, Newport, South Wales, UK, 209-214.

[17] Sperry, E.A. (1910), “The gyroscope for marine pur-

DOI: http://dx.doi.org/10.36956/sms.v3i1.316

poses", Transactions of the Society of Naval Architects and Marine Engineers XVIII, 143-154.

[18] Schlick, E.O. (1904a), "Device for minimising the oscillatory movements of ships", Patent US 769493.

[19] Schlick, E.O. (1904b). "The gyroscopic effect of flywheels on board ship", Transactions of the Institute of Naval Architects, 23, 117-134.

[20] Forbes, T.C. (1904), "Device for steadying ships" Patent US 769693.

[21] Sperry, E.A. (1908), "Steadying Device for Vehicles", Patent US 907907.

[22] McGookin, M., Anderson, D. and McGookin, E. (2008), "Application of MPC and sliding mode control to IFAC benchmark models". In: UKACC International Conference on Control 2008, Manchester, UK.

[23] Perez, T. and Steinmann, P. D. "Analysis of Ship Roll Gyrostabilizer Control", Proceedings of the 8th IFAC International Conference on Manoeuvring and Control of Marine Craft, Guarujá (SP), Brazil.

[24] Masri, S.F., Chassiakos, A.G. and Cauchey, T.K . (1993), "Identification of nonlinear dynamic systems using neural networks", Journal of Applied Mechanics. 60(1), 123-133.

[25] Chassiakos, A.G. and Masri, SF (1996), "Modeling unknown structural systems through the use of neural network", Earthquake Engineering & Structural Dynamics, 25(2), 117-128.

[26] Liang, Y.C., Zhou, C.G. and Wang, Z.S. (1997), "Identification of restoring forces in non-linear vibration systems based on neural networks". Journal of Sound and Vibration. 206(1), 103-108.

[27] Liang, Y.C., Feng, D.P. and Cooper, J.E. (2001), "Identification of restoring forces in non-linear vibration systems using fuzzy adaptive neural networks". Journal of Sound and Vibration. 242(1), 47-58.

[28] Jang, T.S., Kwon, S.H. and Han, S.L. (2009), "A novel method for non-parametric identification of nonlinear restoring forces in nonlinear vibrations from noisy response data: A conservative system", Journal of Mechanical Science and Technology. 23(11), 2938-2947.

[29] Jang, T.S., Kwon, S.H. and Lee, J.H. (2010) "Recovering the functional form of the nonlinear roll damping of ships from a free-roll decay experiment: An inverse formulism", Ocean Engineering. 37, 14-15.

[30] Jang, T.S. (2011), "Non-parametric simultaneous identification of both the nonlinear damping and restoring characteristics of nonlinear systems whose dampings depend on velocity alone", Mechanical Systems and Signal Processing. 25(4), 1159-1173.

[31] Jang, T.S., Baek, H., Choi, S.H. and Lee S. (2011), "A new method for measuring nonharmonic periodic excitation forces in nonlinear damped systems", Mechanical Systems and Signal Processing. 25(6), 2219-2228.

[32] Pongduang, S., Chungchoo, C. and Iamraksa, P. (2020), "Nonparametric Identification of Nonlinear Added Mass Moment of Inertia and Damping Moment Characteristics of Large-Amplitude Ship Roll Motion", Journal of Marine Science and Application, 19(2), 17-27.

[33] Arnold, R.N. and Maunder, L. (1961), "Gyrodynamics and its Engineering Applications", Academic Press, New York and London.

[34] Bretschneider, C.L. (1959), "Wave variability and wave spectra for win-generated gravity waves", Technical Memorandum No. 118, Beach Erosion Board, U.S. Army Corps of Engineers, Washington, DC, USA.

Sustainable Marine Structures
http://ojs.nassg.org/index.php/sms/index

ARTICLE

Application of Fourth Industrial Revolution Technologies to Marine Aquaculture for Future Food: Imperatives, Challenges and Prospects

Sitti Raehanah M. Shaleh[1] Rossita Shapawi[1] Abentin Estim[1] Ching Fui Fui[1] Ag. Asri Ag. Ibrahim[2] Audrey Daning Tuzan[1] Lim Leong Seng[1] Chen Cheng Ann[1] Alter Jimat[2] Burhan Japar[3] Saleem Mustafa[1*]

1. Borneo Marine Research Institute, Universiti Malaysia Sabah, Kota Kinabalu, Sabah, 88400, Malaysia
2. Faculty of Computing and Informatics, Universiti Malaysia Sabah, Kota Kinabalu, Sabah, 88400, Malaysia
3. Korporasi Kemajuan Perikanan dan Nelayan (KO-NELAYAN), Wisma Pertanian Sabah, Kota Kinabalu, Sabah, 88994, Malaysia

ARTICLE INFO

Article history
Received: 25 May 2021
Accepted: 28 May 2021
Published Online: 10 June 2021

Keywords:
Food security
Aquaculture 4.0
Digitalization
Imitation seafood
Sustainable solutions

ABSTRACT

This study was undertaken to examine the options and feasibility of deploying new technologies for transforming the aquaculture sector with the objective of increasing the production efficiency. Selection of technologies to obtain the expected outcome should, obviously, be consistent with the criteria of sustainable development. There is a range of technologies being suggested for driving change in aquaculture to enhance its contribution to food security. It is necessary to highlight the complexity of issues for systems approach that can shape the course of development of aquaculture so that it can live-up to the expected fish demand by 2030 in addition to the current quantity of 82.1 million tons. Some of the Fourth Industrial Revolution (IR4.0) technologies suggested to achieve this target envisage the use of real-time monitoring, integration of a constant stream of data from connected production systems and intelligent automation in controls. This requires application of mobile devices, internet of things (IoT), smart sensors, artificial intelligence (AI), big data analytics, robotics as well as augmented virtual and mixed reality. AI is receiving more attention due to many reasons. Its use in aquaculture can happen in many ways, for example, in detecting and mitigating stress on the captive fish which is considered critical for the success of aquaculture. While the technology intensification in aquaculture holds a great potential but there are constraints in deploying IR4.0 tools in aquaculture. Possible solutions and practical options, especially with respect to future food choices are highlighted in this paper.

1. Introduction

Aquaculture has grown dramatically in the past five decades, with total fish production from this sector amounting to 82.1 million tons [1]. It is widely recognized as a potential sustainable solution for food security and an answer to the need for cost-effective animal protein with low-carbon and ecological footprint. Fish

---

**Corresponding Author:*
Saleem Mustafa,
Borneo Marine Research Institute, Universiti Malaysia Sabah, Kota Kinabalu, Sabah, 88400, Malaysia;
Email: saleem@ums.edu.my

DOI: http://dx.doi.org/10.36956/sms.v3i1.378

demand is projected to increase in the range of 112.1-114.1 million tons by 2030, requiring an additional 30-32 million tons of fish [2-4]. This is a great challenge that requires a real transformation. Landings from capture fisheries are unlikely to increase due to depletion of resources and impairment of ocean ecosystem [5]. Aquaculture production should increase to ensure adequate supplies.

Aquaculture has recently surpassed the capture fisheries in production and is expected to share 62% of the food fish by 2030 [6]. The incremental research and developments have been going on and have contributed significantly to positioning of aquaculture to where it stands today. However, it is inconceivable to meet this high level of demand without transformation. Because the seafood demand has outweighed production, there is a need for a fast-track approach to producing fish using disruptive innovations and technologies that hold promise for revolutionizing the aquaculture industry.

Fourth Industrial Revolution (or IR4.0) offers a range of technologies, and some can be adapted for aquaculture systems. It is appropriate to apply the term ‘Aquaculture 4.0’ to aquatic farming driven by these disruptive technologies. Some interesting work has appeared in this area [7-11]. When the sustainability is taking a center stage in food production, it is necessary to generate a strategic framework comprising the purpose or goals and drivers aligned with the United Nations’ Sustainable Development Goals (SDGs) to resonate with the global narrative.

Aquaculture 4.0 envisages more automation in selected functions, bridging the physical and digital operations through cyber-physical systems using computers for monitoring and algorithmically controlling different mechanisms and processes, and regulating the production by closed-loop data. Potential areas of application of Aquaculture 4.0 technologies are highlighted in this paper together with the reasons for transformation, challenges and prospects with special focus on future food choices.

2. Technology Intensification

Certain new terms such as ‘precision aquaculture’, ‘smart aquaculture’ and ‘digital farming’ are associated with technology intensification in aquaculture. These terms are often used interchangeably but there are subtle differences. Precision aquaculture refers to use of digital techniques in monitoring and optimization of the culture system. This implies regulating the supply of inputs in amounts exactly needed to prevent waste, reduce cost and minimize environmental impacts. Smart farming envisages application of information and data technologies in effective ways for better results. Digital aquaculture combines elements of precision aquaculture and smart aquaculture to advance the technology intensification for Big Data analysis, use of web-based platforms and machine learning among other innovative tools.

Disruptive innovations and technologies of Aquaculture 4.0 are believed to hold key to transforming aquaculture towards seafood security targets. A comprehensive review of the application of various technological tools, including sensors, robots, 3D prints, drones and artificial intelligence (AI) in aquaculture development has been published recently [12]. Aquaculture industries, and R & D organizations are giving increasing attention to embracing modern technologies wherever feasible and affordable. It is being considered as a way of making a major turnaround in aquaculture. Many disrupting solutions are aimed at achieving better output with reduced resource inputs, improved nutritional quality of the harvest, and compliance with the sustainability criteria. This will offer a fast-track approach to meeting the fish production targets through four possible ways:

- Greater intelligent automation of the various operations.
- Bridging the physical and digital world through cyber-physical systems using computers.
- Monitoring and algorithmically controlling different mechanisms.
- Regulating production steps by closed loop data.

Inputs for deployment of modern technologies are in the form of data collections through IoT concept such as wireless network sensors and the analysis of big data with the techniques of AI. For a start, some selective technologies can be tested for their potential outcomes in terms of sustainable production.

Aquaculture 4.0 is closely associated with the aforementioned technology-intensive aquatic farming. Fore [13] has outlined main steps in modern aquaculture systems (Figure 1) that are aimed at: 1) Improving the accuracy, precision and repeatability in the farming processes, 2) Facilitating a greater degree of automation or inbuilt controls in regular monitoring of the farming system, 3) Providing a dependable decision support system characterized by a computerized program for collecting and analyzing the data, and synthesizing information that can be used to solve the problem by computer algorithms or human intervention or both, and 4) Reducing dependencies on manual labor, and subjective assessments.

DOI: http://dx.doi.org/10.36956/sms.v3i1.378

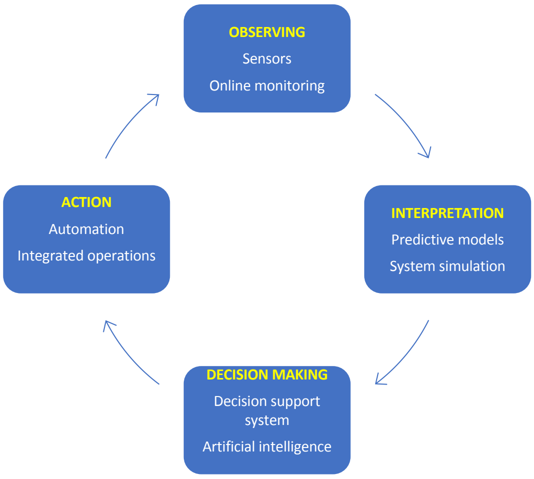

Figure 1. Key steps in the production process.

The overall objective through all these interventions is to improve productivity, resource efficiency, environmental sustainability and economic benefits. The fish stocked in cultural facilities should be able to perform and express its biological activities. These bio-responses need to be observed (Step-1) and interpreted for assessment of fish condition (Step-2) which will form the basis for making decisions on whether or not any interventions are needed (Step-3), and enforcing actions based on the decision for expected outcomes (Step-4). These steps in the production process can be assisted by appropriate technologies.

A model of digital aquaculture system comprising the various tools of technology is presented in Figure 2.

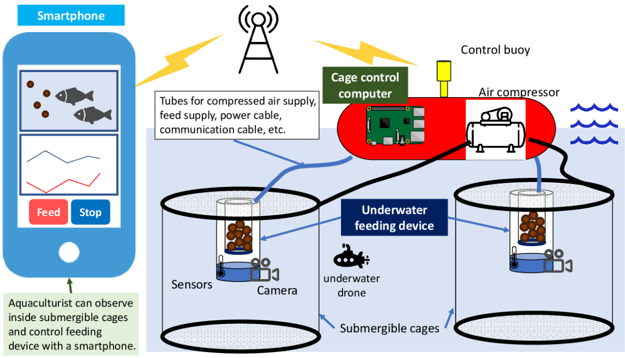

Figure 2. Model of a smart aquaculture system. Reproduced with permission from Tetsuo and Kobayashi [14].

System integration that involves connecting the various aquaculture sub-systems to function as a whole or complete unit of operation as can be seen from Figure 2 is the key to success of an intelligent aquaculture [15].

Among the Aquaculture 4.0 technologies, AI is receiving an increasing interest. In a complex system of aquatic food production, AI deployment can happen in many ways. It requires aligning the biological data with computers and understanding how the system works for solving specific problems. Basically, these procedures involve Artificial Neural Network (ANN).

ANN is a computational model inspired by neural network of the human nervous system. It mimics the pathways of brain function where the sense organs perceive stimuli that are transmitted through sensory nerves to the brain that decides how to respond to the stimuli and sends the information through motor nerves to the effector organs to act accordingly. This provides the foundation of AI where flow of information happens through algorithmic pathways.

ANN comprises Nodes which in biology are termed as Neurons (or nerve cells) [16]. There are multiple nodes arranged in three layers: Input Layer, Hidden Layer and Output Layer (Figure 3).

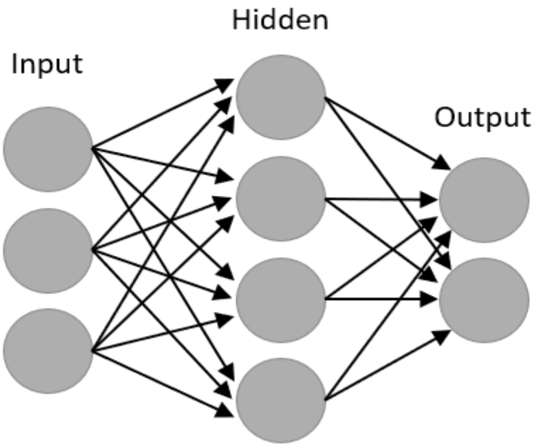

Figure 3. Three layers of nodes in ANN.

- Input layer: Comprises the Input Nodes that bring information from external environment into the network and pass it on to the hidden layer. Information processing and computation are not carried out here.
- Hidden Layer: Comprises nodes that have no direct connection with the outside environment (and hence the name 'hidden' nodes). Their role is to perform computations and to transfer the information to the output nodes.
- Output Layer: Consists of nodes that are responsible for transferring the information to the effector organs which act according to the instructions to produce the end-result or outcome.

Nodes from these adjacent layers have connections between them. When an input (stimulus) enters the node, it gets multiplied by a weight value [17]. Weight represents the strength of the signal (or impulse) and determines how much influence the input will have on the output. Weights are the real values associated with the stimulus. Because all inputs (stimuli) are not equal, therefore, weight values are different.

DOI: http://dx.doi.org/10.36956/sms.v3i1.378

Weights are applied within the nodes of the hidden layer. There is a system in the hidden layer called as an ‘Activation Function’ - that takes the input delivered by input nodes and multiplies it by Weight. Hidden layer also carries out distillation or filtration of inputs (information/ stimuli). It identifies and selects only the important information from the inputs, leaving out the information that is redundant or of no major consequence. If the input (impulse) is relevant and important (higher weight) it is processed for a response. If weights are close to zero, they have lesser importance and stimuli with such weights are filtered out while those of higher weights are retained and processed for response by the fish. There is one more entity called ‘Bias’ (b). Bias is added to the weighted sum and fed through Activation Function as a constant value (=1) which is the Bias Unit. By adding the value ‘1’ the Bias creates a non-zero y-intercept in the linear regression. This enables the ANN to fit the data when all inputs are equal to zero, or in other words, to generate an output when input is zero. It allows shifting linearity to either right or left to help the model to fit the given data. Diagrammatically, this pathway can be shown in Figure 4.

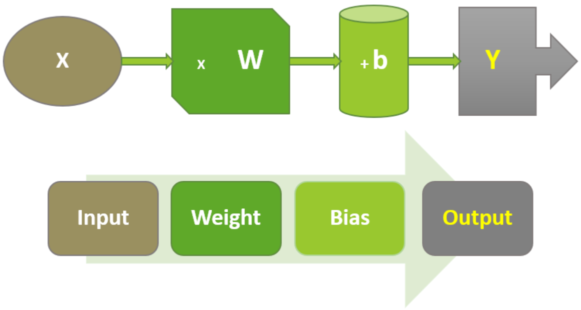

Figure 4. Response transmission pathway in ANN.

Mathematical transformation of this pathway can be expressed by the equation:

Input (X)→ x Weight (W) +Bias (b) → Output (Y).

Each input (X) is assigned a ‘weight’ (W) value based on its relative importance to all the other inputs. Transformation of input into valuable output forms the basis of mathematical constructs where the hidden layer is located between the input and output of the algorithm, and in which weights are applied to the inputs and directed through an Activation Function as the output. Bias is a mathematical entity that is applied to introduce non-linearity in the ANN model. Therefore, Bias is a constant which helps the model in a way that it can fit best in a regression and is an additional parameter in the neural network which is used to adjust the output along with the weighted sum of the inputs. In other words, Bias is an assumption made by a mathematical/ computer model to make the target function easier to process. Bias unit is not connected to or influenced by the input layer activity. It is a fixed value that is added but this role does not amount to any ‘real activity’ (unlike the weight). Thus, the steepness of the sigmoid curve depends on the weight of the inputs, not the Bias. This is evident from the simple formula:

Output = sum (inputs x weights) + bias

From a biological perspective it is better to explain that the Activation Function is not any structural or anatomical entity but a functional process in the form of mathematical equations that determine the output of a neural network [18]. All input values are close to Zero before weight is applied but once multiplied by weights and summed up they get accumulated, requiring rationalization to keep them in an acceptable range for appropriate output. Activation Function also helps in normalizing the output of each neuron. This envisages reorganization of weighted data and data cleaning by eliminating duplicate and redundant data. After normalization in the Activation Function, it is possible to generate output that is needed by a fish to respond to conditions it is exposed to.

As mentioned earlier, the node (neuron) receives a series of inputs (stimuli) and these are acted upon by Weight and Bias for transformation of input data in the hidden layer, and then the information moves into the next (output) layer of the ANN that tunes it to produce the desired outcome in a specified range for the effectors to react. Complexity of neuronal network requires such a normalization for a rationalized output. Since there are many factors in the cultural environment in which the fish is exposed, the simpler form of the equation: Input (X) x Weight (W) + Bias (B)→ Output should transform into the following formula:

Output, Y = f (X1 x W1 + X2 x W2 + X3 x W3) + b.

Neurons of the hidden layer apply the ‘Activation Function’ (f) to the weighted sum of the inputs because of which the fish responds differently according to the nature of stimuli and the needs of the situation. Activation Function provides the type of non-linearity between the inputs and outputs that is biologically logical under a real-world situation. It deserves emphasis that the linear models cannot characterize the nature of relationship between input and output. Without this (Activation Function), the ANN can only generate linear models that do not represent the practical possibilities because most real-world data is non-linear. Response of any aquaculture animal in a cultural system or even in the wild is inherently nonlinear in nature. To elaborate it further, it characterizes a situation where there is no straight-line or direct relationship between an independent variable and a dependent variable. ANN models the input-output that defines the complexity of the perception and processing of the response mechanism in the fish.

In ANN, the Weight and Bias can be considered as learnable parameters. In biological systems, this amounts to rationalization but in ANN these parameters (Weight and Bias) are randomized and adjusted toward the desired values for the correct output. This is where machine learning is involved. Because the hidden layer has many neurons and without activation function there will be a combined linear output in response to different inputs. If that is the case, fish response to multiple stimuli will be the same with full energy mobilized into it! Addition of Bias reduces the variance and hence introduces flexibility by addition of a constant value to the sum of Input + Weight. This is done by shifting the result of Activation Function towards the positive or negative side. Weight reflects the strength of the connection. It determines the amount of influence a change in the input will exert on the output. A low Weight value will have no change on the input, and alternatively a higher Weight value will markedly change the output. If Weight value is low, it means that the sensation (stimulus) is within the threshold limits of the fish, and it is not necessary for the fish to react.

3. Constraints and Options

The main factors constraining technology intensification are: 1) Reluctance to change, especially in the case of small enterprises, 2) Investment risk that weighs heavily in decision-making in large-scale enterprises, 3) Shortage of skilled human resources, and 4) Lack of gainful employment opportunities for graduates who have the knowledge for high-tech operations.

The prospects for aquaculture sector to transform would be brighter with the realization of the inability of the current systems to meet the fish production targets and when significant benefits from technology-intensive systems become apparent. Another reason which will influence market perception will be when the consumers demand to know the methods of growing food and tracer technology gains a foothold.

There are three directions for the future growth of aquaculture industry: Optimization of existing cultural systems, genetic modification and new species as future food.

3.1 Optimization of Existing Culture Systems

Aquaculture industry has a track record of improving the rearing systems. Knowledge and technological interventions have always supported the production and diversification of aquaculture. As a result, aquaculture has grown at the rate of 7.5 - 9 % annually to emerge as the fastest developing food sector [19,20]. Yet, barring a few selected species of fish, the success in commercial-scale seed production of even the high-value fish remains elusive. Most of the seed supplies still come from wild populations. Captive breeding of bivalve molluscs and sea cucumbers is not always successful. Commercial-scale production of lobster seed in hatcheries remains a challenge. Established aquaculture systems such as those for high-value finfish (groupers, seabass), shrimp and crab have been increasing production to meet the demand in the face of stabilization or decline of capture fisheries using the existing infrastructure. These systems require input of new knowledge for meeting the requirements of sustainable development.

3.2 Genetic Modification

Certain genetic modifications have demonstrated a quantum increase in fish growth. Growth rate of some transgenic fish can be increased by 400-600% while simultaneously reducing the feed input [21]. Genetically engineered tilapia has been reported to put on weight 300 % faster [22]. Genetically modified Atlantic salmon attains market size in half the time (16-18 months) compared to the conventional one that takes 32-36 months [23].

Potential candidate species are certainly those that fetch a high price in the market. In Malaysia and many other countries, the giant grouper (*Epinephelus lanceolatus*) is highly valued but so far there are no attempts for gene transfer in this species. Nevertheless, such high-value species remain possible candidates. Even with the state-of-the-art farming methods, good care in the hatchery and rich diet, the giant grouper could not gain 1 kg/year. Obviously, there are limits to growth. Growth can be modulated but it remains within the range set by the genetic and physiological factors. Giant grouper grows to 2.5 meters and attains 400 kg of body weight in about 35- 40 years or even more, gaining about 600 g/year or 1 kg/18 months [24]. Farmed groupers are reared for about for one year and are generally harvested for marketing when 400 - 600 g.

Producing genetically modified organisms (GMOs) is a controversial topic. Although market forces see benefits, but conservation biologists are concerned about the ecosystem implications of GMOs in case of their entry into the wild.

Consumer perception about GMOs is divided between acceptance and rejection. Resolution of this issue will take time. Future food security challenges and climate change

DOI: http://dx.doi.org/10.36956/sms.v3i1.378

adaptations will probably shape the cost/benefit analysis of genetically modified fish. For now, the aquaculture can remain focused on the non-controversial methods of production.

3.3 New Species as Future Food

While optimization of culture systems of currently used species will continue its transformation trajectory, new species can be tested for potential development as future seafood. Being new candidates, it will be easier to apply modern technologies for starting from scratch for sustainable production since it will be free from the legacies of the existing infrastructure and practices.

As a dynamic sector, aquaculture has been diversifying and adapting over time for better production and sustainability. However, now the food security challenges are different and require more efforts for screening new candidate species and selecting those that possess biological attributes needed for sustainable aquaculture. The criteria for selecting new species should be based on multiple qualities. Currently, out of 33,600 species of finfish recorded so far, only 608 species have been tried for aquaculture [3]. The number of invertebrate species is much higher. Of these, there are only 10 top farmed species, and this number includes shellfish as well as seaweeds in addition to finfish.

3.3.1 Criteria for Selection

❑ Adaptability to captivity at high-stocking density.

❑ High rate of survival and fast growth.

❑ Acceptance of artificial diets and nutritional efficiency.

❑ Ability of physiological systems to accept interventions aimed at developing farmed fish as functional food.

❑ Resilience to the effects of climate change and other external drivers.

❑ Amenability to farming in compliance with sustainability requirements.

❑ Consumer preference and marketability.

3.3.2 Advantages of Selecting New Species

(1) Aquaculture industry can make a fresh start, without the need for replacing the existing expensive culture infrastructure.

(2) Culture systems for the new species can be designed in response to prevailing challenges.

(3) Leveraging of past experience.

(4) New systems could offer scope for:

a) Disruptive innovations.

b) Green technology based on circular / decarbonized production models.

c) Potential for developing into functional seafood system through bioencapsulated ration or other means.

4. Tilapia (*Oreochromis niloticus*) as a Model

Tilapia (*Oreochromis niloticus*) is the subject of an ongoing study. It is a commercially important fish globally. Tilapia ranks among the top 10 farmed species in the world that are expected to drive future growth of aquaculture and is expected to yield 7.3 million tons a year by 2030 [6]. Being one the most thoroughly investigated finfish in the world, the data generated on its performance in culture systems offers a great deal of insights needed for AI application. Some basic attributes of tilapia specifically suitable for AI application in areas such as stress detection include:

❑ A strong receptor-effector system.

❑ Well-defined behavioral changes in response to environmental factors (stressors).

❑ Sensory systems having a remarkable ability of perceiving external stimuli and provoking reaction in a way that helps the fish adjust to the prevailing conditions.

Stress-detecting algorithms can help in timely mitigating stress and even prevention, and in optimizing culture conditions. Reducing stress on captive fish is vitally important for sustainable production [25].

The stress response of the fish has been documented by several authors in the past [26-34]. A simplified response of tilapia to stress factors is shown in Table 1. A real-life response system is complex, depending on many factors. The response is modulated by magnitude of stress factors and their possible interdependence, and duration of exposure. This should be considered in algorithm development. Still, such data provide a scientific basis for developing algorithms to detect and mitigate the stress factors for optimizing the culture conditions.

Table 1. Response of tilapia to stress factors.

Variable	*Fish response*
Temperature, °C	Decrease in opercular movement with temperature decline.
DO, mg/l	Reduced random movement, decline in swimming activity. Increased surfacing, crowding, sluggish response to stimuli.
Salinity, ppt	Increased opercular rate, increased vertical movement, disorientation, exhaustion, more time at bottom.
Unionized ammonia (mg/l)	Initial shock, increased agitation followed by decline, increased vertical movement, disorientation.

The fish is exposed to different stimuli at the same time

DOI: http://dx.doi.org/10.36956/sms.v3i1.378

in the culture system or wild environment and reacts as appropriate. The stress factors that serve as stimuli may be:

- ➢ Decline in dissolved oxygen
- ➢ Increase in nitrite and ammonia
- ➢ Rise in water temperature
- ➢ Visual factors
- ➢ Auditory factors
- ➢ Others

Their perception and transmission are depicted in Figure 5.

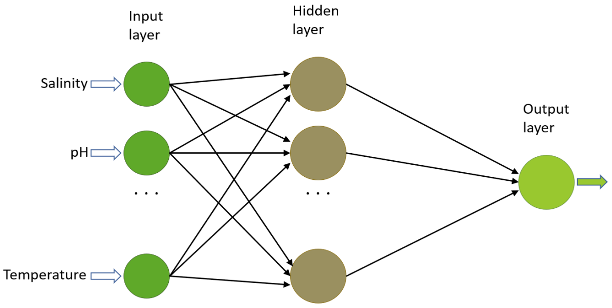

Figure 5. Architecture of multi-layer perception network for prediction of selected water quality parameters.

These stimuli are different in scale and in producing physiological effects in the fish. Their lethal effects are unequal. The stimulus-response, therefore, cannot be a linear process. Thus, in a real-world situation the fish cannot live with the same (or linear) response to factors that are profoundly different. Specific nature of visible response provides the basis of algorithm development. Learning from the fish's stimuli filtering system for response prioritization and modulating an effective outcome are necessary for mathematical constructs of AI. Just as there are different impulses or stimuli or stress factors, there should be multiple algorithms to perform the calculations on the input data to be able to compute the output (=biological response of fish). A biological ANN model that maps the inputs and outputs is complex and has a high level of dimensionality to factors such as dissolved oxygen deficiency, spike in ammonia concentration or change in salinity, thus requiring big data and analytics.

An Ongoing study on stress-detecting algorithm for Tilapia aquaculture optimization through artificial intelligence intervention consists of following components:

(1) Data collection: pH, temperature, salinity, and DO) 10 minutes for 1 month.

(2) Summation of the data.

(3) ANN design specifications.

(4) Network designing.

(5) Testing the ANN design by comparing the actual data with the predicated data output.

For practical purposes and prompt mitigation action, a real-time monitoring of cultural conditions through sensors and the fish's visible (behavioural) response through visual analytics will be required. Use of sensors will be for water quality measurement, but information of monitoring and assessment of fish behaviour and condition will also be very helpful in managing the cultural system. Production efficiency will be high if the fish is in a physiologically robust condition that supports faster growth and health.

The process would involve consolidation of sensor-generated data and computer (digital) vision through interactive interfaces that provide a scientific basis for timely action and data interpretation for Decision Support System (DSS). DSS is a computerized system for collecting and analyzing data, synthesizing the required information to support an efficient decision-making for solving problems in aquaculture systems. It will comprise integrated components in the form of: Physical objects ("things") such as sensors, software and other multiple technologies, real-time analytics and machine learning, stocked fish, and transfer of data over a network without human-to-human or even human to computer interaction. This defines the IoT in a digital aquaculture system with specific features for: Automation of control systems, real-time monitoring of water quality and stocked fish, reduced dependencies on technical personnel, doing away with subjective assessments and improved production efficiency.

5. Future Food Choices

As pointed out earlier, digitalization of existing aquaculture systems can be gradually increased, but it will be more practically convenient and cost-effective to develop aquaculture 4.0 systems for certain future foods, especially microalgae, seaweed and mushrooms.

There is nothing very technical about this popular term 'Future Food'. Some authors define it as food that we will be eating in 20 years' time, but it is better to refrain from fixing any year or decade as it seems arbitrary. Food security is a challenge for the world and is likely to get bigger in near future. What we will be eating in the future is a matter that is receiving a great deal of attention (Table 2). When it comes to seafood, we expect to consume:

(1) More of the same food that we are consuming now.

(2) Same seafood produced in different ways.

(3) Same seafood raised by different culture systems (for example. organic farming).

(4) New species as functional food.

(5) 3D-printed seafood.

DOI: http://dx.doi.org/10.36956/sms.v3i1.378

Table 2. Trends in future seafood.

Known types of foods currently harvested		**Advantages from future farming**
Species in the current production systems	*Species in the future production systems*	
Fish, shrimp, crab from capture fisheries or aquaculture.	Organic fish, shrimp, and crab produced through certified organic aquaculture methods.	Better for health.
Lobster from the wild population.	Hatchery-produced and farmed lobster.	Increase in supply. Decrease in overfishing pressure.
Fish farmed as primary food.	Fish as functional food through bioencapsulated/ fortified diet.	Specific health benefits.
Microalgae harvested from the sea.	Commercial-scale production under controlled conditions.	Exploring the potential of new species could open many horizons for their use as functional or regular food for humans.
Mushroom (Fungi).	Known or new species raised through agri-aquaculture systems "Mush-aquaculture".	Mushrooms are a source of nutraceuticals and therapeutic substances, and bioactive compounds of functional significance.

Application of AI and other tools of current technologies to future aquatic food is practically more plausible due to a number of reasons: 1) Opportunity to select species that can be grown on a fast track, 2) Determining amenability of new species to technology-intensive farming systems, 3) Shaping the production systems consistent with the sustainability requirements, and 4) Using species according to their: a) ability to accept nutrient fortification and bioencapsulation, b) qualities that make them acceptable as functional food when modulated, c) biological capacities for accepting integration into a system of macro-cascading for eco-friendly spinoff benefits or socio-economic dividends, and d) suitability for organic aquaculture. These topics have been elaborated in this paper.

6. Emerging Area: Imitation Seafood

There is a growing interest in imitation seafood. Several plant-based recipes for imitation fish are being developed, for example, raw tuna and salmon. The 3D printed imitation seafoods are opening a vast horizon of new opportunities. This is an area with enormous potential for:

☐ 'Secret' recipes
☐ Innovation
☐ Entrepreneurship
☐ Graduate employment
☐ Start-ups.

Making plant-based fish alternative will require interdisciplinary collaboration involving aquaculture, food science and technology, culinary art, psychology and economics.

Interdisciplinary research is making it possible to produce vegetable-based products that taste like a fish. With more efforts it might be possible to process tomato or other vegetables into a product that resembles the taste of grouper, hump-head wrasse or other species! This topic can inspire researchers of all ages and backgrounds to push the boundaries of innovation and entrepreneurship. However, momentum for such future foods should develop for the sake of human health, environment, creating new areas for entrepreneurship and life-long learning.

It requires changing the mindset. In the words of a protagonist of regenerative agriculture, Charles Massy "Today's problems cannot be solved with today's mind", and thus, we need to change our mindscapes before we can change our food security landscapes.

Promising sources of ingredients for imitation seafood are seaweeds and mushroom among others. Malaysia has a vast coastal marine area for seaweed farming. The growing conditions are favorable. Mushrooms are easy to farm under certain agri-aquaculture systems due to their survival and growing conditions in a tropical climate. They do not carry out photosynthesis and, thus, there is no need for vast sun-exposed areas. Fibrous nature of mushrooms offers the advantage to turn them into products that in some way resemble that from animal sources. Furthermore, mushrooms do not have a strong taste or flavour, and this helps in culinary processing for imitation. Use of mushrooms in such future foods will intensify interest in exploring the most suitable edible species out of the thousands that are known to occur.

There are good and bad practices that can be associated with the imitation seafood (Table 3).

Table 3. Good and bad practices requiring attention.

	Good practices
1.	Environment-friendly.
2.	Spare animals from the stress of captivity, cruelty and sacrifice.
3.	Free of seafood poisoning risk.
4.	Free of zoonotic infection concerns.
5.	Easy to manipulate nutritional and organoleptic quality by culinary processing.
6.	Easy to develop into functional food.
7.	Produced according to demand and save the product from loss in case of supply chain disruption.
	Bad practices
1.	Counterfeit food products containing false claims of functional properties or even containing harmful substances.

DOI: http://dx.doi.org/10.36956/sms.v3i1.378

7. Solutions

Quality control offers the best solution to curb malpractices in the imitation seafood business. Once the consumer interest picks up, the market is likely to expand and the public will be better informed. The nature of ingredients, quality assurance, price, awareness campaigns and consumer appeal will determine their success in the market. Certification procedures, traceability and blockchain will be needed to ensure that only quality product enters the market and consumers get what is claimed by the producers of the food item on the label. Blockchain has the capability to trace the entire lifecycle of food products from origin to consumers. It can help combat fraud in the food market, boost transparency in operations involved in processing. It will be possible to track and trace any seafood in the market and might emerge as the solution to the critically important food safety.

8. Conclusions

Aquaculture has grown rapidly over the recent decades. With the stagnation in capture fisheries landings, aquaculture should further enhance its contribution to seafood supply and food security. It has reached a stage that the trend of incremental change can shift towards transformation using IR4.0 technologies. There is an urgent need to examine if the current research and development efforts are following a system / systems / systemic or systematic approach. Investment in future food necessitates a serious introspection for an outcome-based and solution-oriented research that is linked to market demand and societal welfare, and is also rooted in environmental sustainability.

Acknowledgement

This study was supported by Aquaculture Flagship program of Universiti Malaysia Sabah.

References

[1] SOFIA. The state of world fisheries and aquaculture. Food and Agriculture Organization, Rome, Italy, 2020.

[2] Kobayashi, M., Msangi, S., Batka, M. et al. Fish to 2030: The Role and Opportunity for Aquaculture. Aquaculture Economics and Management, 2015, 19 (3), 282-300.

[3] Cai, J. and Leung, P.S. (2017). Short-term projection of global fish demand and supply gaps. Fisheries and Aquaculture Technical Paper no. 607, Food and Agriculture Organization, Rome, Italy, 2017.

[4] FAO. The state of world fisheries and aquaculture. Food and Agriculture Organization, Rome, Italy, 2018.

[5] Mustafa, S. and Saad, S. Coral Triangle: Marine biodiversity and fisheries sustainability. In: Leal Filho W., Azul A.M., Brandli L., Lange Salvia A., Wall T. (eds) Life Below Water. Encyclopedia of the UN Sustainable Development Goals. Springer, Cham, Switzerland, 2021.

[6] WB. Fish farms to produce nearly two-thirds of global food fish supply by 2030. The World Bank, Washington, DC, 2014.

[7] Mustafa, F.H., Bagul, A.H.B.P., Senoo, S. and Shapawi, R. A review of smart fish farming system. Journal of Aquaculture Engineering and Fisheries Research, 2016, 2 (4), 193 - 200.

[8] Vik, J.O. Digi Sal: Towards the digital salmon- from a reactive to a proactive research strategy in aquaculture. Norway University of Life Sciences, Oslo, Norway, 2016.

[9] Lu, H. D., Yu, X., & Liu, G. Q. Abnormal behavior detection method of fish school under low dissolved oxygen stress based on image processing and compressed sensing. Journal of Zhejiang University (Agriculture and Life Ences), 2018, 44(4), 499- 506.

[10] Chen, Y. Q., Li, S. F., Liu, H. M., Tao, P. Application of intelligent technology in animal husbandry and aquaculture industry. 14th International Conference on Computer Science & Education (ICCSE). IEEE, Toronto, ON, Canada, 2019.

[11] Helland, S. How digitalization is refining aquaculture research. The Fish Site. The Fish Site, Hatch Accelerator Holding Limited, Cork, Ireland, 2020.

[12] Mustafa,S., Estim, A., Shapawi, R., et al. Technological applications and adaptations in aquaculture for progress towards sustainable development and seafood security. IOP Publishing, Bristol, UK, 2021.

[13] Fore, M. Precision fish farming: A new framework to improve aquaculture, Part 1. Global Aquaculture Alliance. New Hampshire Avenue, Portsmouth, USA, 2019.

[14] Tetsuo, I. and Kobayashi, T. Smart aquaculture system: A remote feeding system with smartphones. Proceedings of the 2019 IEEE 23 International Symposium on Consumer Technologies, pages 93-96. DOI: v10.1109/ISCE.2019.8901026.

[15] Li, D. and Li, C. Intelligent aquaculture. World Aquaculture Society, Los Angeles, USA, 2021.

[16] Ogajanovski, G. Everything you need to know about neural netyworks and back propagation- machine learning easy and fun. Towards Data Science, Media, Canada, 2019.

[17] Alammar, J. A visual and interactive guide to the basics of neural networks. Creative Commons Attribu-

DOI: http://dx.doi.org/10.36956/sms.v3i1.378

tions, 2018.

[18] Nizrak, A. Comparison of activation function for deep neural networks. Yildiz Technical University, Istanbul, Turkey.

[19] SOFIA. The state of world fisheries and aquaculture Food and Agriculture Organization, Rome, Italy, 2018.

[20] IFFO. Aquaculture. IFFO Marine Ingredients Organization, London, UK, 2021.

[21] Towers, L. Importance of transgenic fish to global aquaculture- a review. The Fish Site, Hatch Accelerator Holding Limited, Cork, Ireland, 2016.

[22] Muir, W.M. The threats and benefits of GM fish. EMBO Report, 2004, 5 (7), 654 - 659.

[23] Williams, D. Genetically modified salmon to hit US markets. CGTN America, Washington, DC, 2019.

[24] Tucker, J.W. Species profile: grouper aquaculture. Southern Regional Aquaculture Center (SRAC), Publication No. 721. Fort Pierce, Florida, USA, Division of Marine Science Harbor Branch Oceanographic Institution, 1999.

[25] Aerts, J. Stress in aquaculture: a rough guide. The Fish Site, Hatch Accelerator Holdings, Cork, Ireland, 2019.

[26] Fernandes, M.N., Rantin, F.T. Relationships between oxygen availability and metabolic cost of breathing in Nile tilapia (Oreochromis niloticus): aquacultural consequences. Aquaculture, 1994, 27:339-346.

[27] Moreira, P.S.A. and Volpato, G.L. Conditioning of stress in Nile tilapia. Journal of Fish Biology 2004, 64, 961-969.

[28] Jian-yu, X., Xiang-wen, M., Ying, L. et al. Behavioral response of tilapia (Oreochromis niloticus) to acute ammonia stress no0nitored by computer vision. Journal of Zhejiang University. Science, 2005, 812 - 816.

[29] Xu, J., Liu, Y., Cui, S. et al. Behavioral responses of tilapia (Oreochromis niloticus) to acute fluctuations in dissolved oxygen levels as monitored by computer vision. Aquaculture Engineering 2006, 35, 207 - 217.

[30] Barreto, R.E., Volpato, G.L., Faturi, C.B., et al. Aggressive behaviour traits predict physiological stress responses in Nile tilapia (Oreochromis niloticus). Marine and Freshwater Behavior and Physiology, 2009, 42,109-118.

[31] Barreto, R.E., Miyai, C.A., Sanches, F.H.C. et al. Blood cues induce antipredator behavior in Nile Tilapia conspecifics. PLoSOne, 2013, 8: e54642.

[32] Hassan, M., Zakariah, M.I., Wahab, W. et al. Histopathological and behavioral changes in Oreochromis sp. After exposure to different salinities. Journal of Fisheries cand Livestock Production, 2013, 1, 103. DOI: 10.4172/2332-2608.1000103.

[33] King, M. and Sardella, B. The effects of acclimation temperature, salinity, and behavior on the thermal tolerance of Mozambique tilapia (Oreochromis mossambicus). Journal of Experimental Zoology Part A Ecological and Integrative Physiology, 2017, 327(7) https://doi.org/10.1002/jez.2113.

[34] Panase, P., Saenphet, S. and Saenphet, K. Biochemical and physiological responses of Nile tilapia, Oreochromis niloticus Lin subjected to cold shock of water temperature. Aquaculture Reports, 2018, 11, 17-23.

Sustainable Marine Structures
http://ojs.nassg.org/index.php/sms/index

ARTICLE

A CFD Study of the Resistance Behavior of a Planing Hull in Restricted Waterways

Ahmed O. Elaghbash[*]

RSC for engineering and naval architecture and consultancy, Sudan

ARTICLE INFO

Article history
Received: 25 June 2021
Accepted: 28 June 2021
Published Online:10 July 2021

Keywords:
Planing hull
High speed craft
Shallow water
Deep water
Solitary wave
Critical speed
Total resistance
CFD
Channel
Restricted water

ABSTRACT

The demand for high-speed boats that operating near to shoreline is increasing nowadays. Understanding the behavior and attitude of high-speed boats when moving in different waterways is very important for boat designer.

This research uses a CFD (Computational Fluid Dynamics) analysis to investigate the shallow water effects on prismatic planing hull. The turbulence flow around the hull was described by Reynolds Navier Stokes equations RANSE using the k-ε turbulence model. The free surface was modelled by the volume of fluid (VOF) method. The analysis is steady for all the ranges of speeds except those close to the critical speed range Fh =0.84 to 1.27 due to the propagation of the planing hull solitary waves at this range.

In this study, the planing hull lift force, total resistance, and wave pattern for the range of subcritical speeds, critical speeds, and supercritical speeds have been calculated using CFD. The numerical results have been compared with experimental results. The dynamic pressure distribution on the planing hull and its wave pattern at critical speed in shallow water were compared with those in deep water.

The numerical results give a good agreement with the experimental results whereas total average error equals 7% for numerical lift force, and 8% for numerical total resistance. The worst effect on the planing hull in shallow channels occurs at the critical speed range, where solitary wave formulates.

1. Introduction

In this chapter, try to interpret the operation theory of high speed craft which considers the planing hull as the main part of it. Also, it is displayed an objective, purposes of the research, and thesis structure.

1.1 High-speed Craft

Many researchers have tried to define high-speed vessels; the first one is Baird (1998) who says the speed of the ship up to 30 knots. Also, some hydrodynamicists say when the Froude number $Fn = U/\sqrt{g * L}$ above 0.4 such as high-speed monohulls and catamarans. Recently, definition of high speed craft, it means a craft that is operable on or above the water and has characteristics so different from those of conventional displacement ships, to which the existing international conventions, particularly SOLAS, apply, that alternative measures should be used to achieve an equivalent level of safety. In order to be considered a high speed craft, the craft must be

---

**Corresponding Author:*
Ahmed O. Elaghbash,
RSC for engineering and naval architecture and consultancy, Sudan
Email: men.aom90@gmail.com

http://dx.doi.org/10.36956/sms.v3i1.414

capable of a maximum speed equal to or exceeding V = 3.7 displ .1667, where V is the maximum speed and displ is the vessel displacement corresponding to the design waterline in cubic meters. The classification of high-speed vessels depends on the forces carrying them; Figure 1 shows these forces which support the vessels. On the left-hand side, show the vessels supported by air, which includes Air Cushion Vehicles (ACV), Surface-Effect Ships (SES) and wing-in-ground craft (WIG).

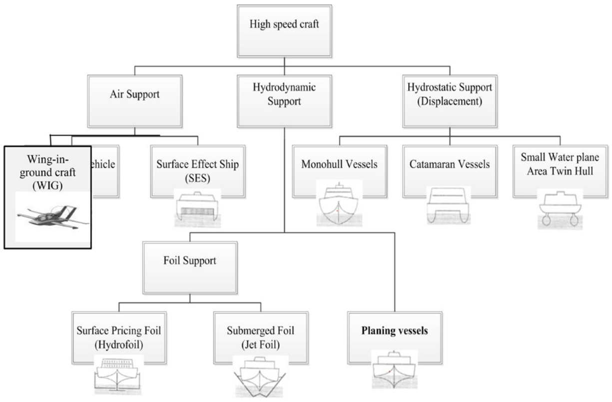

Figure 1. types of high speed craft

On the right-hand side, the Vessels are supported by a hydrostatic force which is given from the submerged part of the vessel (buoyancy), called Displacement vessels include conventional monohull, catamaran, trimaran, small water-plane-area twin-hull (SWATH). In between displacement vessels and air-supported, there is a hydrodynamics force supported vessels as a result of vessel forms such as planing hull or foil support including the surface pricing foil (Hydrofoil) and Submerged Foil (jet foil). They all suffer from the common problem of limited payload and sensitivity to wind and sea state. While each type of vessel has its unique characteristics depended to form of the vessel.

1.1.1 Wing-in-ground (WIG) Craft

Wing-in-ground (WIG) crafts are supported in their main operational mode solely by aerodynamic forces which enable them to operate at low altitude above the sea surface but out of direct contact with that surface. Accordingly, their arrangement, engineering characteristics, design, construction and operation have a high degree of commonality with those characteristics of aircraft. However, they operate with other waterborne craft and must necessarily utilize the same collision avoidance rules as conventional shipping. WIG craft is a multimodal craft which, in its main operational mode, flies by using ground effect above the water or some other surface, without constant contact with such a surface and supported in the air, mainly, by an aerodynamic lift generated on a wing (wings), hull, or their parts, which are intended to utilize the ground effect action [1]. WIG crafts are categorized according to the following types:

- Type A: a craft which is certified for operation only in ground effect. Within prescribed operational limitations, the structure and/or the equipment of such a craft should exclude any technical possibility to exceed the flight altitude over the maximum vertical extent of ground effect.
- Type B: a craft which is certified for main operation in ground effect and to temporarily increase its altitude outside ground effect to a limited height, but not exceeding 150 m above the surface, in case of emergency and for overcoming obstacles.
- Type C: a craft which is certified for the same operation as type B; and also for limited operation at altitude exceeding 150 m above the surface, in case of emergency and for overcoming obstacles.

IMO and the International Civil Aviation Organization (ICAO) have agreed that any WIG craft capable of sustained flight outside the influence of ground effect should also be subject to the rules and regulations of ICAO. Other crafts, including those with limited "fly-over" capability, should be covered only by the maritime regulatory regime.

1.1.2 An Air Cushion Vehicle (ACV)

An Air Cushion Vehicle is a vessel that is completely carried by air pressure, in the near vicinity to the surface. It is suitable for utility over earth or water. Its flexibility makes it a vehicle of choice in circumstances where region remoteness, insufficient water profundity, or need of shoreline facility. To hold the cushion of air under the boat, it is outfitted with an elastic seal called a skirt. Air leakage out from down the skirt compensated by lift fans. The air pressure under the boat should be a balance for load weight on the boat.

1.1.3 Surface Effect Ships (SES)

A Surface Effect Ship operates merely above water and a little portion displacement, about 10%, is propped by catamaran-similar side hulls. This sort of vessel features a shallow draft than a routine catamaran and due to the minimal displacement, makes significantly less wake. Cause to the fixed side hulls, a SES has elastic seals only at the stern and bow and demand lower lift capacity than an ACV.

1.1.4 Jet Foils and Hydrofoils

Jet foils and hydrofoils have a more profound displacement than SES, ACV, and trend to be steadier, giving a smoother traveler ride. Hydrofoils fly on wings in the water: whereas, hovercraft float on a layer of air above the water. Cause of their deeper displacement they are also more susceptible to damage from floating debris. Foils extend from movable arms that act as the lifting surface at operational speeds. The foils make a lift that completely raises the monohull out of the water. Hydrofoil parts can be partitioned into two main classifications, surface-piercing and completely submerged. A hydrofoil must be able to function securely while both hulls are borne mode and while takeoff.

1.1.5 Planing Hull Vessels

The vessel lifted by bouncy at Froude number under 0.4 is called a displacement ship. Whereas when carrying most of the weight of the ship by hydrodynamic force at Froude number above to 1 it's called a planing vessel. While the semi-planing vessel is in the range of Froude number between 0.4 and 1. Planing craft is employed as navy boats, racing boats, service boats, recreational boats, and ambulance boats. In general, the planing hull sailing with trim by stern means rise the bow and immerse the stern as a result of planing surface. Figure 2 shows the hydrodynamic force push the planing hull outer the water to reduce the resistance and increase the speed.

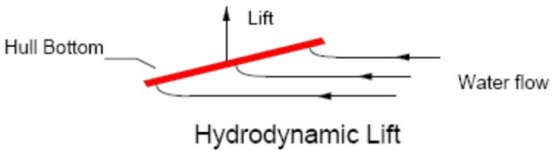

Figure 2. hydrodynamic lift of planing hull

1.1.6 Monohull Vessels

Adjusted from the army, the high execution monohull design can be seen in corvettes and destroyers. These vessels are distinguished by a slim limit hull, high speed, and the capacity to function in shifted climate conditions. Whereas exceedingly maneuverable, this sort of vessel is delicate to wind and wave activity unless stabilizers are utilized. The fast ship design is an illustration of a high execution monohull design, and Norasia is a case of a monohull with stabilizers. This design offers the highest cargo carrying capacity per ton. Most monohulls vessels work on comparatively lower ranges of speeds.

1.1.7 Catamaran Vessels

A catamaran vessel has two displacement hulls. It utilizes when required for a spacious area on the deck and high stability in sailing. This feature is comfortable for a passenger, and suitable for low-density cargoes. For that, it uses in fast ferries.

- Asymmetrical Catamarans: The more prevalent basic form of a multihull in the 1970s than nowadays. It is a monohull vessel with a slot cut out within the center.
- Symmetrical Catamarans: An amended catamaran design with many hull shape variations that feature two symmetrical hulls. This improves the performance and course keeping of the asymmetrical catamaran. This multihull is designed to move a range of displacement speeds semi-displacement speeds. Always, the level of the main deck is higher than operational waterline leading to improve sailing at rough sea, in comparison with Asymmetrical multihulls.
- Wave-Piercing Catamarans: this design populates by INCAT of Australia. It is asymmetrical multihulls with an elongated bow-section. The bow-section designs have many versions, notices hard taper at the end. It is designed to work under the waterline and the after sections operate in a displacement/semi-displacement mode. Since water is more stable on the underwater surface, the wave-piercing catamaran has excellent exposed water performance.

1.1.8 Small Water-plane Area Twin Hull (SWATH)

Small water-plane Area Twin Hull is considered an amendment of a catamaran design. Its design is recognized by two tubular immersed in water under hulls, fixed to the upper catamaran frame by slim struts. The torpedo-shaped hulls work beneath the waterline. The concept is to put the ship's buoyancy under the water surface and give minimal surface region at the waterline for waves to act upon, creating great sea-keeping capacity.

1.2 Objectives of Research

This work is shedding light on The CFD capability measurements to capture all phasic and phenomena in different waterways. Furthermore, the shallow channel hydrodynamic forces effect on planing prismatic hull compared with hydrodynamic forces in open water; this was conducted through a transition from displacement speed to planning speed.

1.3 Purposes of Research

The following questions are addressed in this thesis.

- How accurately can the hydrodynamic forces on a planing hull be predicted using CFD simulations?
- Do the CFD simulations yield any additional information that is not obtained from model testing?
- What are phenomena which occur in the free surface during moving the planing hull in different waterways for

http://dx.doi.org/10.36956/sms.v3i1.414

a transition from displacement to planing speed?

1.4 Thesis Structure

The thesis is divided into six chapters:

Chapter 1 includes the dividing of high-speed vessels depending on type of force which supported vessel, three main forces; Air support, hydrodynamic support, and buoyancy support. Also, it is displayed an objective and purposes of research, and thesis organization.

Chapter 2 includes the literature reviews of planning hull analysis techniques used to obtain hydrodynamic performance in various waterways. Besides, the Savitsky formula is applied to a prismatic planing hull is presented.

Chapter 3 Introduce the theory of planning hull, it explained the main characteristics and the form types of a planing hull. Also, it shows resistance types on a planing hull, and effect of confined water to wave pattern and viscous resistance.

Chapter 4 covered the steps of CFD analysis; domain dimension selection, boundary condition siting, and grid generation strategy which is used finite volume method for prismatic planing hull analysis, when sailing through the shallow channel and open water.

Chapter 5 discusses and validates numerical results obtained from a shallow water channel include wetted length, total resistance, hydrodynamic lift force, normal force, and wave pattern with experimental results. Also; compares total resistance and wave form with open water results.

Chapter 6 includes conclusion for sailing effect in various waterways of planning vessel and recommendations for future works.

2. Literature Review

This chapter reviews the techniques which using for planing hull analysis. Besides, the Savitsky formula is applied to a prismatic planing hull is presented.

2.1 Background

Recently, the simulation of the hydrodynamic performance of planing hull sailing in shallow water has become a common practice in the yachts building community. Hence, it is more used for the high-speed boats which sailing near to shoreline compared with where yachts used to navigate before. The high demand for high-speed boats operating near shore requires good knowledge of their behavior in three regions of speed, (subcritical, critical, and supercritical).

There are many methods to calculate hydrodynamic characteristics of planing vessels such as analytical experimental and numerical methods Figure 3 shows the most common of these methods including the numerical and experimental methods. The experimental methods require expensive facilities and measurement tools. These results increased cost and time compared with the numerical methods. Hence there has been an increase in the use of numerical methods for investigating the small boat resistance in different waterways such as shallow channels and open water. At the planing speed, the planing hull is supported by buoyancy force and lift force which put the hull in position, the wave-making resistance is the main component in the total resistance. The waves system includes the transverse wave and the divergent wave. The divergent wave angle starts for a 19.47 degree at subcritical speed (Kelvin wave pattern) and increases until 90 degrees at critical speeds after that decreases in supercritical speeds.

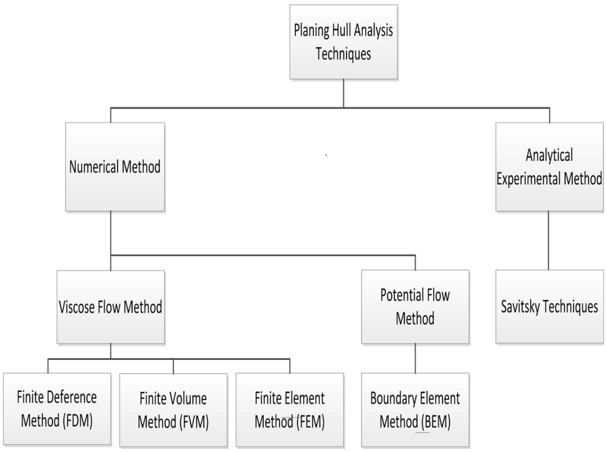

Figure 3. analysis approaches used for planning hull [2]

The first theoretical formula to consider the calculation of maximum pressure around planing 2D sections was proposed by Kerman [3], which was based on the conservation of momentum in the analysis. His work remained in use until equations for 3D planing surfaces by Savander and Scorpio [4] were introduced, which describes potential perturbation and vortex distribution around a planing plate.

The finite difference method was used to solve the Kadomtsev-Petviashvili equation for a TSS model moving near critical speed [5]. By using the technique of matched asymptotic expansions along with nonlinear shallow-water wave theory, the problem is reduced to a Kadomtsev-Petviashvili equation in the far-field, matched with a near-field solution obtained by an improved slender-body theory, taking the local wave elevation and longitudinal disturbance velocity into account. The ship can be either fixed or free to squat. Besides wave pattern and wave resistance, the hydrodynamic lift force and trim moment are calculated by pressure integration in the fixed-hull case; running sinkage and trim, by the condition of hydrodynamic equilibrium in the free-hull case. Many experiments were conducted in an attempt to calculate the force and the moment on the flat bottom hull in shallow water at fixed trim by Christopher [6]. Furthermore, the force and moment on a constant deadrise angle prismatic hull by Reyling [7] were obtained experimentally.

For series 62 hull form, residuary resistance was computed over a range of speeds from displacement speeds to planing speeds when the hull moving in shallow water and it was concluded that there is an increase in residual resistance at the subcritical speed range and a decrease at the supercritical speed range as compared to deep water. Besides, there was a resistance hump created at the maximum angle of trim and the highest value of sinkage.

The 2D+t potential flow method was used to investigate the performance of planing hulls in calm water and was compared with 3D Reynolds Navier Stokes Equation (RANSE) method by Iafrati and Broglia [8]. A comparison between the two solutions is established to understand the role played by three-dimensional effects, neglected within the slender body assumption. The analysis is focused on the evaluation of the free surface shape and of the pressure field acting on the hull surface. It is shown that a good agreement is achieved in terms of the free surface profile, corrected is applied to the 2D+t solution to account for the rise up of the water in front of the hull. The comparison in terms of pressure distribution reveals important three-dimensional effects in the very fore part of the hull, in the region about the separation point, and at the transom. These methods-based designs were presented, starting from a non-stepped hull configuration, a multiple-step solution was developed and an optimization of the unwetted aft body area behind the steps was performed. The goal of the optimization is drag reduction and dynamic stability [9]. The validation of the 2D+t model for single stepped planing hull with the experimental data in terms of; resistance, dynamic trim, and wetted surface area was carried out by Bilandi [10]. The obtained hydrodynamic results have been compared against the experimental data and it has been observed that the presented mathematical model has reasonable accuracy, in particular, up to Froude number 2.0. Furthermore, this mathematical model can be a useful and fast tool for the stepped hull designers in the early design stage to compare the different hull configurations. It should also be noted that the mathematical model has been developed in such a way that it has the potential to model the sweep-back step and transverse the vertical motions of single-stepped planing hulls in future studies.

The RANSE method was used to predict moment and force on a planing prismatic hull with a constant deadrise angle equal to 20 degrees by Brizzolara and Serra [11]. Results obtained, in terms of drag lift forces and longitudinal trimming moment, are compared with available experimental (model tests made at Hydronautics towing tank) and semi-empirical theories (Savitsky, Shuford, etc.) commonly used by a naval architect for the prediction of planing surface hydrodynamic performance. By the comparison of global force components and moments and the analysis of distributed parameters, such as pressure on the wetted hull, tangential stresses, spray root line, and wave elevations, some interesting conclusions can be drawn on the accuracy of CFD codes for the prediction of steady hydrodynamic performance of planing hulls.

Safari calculated; total resistance, added resistance, and wave pattern numerically for model 4667-1 by using CFD software based on finite volume method to solve the RANS equations in different speed and depths including deep and shallow water conditions. Also, the wave pattern and flow field around the vessel are investigated. For validating the method, at first, the resistance results in deep water are compared with the experimental data and show good agreements. Simulations are performed in transient mode, using Volume of Fluid (VOF) and k -ε schemes to model the free surface turbulent flow. The results have shown that by decreasing the depth, the shallow water-resistance of a planing vessel will be increased [12]. Mancini used this analysis to get; total resistance coefficients, wetted surfaces, and dynamic trim for the parent hull model (C1 hull) from the Naples Systematic Series (NSS), Form hull characterized by a warped bottom [13].

Moreover, heave motion, pitch angle, free surface deformation, and resistance of planing vessels were obtained through this analysis by Wang [14] in deep water.

The modern transverse stepped planing hull was investigated by CFD, which applies moving mesh techniques and large eddy simulation to find the total resistance, trim, and sinkage. These numerical results were validated with experimental results [15]. Moreover, Bakhtiari estimated; the numerical results of drag, pressure distribution, wetted surface, water spray, and wave generation by stepped planing hull [16]. Furthermore, the wake profile was compared by Savitsky and Morabito empirical formula. The morphing mesh method and k-ε model were used to simulate the fluid flow around the two-stepped hull moving freely to heave and pitch [17]. Also, this mesh technique was used to describe hydrodynamic characteristics around the tunneled planing hull and it's compared with experimental results [18].

The Smoothed Particle Hydrodynamics (SPH) method investigated the pressure distribution on the seafloor in very shallow water and, the change in the angle of created divergent waves over a range of speeds [19].

2.2 Savitsky's Method

This analysis for prismatic planing hull at fixed trim and fixed beam aims to find formulas for calculating the lift force, total resistance, wetted area, and center of pressure. There are two steps for this analysis, a simple case that imposes that all forces and moment affect in the center of gravity. Next, the general case includes lift, drag, and trust effect in a different point on the hull.

The equations are depended on huge experimental results. The lift coefficients equation following as [20]

$$\boldsymbol{C_{L\beta} = C_{L0} - 0.0065\beta C_{L0}^{0.6}} \quad (2.1)$$

And

$$C_{L\beta} = \frac{\mathrm{F_{L\beta}}}{0.5\rho U^2 B^2}$$

Also

$$\mathbf{C_{L0}} = \frac{\mathbf{F_{L0}}}{\mathbf{0.5\rho U^2B^2}} = \boldsymbol{\tau}_{\mathbf{deg}}^{\mathbf{1.1}}\left(\mathbf{0.01}\boldsymbol{\lambda}_{\mathbf{w}}^{\mathbf{0.5}} + \frac{\mathbf{0.0055}\boldsymbol{\lambda}_{\mathbf{w}}^{\mathbf{2.5}}}{\mathbf{Cv^2}}\right) \quad (2.2)$$

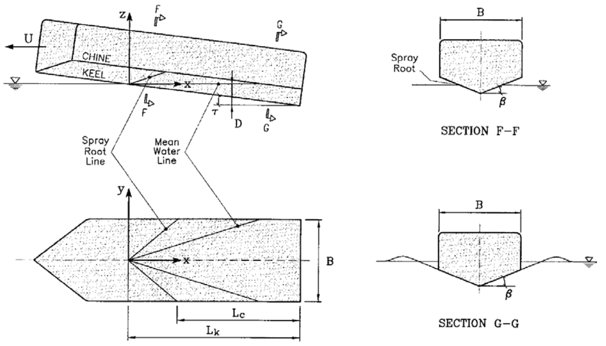

Figure 4. parameters for prismatic planing hull by Savitsky (1964)

Figure 4 interpreted the dimensions and trim angle τ and deadrise angle β which are used to define the Savitsky geometry. From Savitsky formula notices that the lift force and drag is quale zero when the planing hull even keel. The drag force can be found by

$$\mathbf{Rp = F_{L\beta}\tau} \quad (2.3)$$

The angle of trim has an important role to make the hull similar to a hydrofoil. It means that the hull has a drag force and lift. Moreover, the deadrise angle βis decreased lead to an increased lift force part. Finally, the longitudinal center of pressure calculates by

$$\frac{l_P}{\lambda_W B} = \mathbf{0.75} - \frac{\mathbf{1}}{\mathbf{5.21}C_v^2/\lambda_W + \mathbf{2.39}} \quad (2.4)$$

Where lp the distance from the stern to the center of pressure

The total wetted bottom area of a planning surface is actually divided into two regions. One is aft of the spray-root line, commonly referred to as the pressure area and the other is forward of the spray-root line, referred to as spray area. The pressure area is load carrying area of the planning bottom. The forward spray area contributes to the total drag but is not considered to support any portion of load. An enlarged sketch of flow direction on a deadrise surface is shown in Figure 5. It is found that the flow in the pressure area is predominantly aft with some transverse floe along the chines. The flow along the spray-root line is primarily along the direction of the stagnation line. In the spray wetted area the direction of the fluid flow are such that the space angle between oncoming fluid particles and stagnation line is equal to the angel between the direction of the spray jet and the stagnation line; for example any line of motion in the spray area is nearly a reflection about the stagnation line of the incidence velocity direction. Since the pressure in the spray area is nearly atmospheric, then, by Bernoulli, the spray velocity can be assumed to be equal to the planing speed.

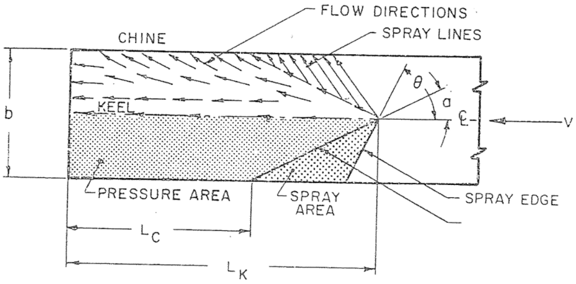

Figure 5. flow direction along planning prism and extent of spray area [20]

The total spray area, both sides, projected on a plane along the keel line is given by

$$\boldsymbol{A_s = \frac{b^2}{2}\left(\frac{tan\beta}{\pi tan\tau} - \frac{1}{4\, tan\Phi\, cos\beta}\right)} \quad (2.5)$$

The Savistly formula achieved good agreement with the experimental results but the CFD method work at a different type of modern hull shape and various waterways.

3. Planing Hull Theory

This chapter displays the main characteristic of the planing hull and the type's form of planing vessel. It is defined the concept and types of resistances. Also, it shows the effect of restricted waterways on wave-making resistance and viscous resistance.

3.1 Planning Hull Characteristic

The planing vessels sharing with Common features have a transom stern, bow carve, flat surfaces, hard chines, V shape at the transom, and maximum length does not exceed 30m. Figure 6 shows the main characteristics of

http://dx.doi.org/10.36956/sms.v3i1.414

the planing hull shape.

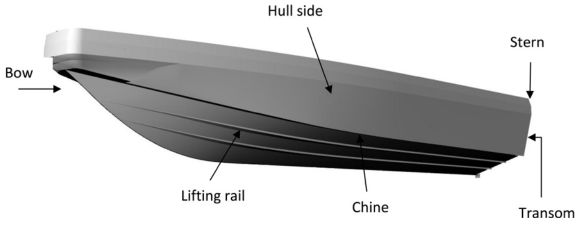

Figure 6. main planing hull characteristics

All the planing boat has one or more chine. It means the points crossing the bottom and hull-side. There are three types of chine; hard chine-like-angel, soft chine-like-carve, and reverse chine. A hard chine is meant to throw spray to the facets of the hull and to prevent water from flooding the hull where it will raise resistance. Chine with step has a considerable contribution of dynamic lift force. The soft chine gives smoother sailing for the hull compare with a hard chine boat. Whereas it is the maximum speed for hard chine boats higher than the soft chine boats [21].

Deadrise β is the angle a hull bottom makes with the horizontal plane viewed from ahead or astern. The right amount of deadrises gives a boat directional stability, a softer ride, and reduces wetted surface drag as the boat rises on a plane. Deadrise is said to be "constant" if it stays approximately the same from amidships to the transom. Deadrise is "variable" if it changes from a deep angle at amidships to a shallow angle at the transom.

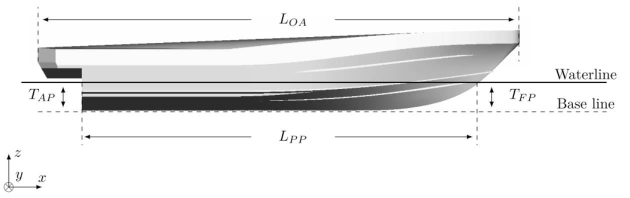

Figure 7. main dimension of planning hull

The dimensions of the planning hull are considered the part of hull characteristics shown in Figure 7.

L_{OA} Overall length of the planing hull measure the distance from bow to stern

L_{PP} Length between perpendiculars, it changes when the hull starts moving

T_{FP} Draft forward measure the vertical distance between the base line and waterline in a bow

T_{AP} Draft aft measure the vertical distance between the base line and waterline in a stern

The hull upright position, means don't movies is

$$T_{AP} = T_{FP}$$

Trimming angel θ when the planning hull start go forward the bow rising and stern immersed.

$$T_{AP} \neq T_{FP}$$

3.2 Planing Hull Type

The design of the planing hull boat improves with time to provide comfort, luxury, and increase the speed according to customer requirements and application of vessels. There are a lot of designs of planing to improve the performance of the hull.

3.2.1 Prismatic Planing Hull

The Fridsma hull was produced in 1969 by the Davidson Laboratory. Figure 8 shows the form of a prismatic hull in which the deadrise angle β is fixed in all the stations and was one beam in length. The bow had identical planforms and elliptical keel profiles. When the β equals zero the hull is called the flat bottom.

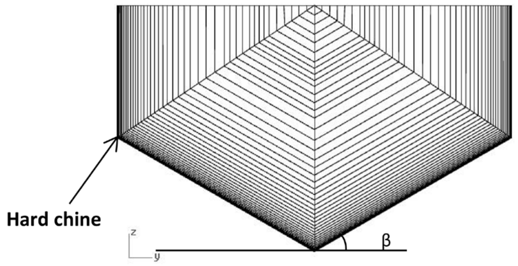

Figure 8. Prismatic Fridsma hull [22]

3.2.2 Warped Planing Hull

Figure 9 shows the warped hull in which the deadrise angle changes along the length of the hull, for that demand the change of angle along with any station. This gradual change of angles from bow to stern transom gets better comfortable on board and decreases fuel consumption on a warped hull compared with a prismatic hull in the voyage.

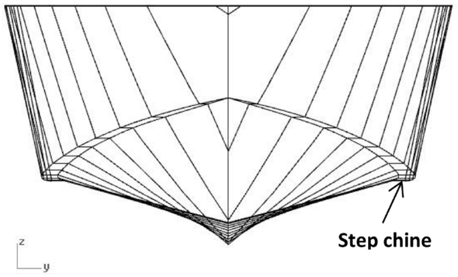

Figure 9. Warped hull of C945 models [23]

Through time the planing hull design developed to decrease the total resistance and increase the speed. For that on the warped bottom hull, a spray rail was added to improve which improves the performance of the planing hull by M¨uller-Graf (1991).

- Give more lift force due to the deflection of the spray.

- Decreases the spray frictional resistance to reduce the spray wetted area on the hull.
- Damping roll motion and more transverse stability.
- Increases deck dryness.

3.2.3 Tunneled Planing Hull

The tunnels divided the planning hull into three parts: the main hull and two side hulls. It is called a trimaran planning hull. Figure 10 shows the body plane of the tunneled planning hull. The tunnel gives an additional aerodynamic lift of the hull and less power required for racing.

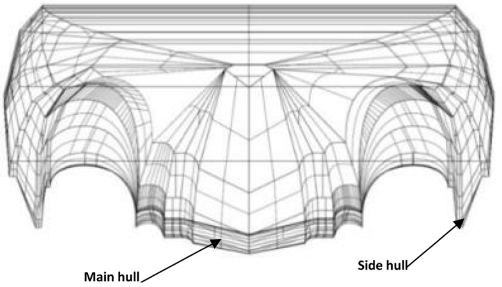

Figure 10. tunneled planing hull [18]

3.2.4 Stepped Planing Hull

The modern designs of the planing hull have one or more transverse steps on the hull bottom. The transverse step separates the flow of water and ventilates the aft part of the hull. This causes a reduction of the wetted surface area, which leads to decreased friction resistance and improves the lift per unit area. Furthermore, it gives damping pitch motion and improves pitch control. Figure 11 shows the planing hull with one transverse step. Approximately, the stepped planing gives good performance at the high-speed range $1.5 \leq Fn \leq 1.75$ and more drag at the displacement speeds compare with the same planing hull non-step.

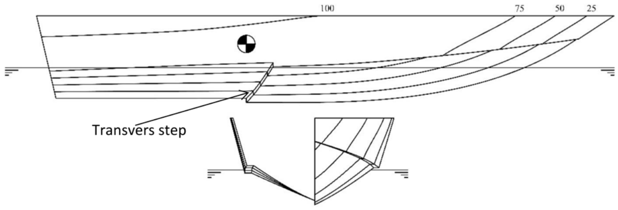

Figure 11. The C03 model buttock line and body plan [10]

3.2.5 Air Lubricated Planing Hull

This type of boat is a lot ordinarily referred to as a planing hull. When to move at high speed the bow lifts out of the water and is carried by the passage of air under that, whereas the stern is in a displacement mode and is carried by the seawater. It is sailing similar to small boats and private watercraft.

3.3 Planing Hull Resistance

The total resistance for bare planing hull in calm water R_T excludes the added resistance by sea wave and wind. It is equal to the sum of the air resistance, viscous resistance, spray resistance, and wave-making resistance.

$$R_{T=}R_A+R_V+R_S+R_M \qquad (3.1)$$

There is an effect of restricted waterways such as finite depth of water and baking effect. This waterway increases total resistance compared to the unrestricted waterway.

3.3.1 Air Resistance

The air resistance is very little value in which the density of air is much smaller than the density of water. Spatially at low speed can be neglected. The air resistance can be calculated by

$$R_A=0.5\rho_a c_D AU^2 \qquad (3.2)$$

Where ρa the density of air, $C_D$air frictional coefficient, A projected area on vessel above the waterline which facing the air, U speed of a vessel.

3.3.2 Viscous Resistance

The viscous resistance R_V concerns the main component of total resistance because its value depends on tangential force on the hull and vessel form. The viscous resistance includes frictional resistance, R_F viscous pressure resistance R_{VP} and Flow separation. The frictional resistance can be calculated by

$$R_F=0.5\rho C_F SU^2 \qquad (3.3)$$

C_F The frictional coefficient for smooth hull founded by the International Towing Tank Conference (ITTC) 1957 for model ship.

$$\mathbf{C_F = \frac{0.075}{(\log_{10}Rn-2)^2}} \qquad (3.4)$$

Reynolds number is equal whereas kinematic viscosity.

The factor (K) expresses all parameters related to the shape of the hull like the wake, the roughness of a surface, separation point, and eddies….etc.

$$R_V=(1+K)*R_F \qquad (3.5)$$

To explain the impact of fluid viscosity, boundary layer theory can be used. This means that viscosity matters only in a thin layer close to the surface of the hull. It is possible to use the two-dimensional boundary layer along a flat plate to define significant viscous flow characteristics.

A flat plate can be approximate the moistened hull surface. If we look at the flow following the ship from a reference frame, the ship's ward speed appears as an incident flow on a stationary hull with velocity U, as shown in Figure 12.

http://dx.doi.org/10.36956/sms.v3i1.414

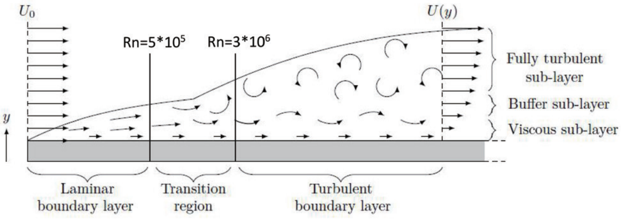

Figure 12. sachem of the boundary layer on a flat plate [24]

3.3.3 Spray Resistance

Almost, the spray resistance starts to occur at Froude number 0.5 and rapidly increases with speed. Its effect of the spray resistance was divided to pressure resistance component and frictional resistance by M¨uller-Graf (1991).

$$R_S=R_{SP}(Fn)+R_{SF}(R_n, W_n) \tag{3.6}$$

Where R_{SP} The function of Froude number, R_{SF} the function of the Reynolds number and Weber number

$$\boldsymbol{Wn=\frac{\rho V_{SR}^2 d_{SR}}{T_S}} \tag{3.7}$$

V_{SR} is the spray velocity, d_{SR} is the spray thickness, and *Ts* is the surface tension at the water-air interface. A representative value of *Ts*

3.3.4 Wave Making Resistance

The wave-making resistance R_M is the second major component of the total resistance. It is the resistance of a wave, which is generated by the vessel when it moves in calm water. Three factors affect wave-making resistance: speed of the vessel, underwater hull form, and depth of water. The last factor that has a strong influence on Froude depth equal to one. The wave-making resistance cannot be easygoing for calculating it, like viscous resistance. Kelvin (1887) explain the waves system established when the pressure point moving in deep water. There are two types of waves. Figure 13 shows the divergent wave and the transverse wave in deep water. The crest divergent wave slopes 19.28° from the centerline. While the transverse wave perpendicular to the centerline 90°. However, it recently shows that this angle can be significantly smaller at large Froude numbers [25].

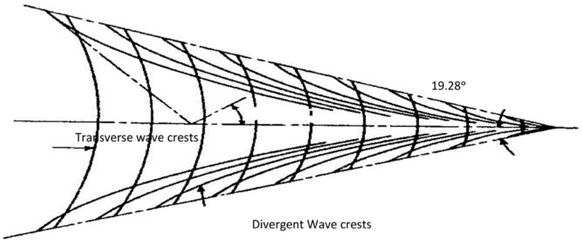

Figure 13. The Kelvin ship wave pattern in deep water. The included half-angle 19◦28_ of the waves is called the Kelvin angle and is affected by the water depth [26]

3.4 Restricted Waterways Effect

The restricted waterways like the channels, lakes, harbored, and so on. Have effects on the total resistance, because there is a restriction on the depth of water and width or both. show the depth Froude number F_h makes the essential role in divide the range of speed into three regions in shallow water

$$\boldsymbol{F_h = U/\sqrt{g*h}} \tag{3.8}$$

- $F_h < 1$ the region of subcritical speed the wave pattern like in deep water.
- $F_h \approx 1$ the region of critical speed the divergent wave angle equals 90.
- $F_h > 1$ the region of supercritical the divergent wave angle equals 45 and disappear the transverse wave.

3.4.1 Effect on Wave-making Resistance

In shallow water, when increases the Froude depth F_h the wave angle modified means that change the angle of divergent wave and transverse in waves system shown in Figure 14. That is a modification in the wave system as a result of wave retardation which means the wave speed in shallow water decrease than the deep water. All of that leads to a change of wave-making resistance in shallow water. Especially, at critical speed in a shallow water channel can show the solitary waves. When Froude depth was equal to 1, the speed of the ship was equal to the speed of the wave, which can be calculated by

$$\mathbf{U=\sqrt{g*h}} \tag{3.9}$$

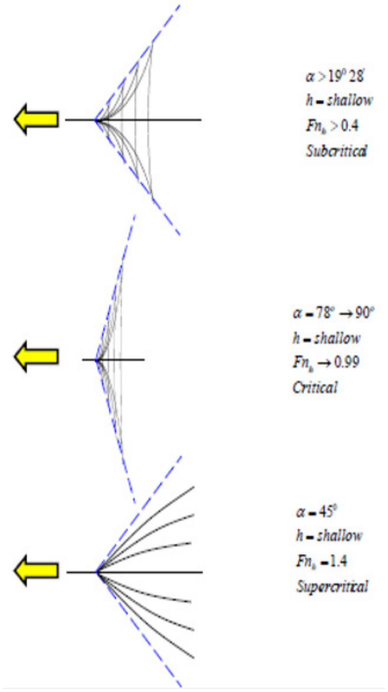

Figure 14. wave pattern change in shallow water

http://dx.doi.org/10.36956/sms.v3i1.414

3.4.2 Effect in Viscous Resistance

In shallow water, according to throttling the flow between the seabed and bottom hull, The fluid flow under the vessel increased speed and decreases pressure supported the hull, it's called the backflow effect, the fluid speed rises leads to enhancement skin friction resistance, whereas decreases water pressure under the hull, its changes the position of the hull.

Squat phenomena definition is combined between sinkage and trim when the hull moving in shallow water, sinkage resulting from pressure dropping under the hull. It causes a change of water plane area and moves center of gravity. If the center of gravity union with from center of buoyancy, the hull is upright. When the center of gravity move from the center of buoyancy, a trim angle is established between them. For all that, squat effect to:

- Increases the total resistance, viscous resistance, and wave-making resistance when the vessel sailing forward.
- The ship sailing slow-speed and has been losing part of maneuvering and steering.
- There will be a drop in speed in shallow water as a result of increased resistance and reduced propulsion efficiency.
- There is a greater tendency towards vibration as a result of propeller-induced vibration.

A range of planing speed the hydrodynamic lift force work opposite direction to sinkage force. So the sinkage force reduces the buoyancy force which shares in put the planing hull in position.

4. Methodology of Analysis

In this chapter, the methodology used in the CFD analysis is described. The chart in Figure 15 shows the CFD results validation with experimental data. The work is started by defining the numerical domain dimensions. And then mesh elements are generated and boundary conditions for the numerical domain are set to carry out the analysis and obtain the results. Post-processing results are then assessed by comparing them to experimental data. If the results are in agreement with the experimental data the analysis is finished. Otherwise, modifications on mesh and setup are applied in the new analysis boundary condition and regenerating the mesh to make the new analysis until getting valid results.

4.1 Finite Volume Method

In this research work, the finite volume RANS code ANSYS CFX was used to study the flow around a small planing hull craft in a shallow water channel to predict the hydrodynamic forces and wave patterns of the hull at subcritical, critical, and supercritical speeds.

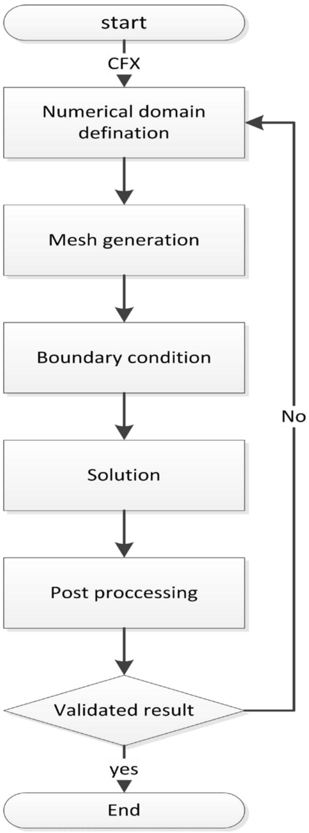

Figure 15. flow CFD analysis simulation

The motion of a viscous fluid is governed by the Navier-Stokes equations, which are valid both for turbulent and laminar flow. For an incompressible, Newtonian fluid in three dimensions under the influence of an external gravitational field, [27] the Navier-Stokes read.

$$\frac{\partial U_i}{\partial x_i} = 0.0$$

$$\frac{\partial U_i}{\partial t} + U_j \frac{\partial U_i}{\partial x_j} = -\frac{1}{\rho}\frac{\partial P}{\partial x_i} + \nu \frac{\partial^2 U_i}{\partial x_j \partial x_j} + g_i \qquad (4.1)$$

Here, the equations are formulated using tensor notation. The indices i and j in the Navier-Stokes equations run over the spatial coordinates x, y, and z. In these equations, U_i is the velocity in direction i, xi is the spatial coordinate in dimension i, t is time, ρ is the density, P is the pressure, ν is the kinematic viscosity and g_i is the gravitational acceleration.

The finite volume method (FVM), is a numerical method of discretizing a continuous partial differential equation (PDE), into a set of algebraic equations. The first step of discretization is to divide the computational domain into a finite number of volumes, forming what is called a mesh or a grid. Next, the PDE is integrated into each volume by using the divergence theorem, yielding an algebraic equation for each cell. In the centers of the cells, cell-averaged values of the flow variables are stored in so-called nodes. This implies that the spatial resolution of the solution is limited by the cell size since the flow variables do not vary inside a cell [28]. The FVM is conservative, meaning that the flux leaving a cell through one of its boundaries is equal to the flux entering the adjacent cell through the same boundary. This property makes it advantageous for problems in fluid dynamics [29].

A stationary transport equation involving diffusion and convection of a general flow variable, variable, φ, can be written as

$$\rho U_i \frac{\partial \phi}{\partial x_i} = \frac{\partial}{\partial x_i}\left(\Gamma \frac{\partial \phi}{\partial x_i}\right) + S(\phi) \tag{4.2}$$

Where Γ is the diffusivity and S is a source term that may depend on . By using the FVM, this equation can be written in discrete form as

$$a_P \phi_P = \sum\nolimits_{nb} a_{nb} \phi_{nb} + S_U \tag{4.3}$$

Where

$$a_P = \sum\nolimits_{nb} a_{nb} - S_P \tag{4.4}$$

In these equations, where the summations run over all the nearest neighbors of each cell, φ_P is the value of the flow variable in the present cell and φ_{nb} are the values of the flow variable in the neighboring cells. S_U and S_P are the constant and flow variables depending on parts of the source term, respectively. Furthermore, a_P is the discretization coefficient associated with the present cell, and are discretization coefficients describing the interaction with its neighboring cells. The discretization coefficients depend on the discretization schemes used to approximate the values of the flow variables on the cell boundaries, also known as cell faces. By using appropriate discretization schemes to determine the coefficients, a set of algebraic equations for the cell values is obtained.

4.2 Turbulence

When a hull is moving through the water, the flow around the hull is turbulent. In this section, the governing equations of turbulent flows are presented and turbulence modelling is explained.

4.2.1 Turbulent Flow

Turbulence has no physical definition, but it is characterized as a three-dimensional, irregular flow where turbulent kinetic energy is dissipated from the largest to the smallest turbulent scales. On the smallest turbulent scales, known as the Kolmogorov scales, the energy is dissipated into heat due to viscous forces. Since turbulence is a dissipative phenomenon, energy must be continuously supplied to maintain a turbulent flow.

Analytical solutions to the Navier-Stokes equations only exist for a limited number of simple cases such as laminar flow between flat plates. For turbulent flows in engineering applications, analytical solutions do not exist and the Navier-Stokes equations must be treated numerically. If they are solved using direct numerical simulation (DNS), the velocity field of the flow is obtained. However, since turbulence occurs on a wide range of time and length scales, DNS requires very high temporal and spatial resolutions to capture all the details of the flow. Thus, DNS is very computationally expensive and time-consuming which limits the method to special applications such as academic research or simulation of simple flows.

4.2.2 Turbulence Modelling

The most common way of treating turbulence is to use turbulence models in which the turbulent features of the flow are not resolved in time. By performing Reynolds decomposition, the instantaneous velocity and pressure can be decomposed as

$$\begin{aligned} u &= U_i + \overline{U_i} \\ p &= P + \overline{P} \end{aligned} \tag{4.5}$$

Where $\overline{U_i}$ and $\overline{P}$ denote the time-averaged quantities while U_i and p are the fluctuating components of the velocities and the pressure. By inserting the Reynolds decomposition into the Navier-Stokes equations given in equation (4.1), the Reynolds averaged Navier-Stokes (RANS) equations are obtained. These are written as

$$\frac{\partial \overline{U_i}}{\partial x_i} = 0.0$$

$$\frac{\partial \overline{U_i}}{\partial t} + \overline{U_j} \frac{\partial \overline{U_i}}{\partial x_j} = -\frac{1}{\rho} \frac{\partial \overline{P}}{\partial x_i} + \nu \frac{\partial^2 \overline{U_i}}{\partial x_j \partial x_j} - \frac{\partial \overline{u_i u_j}}{\partial x_j} + g_i \tag{4.6}$$

It can be noted that the RANS equations are very similar to the Navier-Stokes equations except for the additional term including $u_i u_j$, referred to as the Reynolds stress tensor. If the Reynolds stress term is modelled, the RANS equations describe the time-averaged flow quantities which require substantially less computational resources in comparison to DNS.

A common approach for modelling the Reynolds stress tensor of the RANS equations is to use the Boussinesq approximation. In this assumption, the Reynolds stress tensor is modelled as a diffusion term by introducing a turbulent viscosity, νt, according to

$$-\overline{u_i u_j} = v_t \left(\frac{\partial \overline{U_i}}{\partial x_j} + \frac{\partial U_j}{\partial x_i}\right) - \frac{2}{3} k \delta_{ij} \tag{4.7}$$

In this equation, δij is the Kronecker delta which assumes a value of 1 if i = j and 0 otherwise, and k is the turbulent kinetic energy defined as

$$k = \overline{\frac{1}{2} u_i u_j} \tag{4.8}$$

By using a model to describe how the turbulent viscosity depends on the flow, the RANS equations can be solved. The so-called two-equation turbulence models, such as the k-ε model and the k-ω model, use two additional

http://dx.doi.org/10.36956/sms.v3i1.414

transport equations to describe the turbulent viscosity. They are referred to as complete models since they allow the turbulent velocity and length scales to be described independently [30].

4.2.3 Turbulence Model Standard k-ε

The stander k-*ε* model reported by Launder et al., to obtain turbulent viscous using transport equation for turbulence kinetic energy k

$$\frac{\partial(\rho k)}{\partial t}+\frac{\partial(\rho k\bar{U}_i)}{\partial x_i}=\frac{\partial}{\partial x_j}\left(\left(\mu+\frac{\mu_t}{\sigma k}\right)\frac{\partial k}{\partial x_i}\right)+P_k-\varepsilon\rho \qquad (4.9)$$

And transport equation for dissipation rate ε

$$\frac{\partial(\rho\varepsilon)}{\partial t}+\frac{\partial(\rho\varepsilon\bar{U}_i)}{\partial x_i}=\frac{\partial}{\partial x_j}\left(\left(\mu+\frac{\mu_t}{\sigma\varepsilon}\right)\frac{\partial\varepsilon}{\partial x_i}\right)+\frac{\varepsilon}{k}(C_{\varepsilon 1}P_k-C_{\varepsilon 2}\varepsilon\rho) \qquad (4.10)$$

To obtain

$$\mu_t=C_\mu\frac{\rho k^2}{\varepsilon} \qquad (4.11)$$

Where

σk, $\sigma\varepsilon$ and C_μ are model constants

$C_{\varepsilon 1}$ and $C_{\varepsilon 2}$ are variable coefficient for the model

P_k is the production due to mean velocity shear

Table 1 shows the model coefficients improved during the time by a group of scientists.

Table 1. model coefficients improve with time

model	years	C_1	C_2			
Launder and Jones	1972	1.55	2	1.3	1	0.9
Sharma and Launder	1974	1.44	1.92	1.3	1	0.9
Spalding and Launder	1974	1.44	1.92	1.3	1	0.9

The turbulence *k-ε* has a reasonably accurate and computational cost per iteration compare with most anther turbulence models, resulting in that it used the engineering turbulence model for industrial applications. There is constrain for turbulence model at a wall, strong separation, curvature and large streamline for that must be using the wall function.

4.2.4 Turbulence Model k-ω

The turbulence model *k*-ω reported by Wilcox [31]. It has a transportation equation for kinetic energy *k* and specified dissipation *ω*, this specific dissipation has a relation to dissipation *ε* according to

$$\omega\propto\frac{\varepsilon}{k} \qquad (4.12)$$

$$\frac{\partial k}{\partial t}+\frac{\partial}{\partial x_i}(k\bar{U}_i)=\frac{\partial}{\partial x_j}\left(\left(\nu+\frac{\nu_t}{\sigma_k^{\omega}}\right)\frac{\partial k}{\partial x_j}\right)+P_k-\beta^*k\omega \qquad (4.13)$$

And transport equation for

$$\frac{\partial\omega}{\partial t}+\frac{\partial}{\partial x_i}(\omega\bar{U}_i)=\frac{\partial}{\partial x_j}\left(\left(\nu+\frac{\nu_t}{\sigma_\omega}\right)\frac{\partial\omega}{\partial x_j}\right)+\frac{\omega}{k}(C_{\omega 1}P_k-C_{\omega 2}k\omega) \qquad (4.14)$$

To obtain

$$\nu_t=\frac{k}{\omega} \qquad (4.15)$$

Where

β^*, , σ_ω, $C_{\omega 1,}$ and $C_{\omega 2}$ are model constants.

The merits of this turbulence model have good work near the wall and low turbulent regions [29]. Hence, it is valid too in the regions of turbulent Reynolds number locale near to the wall, lead to that the transport equations can be utilized within the entire stream space. The disadvantage of the *k*-ω model is that the results are sensitive to the choice of boundary conditions and initial conditions.

4.2.5 Turbulent Model SST

Shear stress transport (SST) model described by Menter. This model is a hybrid turbulence model to get advantages *k*-ε and k-ω turbulent models. Figure 16 shows the Zonal work turbulence model *k*-ε & k-ω around the flat plate, the first model applies in the wake and outward stream domain. Other models work around the wall it means sub and log layer.

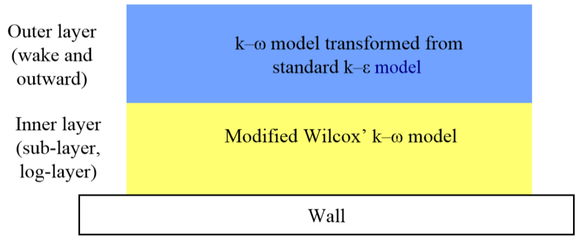

Figure 16. Zonal work turbulence model *k*-ε & *k*-ω on a flat plate [32]

According to a combination between k-ε and k-ω turbulence models, Transportation equation blended of them to obtain by

$$\frac{\partial(\rho k)}{\partial t}+\frac{\partial(\rho k\bar{U}_i)}{\partial x_i}=\frac{\partial}{\partial x_j}\left(\left(\mu+\frac{\mu_t}{\sigma k}\right)\frac{\partial k}{\partial x_j}\right)+\tau_{ij}\frac{\partial\bar{U}_i}{\partial x_j}-\beta^*\varepsilon\rho\omega$$

$$\frac{\partial\omega}{\partial t}+\frac{\partial}{\partial x_i}(\omega\bar{U}_i)=\frac{\gamma}{\nu_t}\tau_{ij}\frac{\partial\bar{U}_i}{\partial x_j}-\beta\rho\omega^2+\frac{\partial}{\partial x_j}\left(\left(\mu+\frac{\mu_t}{\sigma_\omega}\right)\frac{\partial\omega}{\partial x_j}\right)+2\rho(1-F_1)\sigma_{\omega 2}\frac{\partial\omega}{\partial x_j}\frac{\partial k}{\partial x_j}\frac{1}{\omega} \qquad (4.16)$$

The SST *k*-ω model has shown good performance for many types of complex flows, such as inflows with adverse pressure gradients and separating flows. It has been recognized for its good overall performance [33] and it is the most commonly used turbulence model for simulations of ship hydrodynamics. A drawback needs a lot of time to solve problems combers with the *k-ε* turbulence model.

4.3 Geometry of Planing Hull

The model employed in this study is the same as the one used in the Morabito experiment [34] whose model surface is shown in Figure 17. The model is a box shape whose dimensions are (length 914 mm, beam 183 mm, depth 102 mm) with groove (9 mm high × 6 mm deep) around the model. It is located at 9 mm above the bottom.

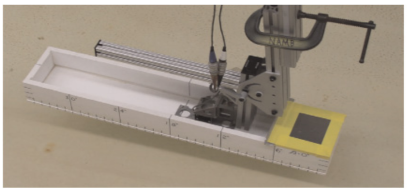

a) Experimental model (Morabito, 2013)

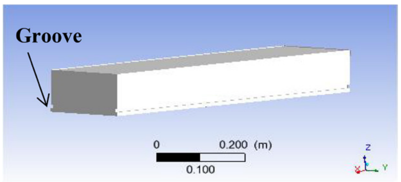

b) Numerical model

Figure 17. Planing hull model a) Experimental model (Morabito, 2013) b) Numerical model

The test was adopted by moving the model through the channel at a constant sinkage and trim by aft is equal to 6 degrees. This angle raises the bow of the hull above the waterline leads to canceling the bow effect. The hull model is examined in calm water at a range of speed from 0.3 m/s to 3.7 m/s for water depths 0.5b, 0.75b, 3b, 8b.

The objectives of the Morabito experiment are to measure the tangential force and normal force on the bottom of the hull separately using a dynamometer, also it's calculated; the change in wetted chain length (L_C), and transom ventilation (Y_K) at all range of speed. For that, the hull is divided into station and water line shown in a.

4.4 Planing Hull Computational Domain

Due to the symmetry of the hull, only half of the computational domain is represented in the CFD simulations of this study with dimensions shown in Figure 18. The hull is implemented with a fixed trim of 6 degrees and fixed heave giving a transom draft of 0.05673 m, such as that in the experimental work. The study is carried out to simulate a shallow channel whose water depth is 0.1 L and width is 1.3 L. The reference point of the computational domain is at G= (0, 0, 0). Boundary conditions imposed on the numerical domain are shown in Table 2. The air-water flows through the shallow channel from inlet to outlet about the hull. These investigations cover a range of speeds from 0.3 m/s to 3.7 m/s. This range includes the three regions of the subcritical, critical, and supercritical speeds. Also, when the analysis for deep water, the high seabed equal to 2.46 L. This height ensures no effect for seabed on the hull resistance.

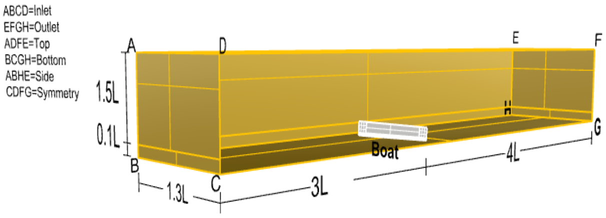

Figure 18. Dimension and boundary conditions of the shallow domain

Table 2. boundary conditions details

Position	type	boundary condition
Boat	No-slip	wall
Inlet	velocity	inlet
Outlet	static pressure	outlet
Top	free slip	wall
Side	free slip	wall
Bottom	free slip	wall
Symmetry	-	symmetry

In this investigation, was selected the *k-ε* turbulence model depending on previous work [12]. At the critical speeds, when the ship velocity is equal to the velocity of the wave in a shallow channel, the solitary wave will be established every some time. The solitary waveform is a wave single crest that moves forward through the shallow channel. Hence, it's required transient analysis at critical speed as shown in Table 3. The analysis at subcritical speeds and supercritical speeds are steady with time shown in Table 4.

Table 3. analysis setting at critical speeds

analysis type	transient
number of element	6000000
turbulent model	*k-ε*
Total time	25 sec
time step	0.2 sec

Table 4. analysis setting at subcritical and supercritical speeds

analysis type	Steady-state
number of element	6000000
Residual	e^-5
Max iteration	10000
turbulent model	*k-ε*

4.4.1 Open Water Domain Dimension

An open water analysis needs to make some changes

http://dx.doi.org/10.36956/sms.v3i1.414

in computational domain dimensions to cancel the seabed effect shown in Figure 19. When $h/T \geq 10$ the effect of seabed to the hull is insignificant. In literature reviews of planing hull analysis in deep water, the depth of water is equal to three times the total length of the vessel. Moreover, the distance between the channel side and the hull equals two and a half time the hull length. This distance more than enough to remove the effect of channel-side into the hull. The small box around a hull as a domain uses to help capture physics phenomena at deep-water analysis. A small domain dimension is shown in Figure 19.

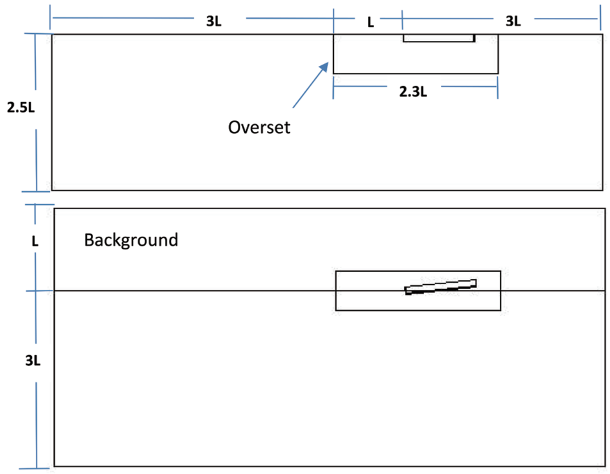

Figure 19. Open water domain dimension

4.4.2 Distribution on the Hull

In the current study, the wall bounding effects are very important and have a significant effect on the hull form drag at different speeds. Figure 20 shows the distribution y+ on the hull which a value around 30 to 300. This range of y+ gives the turbulence model a good chance to predict the flow around the hull form properly. Can be calculated.

$$y^+ = \frac{yu^*}{v} \tag{4.17}$$

u* Calculated by flowing formula

$$u^* = \sqrt{\frac{t_w}{\rho}} \tag{4.18}$$

And

$$t_w = \frac{1}{2}\,\rho\, C_f U^2 \tag{4.19}$$

The distance from the surface of the hull to the first cell centroid considered it y, u* wall friction velocity, v kinematic viscosity, t_w sheer stress, ρ dynamic viscosity, U speed of the vessel, C_f friction coefficient obtained by equation (4.3).

4.4.3 Free Water Surface

To simulate a hull moving in water, models are needed to resolve the interface between the water and air. There are different two-phase models available that either tracks the surface directly or tracks the different phases and then reconstruct the interface. One example is the level-set method, where all molecules of one phase are marked and then tracked in the fluid flow. The most frequently used

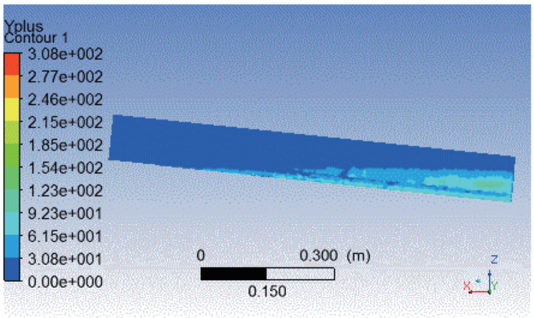

a) hull side in shallow water

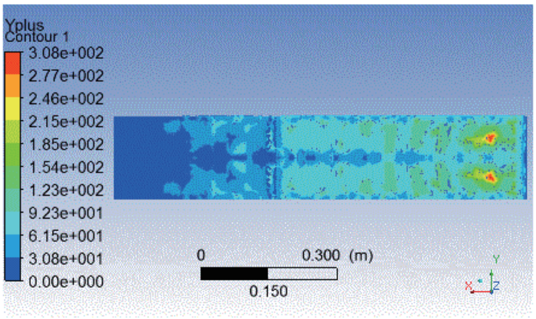

b) hull bottom in shallow water

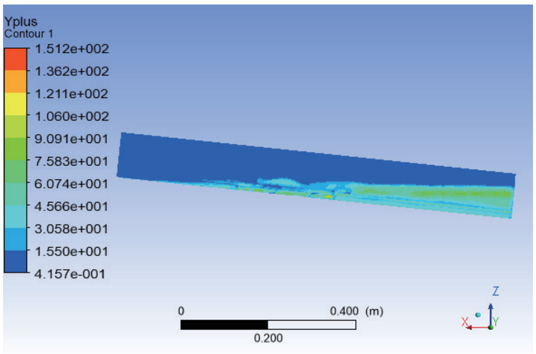

a) hull side in open water

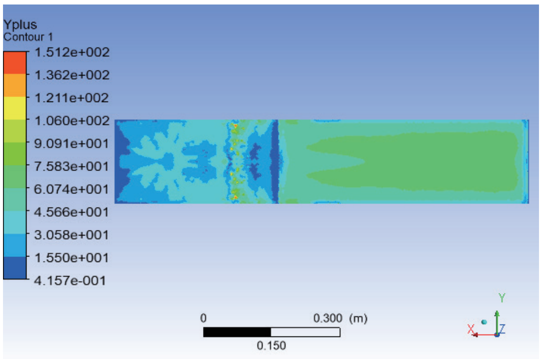

b) hull bottom in open water

Figure 20. distribution y+ on the hull

http://dx.doi.org/10.36956/sms.v3i1.414

method to capture the free surface in ship hydrodynamics is the volume of fluid (VOF) method. In the VOF method, the different phases are tracked.

The flow of the model is assumed to be an incompressible turbulent flow. Hence, the governing equations are the continuity and momentum equations given as follows.

$$\frac{\partial u}{\partial x}+\frac{\partial v}{\partial y}+\frac{\partial w}{\partial z}=0$$

$$\frac{\partial \overline{U_i}}{\partial t}+\overline{U_j}\frac{\partial \overline{U_i}}{\partial x_j}=-\frac{1}{\rho}\frac{\partial \overline{P}}{\partial x_i}+\nu\frac{\partial^2\overline{U_i}}{\partial x_j\partial x_j}-\frac{\partial \overline{u_i u_j}}{\partial x_j}+g_i \quad (4.20)$$

The Reynolds stress tensor $\overline{u_i u_j}$ represents the change of momentum cross the free-surface which occurs as a result of surface tension force, the color function describes the free-surface as the volume of fraction γ

$$\frac{\partial \gamma}{\partial t}+U_i\frac{\partial \gamma}{\partial x_i}=0 \quad (4.21)$$

Based on the volume of fluid (VOF) method, the air-water interface is described implicitly. The volume of fraction γ represents the percentage of water at each cell at the free surface to describe the interference between the two fluids. The magnitude of γ for each cell cut by the free surface is between 0 and 1 ($0 < \gamma < 1$). While the volume fraction γ equals 1 for total water occupancy, it equals 0 for total air

$$\rho_{ij}=\gamma_{ij}\rho_w+(1-\gamma_{ij})\rho_a \quad (4.22)$$

$$\mu_{ij}=\gamma_{ij}\mu_w+(1-\gamma_{ij})\mu_a \quad (4.23)$$

Where ρ and μ at any cell (denoted by *ij*) can be computed using γ by taking a simple volume average over the cell. Besides, (*a*) and (*w*) refer to air and water, respectively.

4.5 Mesh Generation Strategy

Code ICEM CFD is used to generate an unstructured mesh grid required for the CFD code solver.

For analysis in two waterways, it needs different strategies for building mesh in the computational domain. In shallow channel analysis is applied grid in one-domain is called single mesh, whereas a two-domain grid is used in open water analysis it is called overset mesh.

4.5.1 Single Mesh

The number of mesh elements generated –in one domain- and shown in Figure 21 equals 6 million elements. The accuracy of results is dependent on the quality of the mesh grid which is affected by the element size, type, and algorithm. The number of mesh elements is increased over the planing hull surface and its vicinity to improve the accuracy of numerical predictions of resistance and wave patterns generated at different forward speeds. The mesh density function is applied at the free-surface region throughout the whole computational domain to better predict the generated wave patterns by the hull. A refined mesh is generated at the bottom of the computational domain to accurately predict the effect of the channel bottom on the hull resistance.

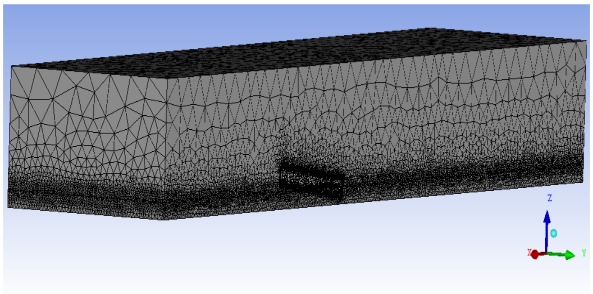

a) Tetrahedral mesh all over the domain

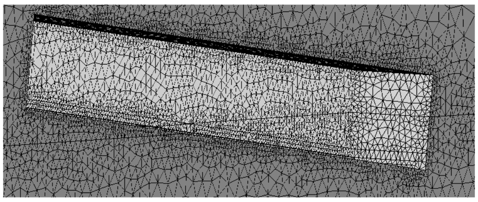

b)Mesh size around the hull

Figure 21. Schematic illustration of generated 6 million mesh elements in one-domain. A) Tetrahedral mesh all over the domain b) Mesh size around the hull.

4.5.2 Overset Mesh

The overset mesh creation is a bit more challenging than the one of the single mesh since it requires the creation of two computational domains: the background and the overlapping domain. The first one consists of a box of large dimensions, while the second one is smaller and contains the boat shown in Figure 19. The idea underlying the overset technique is that the increasing number of elements mesh around the hull without increase the total number of elements in the background domain. On the other hand, the drawback lays in the fact that there has to be communication between the two domains, through an interpolation across the domain boundaries of the smaller domain. To limit the effect of the interpolation to the minimum the meshes have to be built so that the size of the cells at the boundary of the overlapping domain is as close as possible to one of the background domains in that area. Once the domains are created, the same refinements presented for the single mesh are applied, with the only difference that some refinements will belong to the overset domain and some to the background. The free surface refinement will belong to both: an internal surface needs to be created in both domains. The wake refinement will be present only in the background domain, while the surface, curve, and undersea refinements will be added in the overset one. Another refinement is added in the background domain, to comply with the requirement of the same cell size in the area around the boundaries of the overset domain. This is done by inserting in the background domain a box refinement around the overset domain with a target cell size of 0.04 m. Figure 22 shows tetrahedral mesh around the two domains and presium layer around the hull.

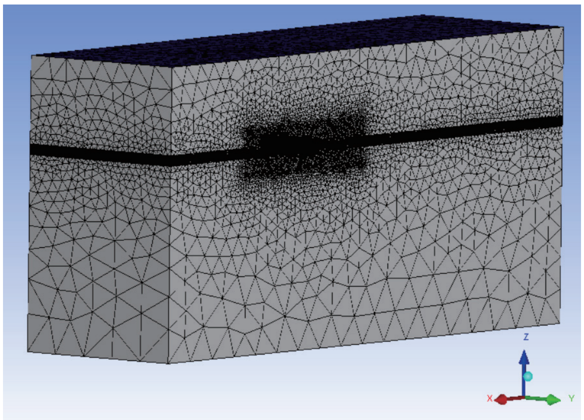

a) Tetrahedral mesh all over the domain

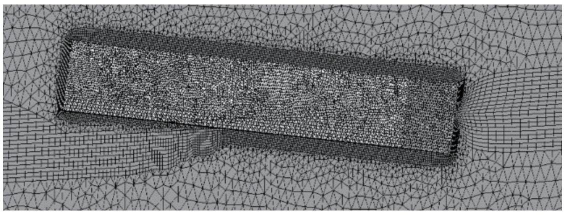

b) Presium layer around the hull

Figure 22. overset mesh generation 1.6 million mesh element

4.6 Mesh Dependence Study

The one-domain mesh generation gives a tremendous number of elements when the change element size. To improve the results a grid dependence study has been made for three generations of mesh 3, 6, and 9 million elements. The grid which has 6 million elements give the best results for all range of speeds and suitable time of analysis. Table 5 shows the error of numerical results for three mesh element comber with experimental resistance and lift force. The minimum error can be founded for the last speed in the range of critical speed 1.2 m/s achieved by 6 million elements.

4.7 Solution

When achieved convergence criteria for total resistance and lift force, the analysis was completed to solve the problem. Figure 30 explains the value of total resistance, lift force, and trim moment in the critical speeds range.

4.8 Post-processing

After the analysis was finished, the post-processing tool was utilized to describe the contour in the waterline, dynamic pressure contour on the hull, and the relation between time and resistance or force or trim moment.

5. Results and Discussion

This study predicted total resistance, generated wave pattern and, lift force of a planing hull model moving in a shallow channel over three regions of speed, (subcritical, critical, and supercritical). Numerical results were validated by comparison with experimental data available in the literature [14].

5.1 Comparison of Numerical and Experimental Results

This part of the thesis compares to available experimental results; wetted length, dynamic normal force over displacement, and lift force coefficient with the numerical results. Notice that, at the critical speed range the value of results fluctuates. For that, the mean value was obtained numerically and compared with the mean value experimentally. The mean value of results can be calculated as

$$Xm = \frac{\sum_{k=1}^{k=n} x_k}{n} \tag{5.1}$$

Where

X_m = mean result at a critical speed

n = number of results

X_k = results at a critical speed.

Furthermore, the percentage of error calculated from this equation:

$$error = \left|\frac{V_{ex}-V_{nu}}{V_{ex}}\right| * 100\% \tag{5.2}$$

Where

V_{ex} = experimental value

V_{nu} = numerical value

Table 5. mesh dependence study for speed 1.2 m/s

Force on hull (N)	Experimental (N)	3 Million Elements	Error (%)	6 Million Elements	Error (%)	9 Million Elements	Error (%)
Total Resistance	4.80	6.64	38	6.08	27	6.33	32
Lift Force	41.75	58.98	41	56.03	34	58.00	39

5.1.1 Comparison SST & k-ε Turbulence Model

The results of the total resistance are calculated from two turbulences mode SST & *k-ε*. The SST model spends more time to arrive at the result comber with the k-ε model. Because the SST model solves two transport equations. Table 6 shows comparison between two errors of total resistance when using SST & *k-ε* model. In the SST turbulence model, the error of resistance is near to 1% in middle high speeds. Whereas in last high speed the error of the k-ε model lower than an error of the SST model. After that, the error of an SST and k-ε model are Convergent in all ranges of speed. In this investigation was selected the *k-ε* turbulence model for all range of speeds.

Table 6. comparison total resistance using turbulent mode SST and k-ε

Velocity (m/s)	$R_{T,Exp}$ (N)	R_T (*k-ε*) (N)	R_T (SST) (N)	(*k-ε*) Error 100%	(*SST*) Error 100%
0.3	0.309	0.307	0.307	0.555	0.606
0.5	0.670	0.789	0.798	17.792	19.041
0.6	1.215	1.123	1.202	7.506	1.050
0.8	2.513	2.755	2.755	9.642	9.642
0.9	3.736	3.582	3.473	4.134	7.058
1	4.416	4.294	4.227	2.759	4.284
1.1	4.946	5.351	5.298	8.189	7.119
1.2	4.801	6.080	6.011	26.628	25.201
1.3	4.787	4.905	4.793	2.458	0.115
1.4	4.856	5.049	4.904	3.983	0.993
1.5	5.007	5.214	5.051	4.137	0.882
1.8	5.814	5.792	5.588	0.374	3.879
2.4	7.737	7.255	6.958	6.225	10.066
3	9.771	9.029	8.660	7.596	11.371
3.7	12.379	11.645	11.172	5.928	9.753

5.1.2 Wetted Length Lc

The wetted length expresses the chine length under the waterline

Figure 23 shows the comparison between the wetted length to beam ratio of the model versus Froude depth numerically and experimentally. When the Froude depth near 1, the wetted length increases, as a result of solitary wave formation at the critical speeds range. However, all the ranges of numerical results achieved an error of around 4.8 % compared with experimental results. The maximum error at F_h= 1.27 is equal to 31.3 %. Approximately, at the supercritical speeds range, the wetted length is steady at 3.45 while, at subcritical speeds, it's slightly fluctuated around 3.25. In general, the numerical results of Lc/b showed an excellent agreement with the results of the experiment.

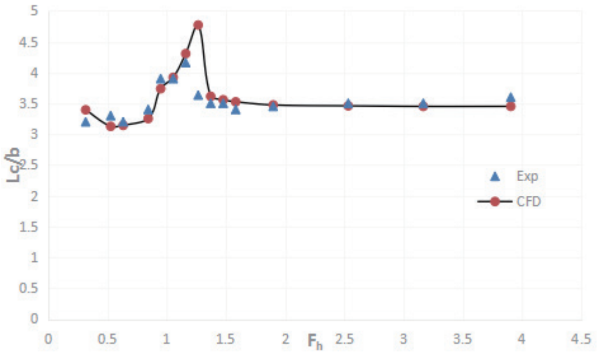

Figure 23. Comparison between experimental and CFD results of wetted length/beam ratio at different Froude depth

5.1.3 Normal Force (N)

The normal force means the hydrodynamic force acts perpendicularly to the hull bottom. Figure 24 shows the dynamic normal force to static buoyancy force ratio, versus the Froude beam (C_V) numerically and experimentally. The experimental normal force ratio slightly decreases below zero at the low-speed range before full ventilation at the transom occurs, which means the dynamic force applies suction on the hull toward the channel bed (squat force). The numerical normal force slightly decreases at partial ventilation. Then it increases rapidly until the dynamic force equal to displacement force at full ventilation at transom as a result of hydrodynamic lift. At this range the largest deviation between experimental and numerical results occurs. After that, the curve increases sharply without a considerable deviation between numerical and experimental results. The numerical results are lined with experimental results.

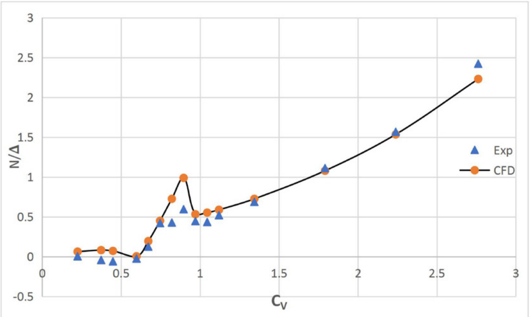

Figure 24. dynamic normal force/static normal force ratio N/Δ versus C_v numerically and experimentally

5.1.4 Total Resistance RT

A comparison between the numerical total resistance and experimental total resistance is shown in Figure 25. The two curves increase sharply over the critical Froude number's range (Fh=0.84 to Fh=1.27). After that, there is a slight drop in values and then they increase gradually over the supercritical Froude number's range (Fh=1.37 to Fh=3.9). Very good agreement between the two curves is observed over –almost- the whole range of Froude numbers albeit, the error increases at Froude number close to the peak. The total average error between the numerical and experimental total resistance is no more than 8%. The maximum error is observed at the maximum critical Froude-depth number of 1.27 and is equal to 26%.

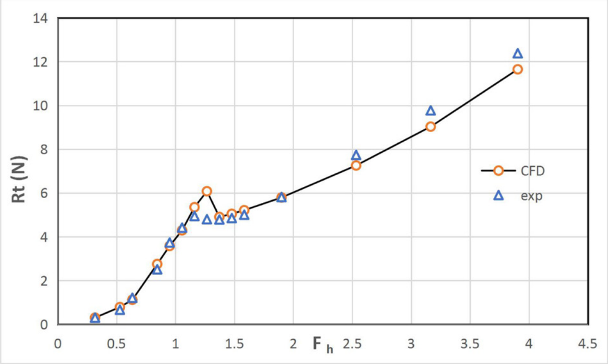

Figure 25. Experimental and numerical total resistance

5.1.5 Hydrodynamic Lift Force LF

A comparison between the numerical and experimental total lift force is shown in Figure 26. In general, the lift force decreases slightly over the supercritical range (from F_h=0.32 to F_h=0.63). There is a numerical over prediction of the lift force in this range. However, the lift force increases rapidly over the critical speed range (from F_h=0.84 to F_h=1.27). Subsequently, the value of the lift force rises gradually over the supercritical range. The total average error equals 7%, while the maximum error is 34% at the maximum critical Froude-depth number. For the whole range of speeds, very good agreement is observed between the numerical and experimental lift force except the maximum critical speed of 1.2 m/s.

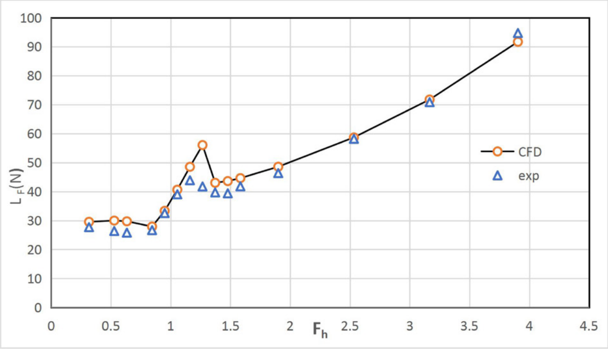

Figure 26. Experimental and numerical Lift force

5.1.6 Wave Pattern

The numerical and experimental wave pattern is similar at speed 0.3 m/s as shown in Figure 27. The free surface deformation at the displacement speed of 0.3m/s is not significant. In the low-speed region, there is no high deformation at the hull side, the wetted chine experimentally and numerically equal to 558.8 mm and 620.9 mm sequentially. Also, there is partial ventilation at transom equals 2.12 mm experimentally and 3.23 mm numerically.

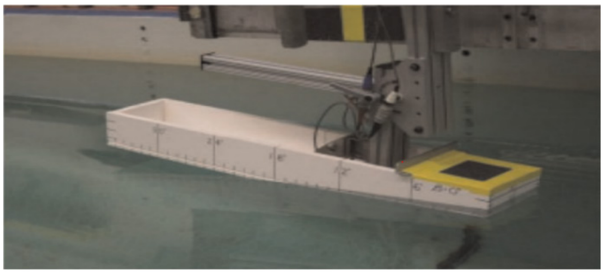

a) Experimental Wave pattern [34]

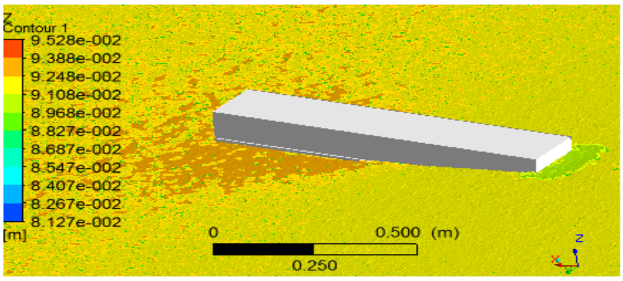

b) Numerical wave pattern

Figure 27. Wave pattern comparison at speed of 0.3 m/s

Figure 28 shows a similarity in the generated wave pattern numerically and experimentally at a speed of 1.8 m/s. There is a high deformation on the free surface at the planing speed of 1.8 m/s. While the waves about the hull side increase in height leading to an increase in wetted chine equal to 635.42 mm numerically and 609.6 mm experimentally, further the free surface drops at the transom. For the numerical and experimental generated wave pattern, high deformation occurs on the free surface and full ventilation at transom equal to 56.73 mm experimentally and 59.03 mm numerically.

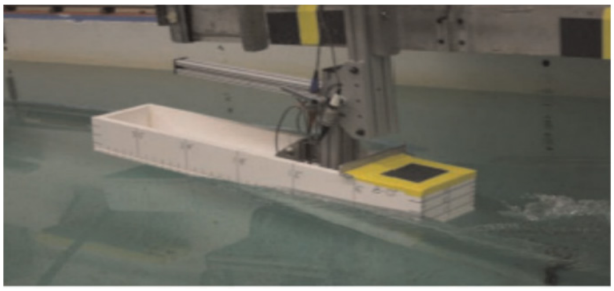

a) Experimental wave pattern [34]

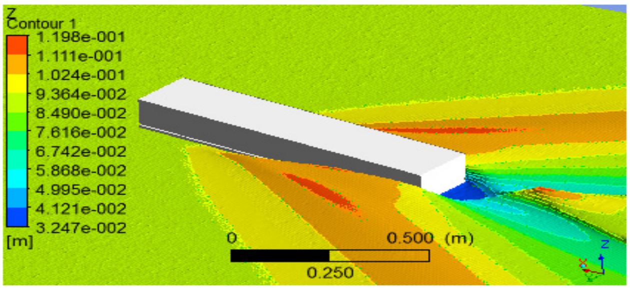

b) Numerical wave pattern

Figure 28. Wave pattern comparison at speed 1.8 m/s

5.2 Solitary Wave Formation and Effects

In this section, the complex hydrodynamic phenomena of solitary wave or soliton formation will be discussed. The solitary wave requires a specific situation to occur such as a shallow channel waterway. When a hull is moving at critical speed in a shallow channel, the solitary wave will be observed. Table 7 shows the solitary waves establishment positions, and amplitudes for critical speeds which are 0.8, 0.9, 1, 1.1, 1.2 m/s. The amplitude of the solitary wave increases with the increase in wave speed. At speed 1.2 m/s, the generated solitary wave is at amidships which has the highest amplitude of 0.05960 m. The solitary wave shifts forward till positioned at the front of the hull, which leads to fluid flow about the hull to be more complex.

Table 7. properties the solitary wave at a range of critical speed

Critical speed m/s	**location of the wave formation numerically**	**Maximum wave amplitude (m)**	**location of the wave formation experimentally**
0.60	No wave	-	No wave
0.80	3.3m ahead of model	0.0133	3 m ahead of model
0.90	1.2m ahead of model	0.0263	1 m ahead of model
1.00	0.3m ahead of model	0.035	at Bow
1.10	at Bow	0.0414	at Amidships
1.20	at Amidships	0.0596	supercritical swept 10-deg

The solitary wave establishes itself at different locations along the hull within the range of critical speeds and moves forward on the hull with time. Figure 29 shows the solitary wave formation steps. Firstly, the divergent waves hit the channel side at t = 2.4 seconds and increase the pressure on the channel sidewall. Secondly, the waves are reflected from the channel side and encounter other divergent waves generated from the hull after 4 seconds. Thirdly, the solitary wave becomes Perpendicular to the hull at t = 10 seconds. Afterward, the wave shifts forward at t = 14.2 seconds until the maximum amplitude formulates at a position of 0.3m after the hull. The next pulse of the wave is produced at t = 18 seconds. As the hull moves in a shallow channel, it produces a pulse wave repeated every 23 seconds.

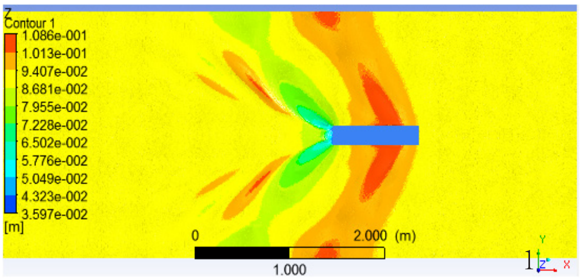

t=2.4sec

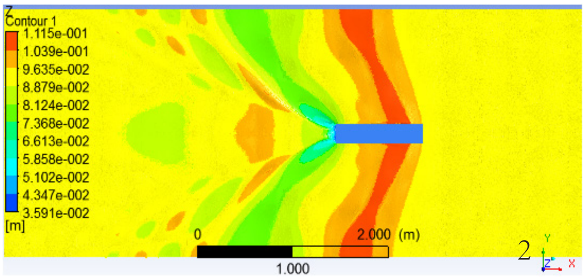

t=4sec

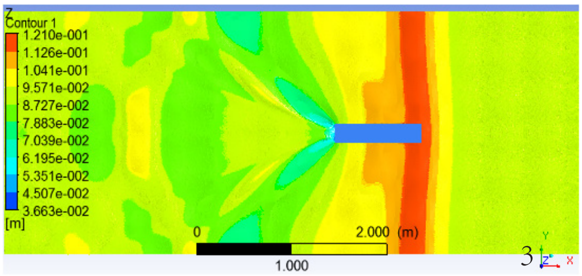

t=10sec

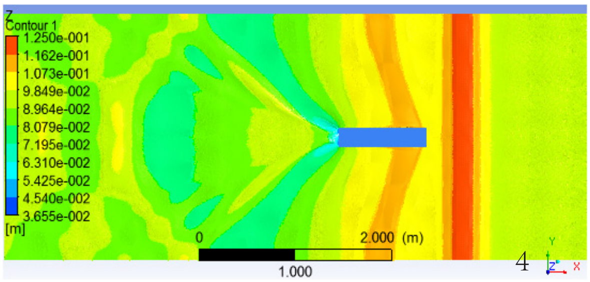

t=14.2sec

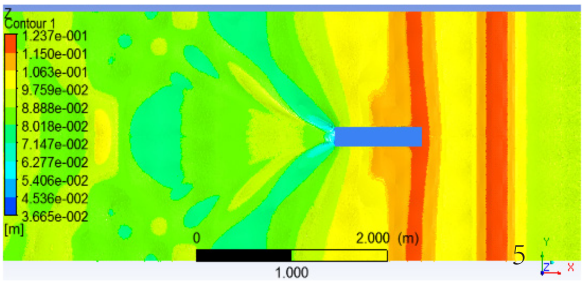

t=18sec

http://dx.doi.org/10.36956/sms.v3i1.414

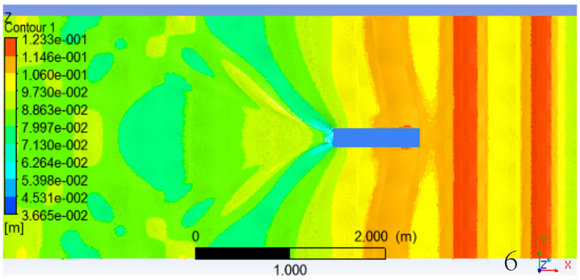

t=23sec

Figure 29. Solitary wave formulation steps at speed 1m/s

Figure 30 represents the change in a trim moment, lift force, and total resistance on a half planing hull at the critical speed versus time. The maximum trim moment and maximum lift force occur on the hull at the same time. The effect of a solitary wave on the moment and lift force curves is like a sinusoidal wave. The instantaneous values of the trim moment and lift force relate to the location of the solitary waveform and speed. The direction of a total resistance an opposite to inlet flow.

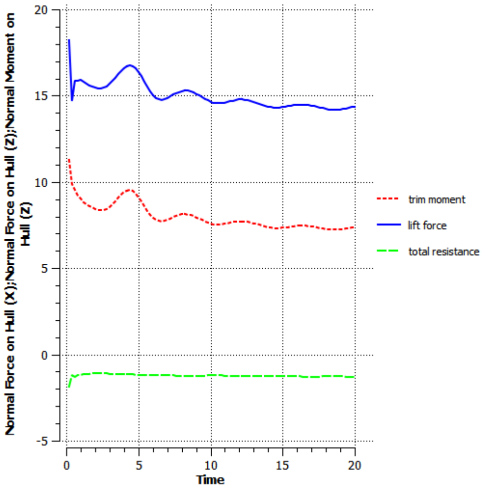

Speed 0.8 m/s

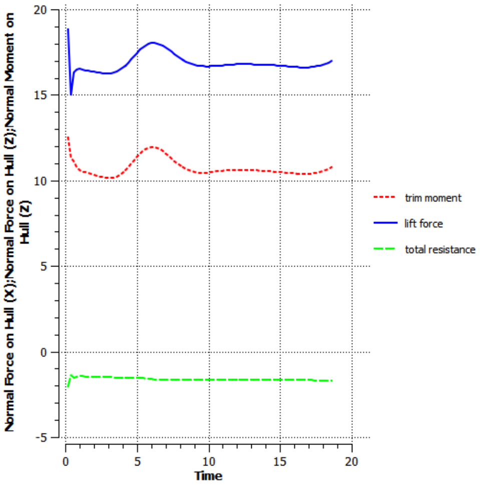

Speed 0.9 m/s

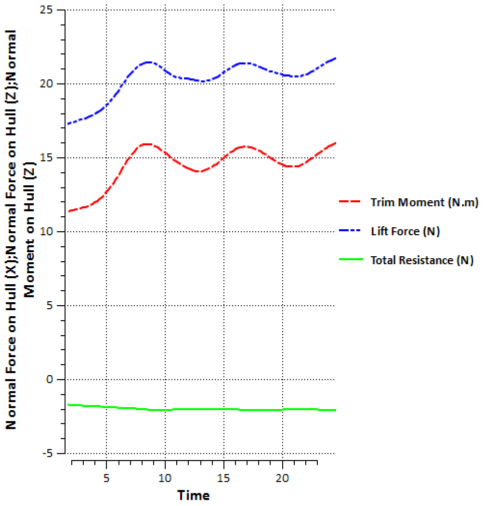

speed 1 m / s

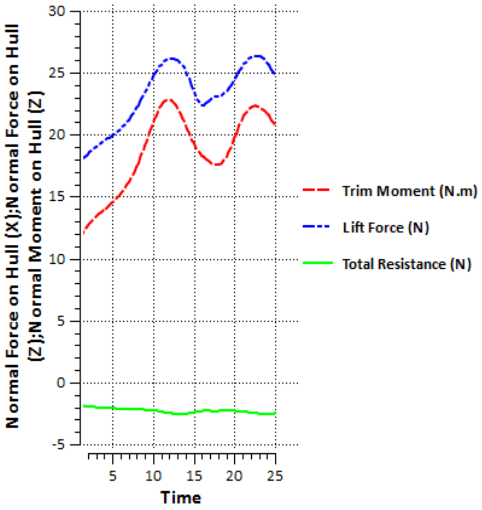

Speed 1.1m/s

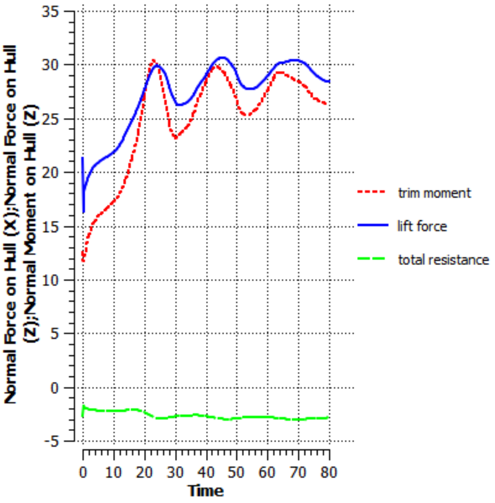

Speed 1.2 m/s

Figure 30. Solitary wave effects on a trim moment, lift force, and total resistance

5.3 Comparison between Hydrodynamic Performance in Shallow Water Channel and Open Water

In this section of a results comber, the dynamic pressures distribution on the hull, wave patter at critical speed, and total resistance change between shallow water channel and open water.

5.3.1 Dynamic Pressure Distribution on the Hull

Figure 31 shows the difference between the shallow channel and deep water hydrodynamic pressure around the hull at a critical speed.

Figure 31 (b) and (d) show an increased wetted surface area on the hull side and hull bottom in a shallow channel at critical speed compared with the wetted surface area in open water that is shown in Figure 31 (a) and (c). The maximum hydrodynamic pressure in Figure 31 (b) and (d) at hull piercing on the water. It's higher than that on the hull in (a) and (c). The pressure distributions around the hull at critical speed are unstable with time as a result of solitary wave formation.

5.3.2 Wave Pattern at Critical Speed

Figure 32 (a) and (b) show the wave elevation comparison between open water and shallow water channel at speed (1 m/s). The maximum wave height at the shallow water channel equals 0.069 m. On the other hand, the maximum wave height at deep water equals 0.038 m. The elevation of the wave in the shallow channel increases by about 81% from deep water. In shallow channels (Figure 32 (b)), the wave elevation increases, and the solitary wave occurs at a critical speed surface which leads to an increase in the wave-making resistance compared with open water.

5.3.3 Total Resistance (RT)

Figure 33 explains the total resistance in deep water for three regions of speed. When the Froude number is in the range of 0.5 this called displacement mode, and the total resistance increases with speed. For semi-displacement speed, the hump of resistance occurs at 0.5< Fr< 0.85 as a result of superposition in the wave system. After that, the total resistance increases with speed at the planing range Fr>0.85. This general figure for the total resistance of the planing hull in deep water is similar to the deep water carve in Figure 34, which shows the total resistance in shallow water channels compared with the total resistance in deep water. The total resistance in deep water at low speeds is not exactly similar to the total resistance in the shallow channel. Firstly, in the deep water, the chart increases gradually until the appearance of the hump which increases resistance as a result of a superposition between two crests or two troughs in the wave system.

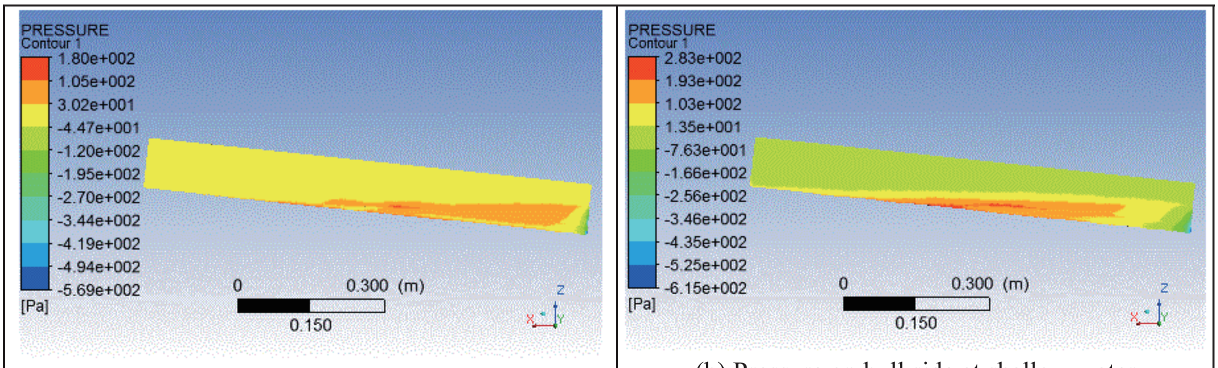

a) Pressure on hull side at deep water

(b) Pressure on hull side at shallow water

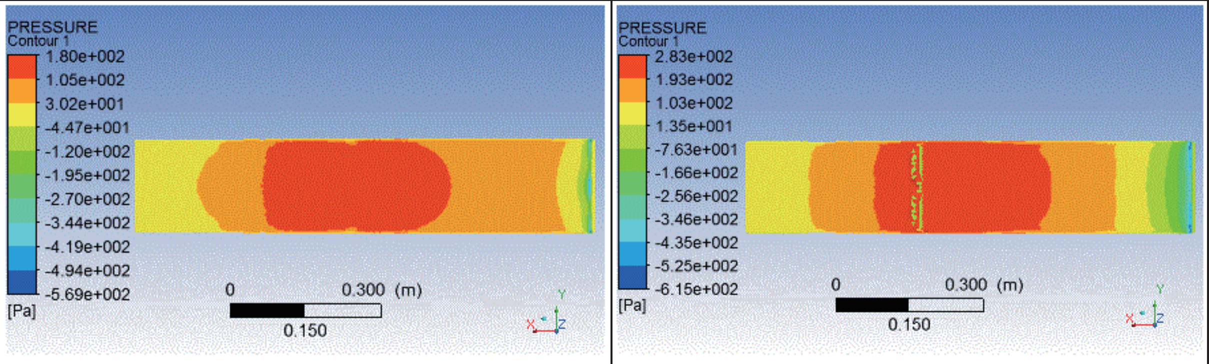

(C) Pressure on hull Bottom at deep water

(d) Pressure on hull Bottom at shallow water

Figure 31. Hydrodynamic pressure around the hull

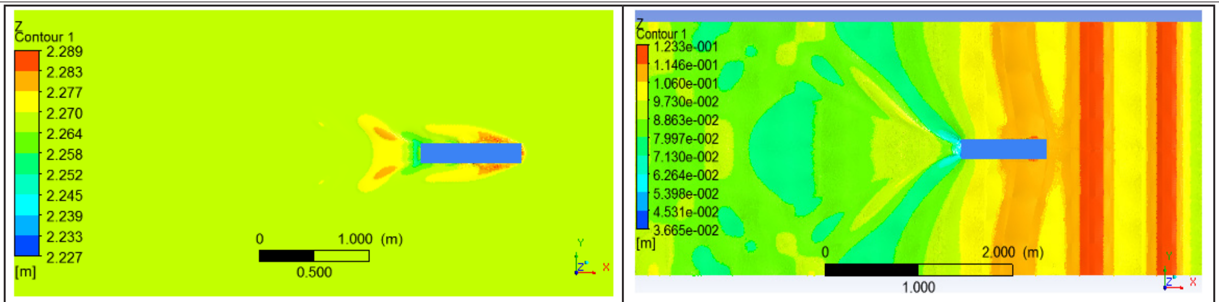

(a) Wave elevation in a deep water

(b) Wave elevation in a shallow water

Figure 32. wave systems comparison between a shallow channel and open water at speed 1m/s

Also, there is a hollow that causes the total resistance to decrease because the crest cancels the trough in the wave system. Secondly, the total resistance in shallow water is rising rapidly in the critical speed period (0.8---1.2 m/s). The maximum difference between total resistance in shallow water and total resistance in deep water is equal to 43% at speed 0.9 m/s. The total resistance in the supercritical speed range increases dramatically with speed increase. Lastly, the total resistance in the shallow channel is much higher than the total resistance in open water.

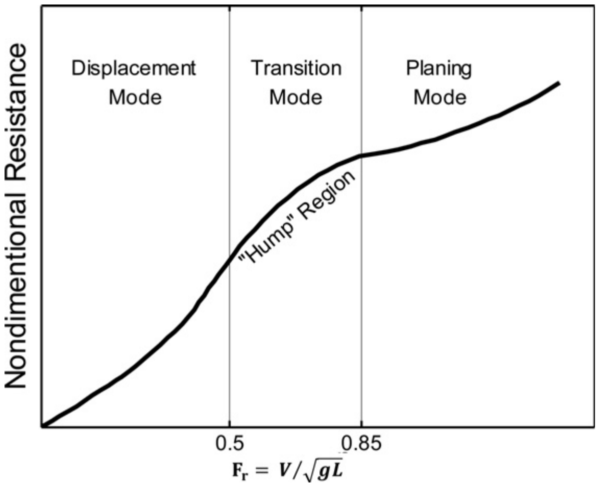

Figure 33. Total resistance of planing hull in deep water [35]

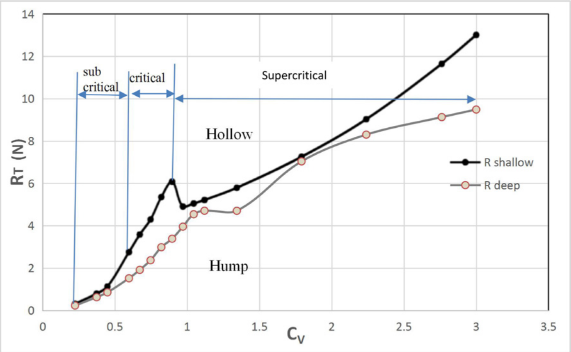

Figure 34. Comparison between the total resistance in shallow water channel and the total resistance in deep water

6. Conclusions and Recommendations

In this chapter, the conclusion, and recommendation of the results from the numerical simulations of the prismatic planning hull when moving in various waterways, is presented.

6.1 Conclusions

In this thesis, the RANS equations are solved by ANSYS-CFX code to simulate a small high-speed hull form moving in a shallow channel and open water. The total resistance and wave pattern of the planing hull model at three regions of speed (subcritical, critical, and supercritical) moving in the shallow channel have been numerically simulated.

- In the shallow water channel, the total average error equals 7% for numerical lift force, 8% for numerical total resistance compared with available experimental results. The numerical analysis well captured the wave pattern. The numerical results give good agreement over the whole range of speeds with the experimental results except at the maximum critical speed of 1.2 m/s which resulted in an error equal to 34% for lift force and 26% for total resistance.
- In the current study, the steps of the solitary wave formulation have been described at critical speeds. The amplitudes of the solitary waves were determined at the critical speeds of 0.8, 0.9, 1, 1.1, and 1.2 m/s where the amplitudes were found equal to 0.0133, 0.0263, 0.035, 0.0414, and 0.0596 m respectively.
- The amplitude of the solitary wave increases whenever there is an increase in the critical speeds. Also, this investigation defined the locations of the solitary wave formulation. Solitary wave formulates in front of the hull at the lower range of critical speed. However, at the higher range of critical speed, it formulates on the hull.
- The solitary wave formation increases the wetted surface area and the free surface deformation. Also, causes fluctuation in the trim moment, and lift force on the planing hull depends on the location and amplitude of the solitary wave. The total resistance on the hull in the

shallow channel is higher than the total resistance in open water. The maximum difference is 43% which takes place at a critical speed of 0.9 m/s.

In conclusion, the worst effect on the planing hull in shallow channels occurs at the critical speed range, where solitary wave formulates. So boat drivers must avoid sailing at a critical speed range.

6.2 Recommendations

The future working which can be recommended:

- Further study for critical speed ranges and behavior of hull motion especially the last speed in the range.
- Using various mesh strategies and different software for this investigation to do more verification of results.
- Additional research concerns the effect of channel dimensions and vessel shape on the formation of a solitary wave at a critical speed.
- Research on how to apply solitary wave energy in useful engineering applications.

References

[1] G. For et al., "GUIDELINES FOR WING-IN-GROUND CRAFT," Int. Marit. Orgnization, vol. 44, 2018.

[2] R. Yousefi, R. Shafaghat, and M. Shakeri, "Hydrodynamic analysis techniques for high-speed planing hulls," Appl. Ocean Res., vol. 42, pp. 105–113, Aug. 2013.
DOI: 10.1016/j.apor.2013.05.004.

[3] V. Kerman, "The Impact on Seaplane Floats During Landing," Washington, No 321, 1929.

[4] T. B.R, Savander, S.M, Scorpio, R.K, "Steady Hydrodynamic Analysis of Planing Surfaces," J. Sh. Res., vol. 46, pp. 248–279, 2002.

[5] S. D. S. Xue-Nong Chen, "A Slender Ship Moving at a Near-Critical Speed in a Shallow Channel," J. Fluid Mech., vol. 291, no. May 1995, pp. 263–285, 1995.
DOI: 10.1017/S0022112095002692.

[6] K. W. Christopher, "Effect of Shallow Water on the Hydrodynamic Characteristics of a Flat-Bottom Planing Surface." NACA, Washington, 1956, [Online]. Available: http://www.dtic.mil/cgi-bin/GetTRDoc?Location=U2&doc=GetTRDoc.pdf&AD=ADA377307.

[7] C. J. Reyling, "An experimental study of planing surfaces operating in shallow water," new jersey, 1976.

[8] A. Iafrati and R. Broglia, "Comparison between 2D+t potential flow models and 3d rans for planing hull hydrodynamics," Ital. Sh. Model Basin, no. December 2016, pp. 6–9, 1955.

[9] F. Di Caterino, R. Niazmand Bilandi, S. Mancini, A. Dashtimanesh, and M. DE CARLINI, "A numerical way for a stepped planing hull design and optimization," NAV Int. Conf. Sh. Shipp. Res., no. 221499, pp. 220–229, 2018.
DOI: 10.3233/978-1-61499-870-9-220.

[10] R. N. Bilandi, S. Mancini, L. Vitiello, S. Miranda, and M. De Carlini, "A validation of symmetric 2D + T model based on single-stepped planing hull towing tank tests," J. Mar. Sci. Eng., vol. 6, no. 4, 2018.
DOI: 10.3390/jmse6040136.

[11] S. Brizzolara and F. Serra, "Accuracy of CFD codes in the prediction of planing surfaces hydrodyamic characteristics," 2nd Int. Conf. Mar. Res. Transp., pp. 147–158, 2007, [Online]. Available: http://www.icmrt07.unina.it/Proceedings/Papers/B/14.pdf.

[12] A. S. Amir H. Nikseresht, "Numerical investigation of shallow water resistance of a planing vessel," Int. J. Civ. Struct. Eng., vol. 3, no. 1, pp. 164–168, 2016.
DOI: 10.15224/978-1-63248-083-5-62.

[13] S. Mancini, F. De Luca, and A. Ramolini, "Towards CFD guidelines for planing hull simulations based on the Naples Systematic Series," 7th Int. Conf. Comput. Methods Mar. Eng. Mar. 2017, vol. 2017-May, no. May, pp. 0–15, 2017.

[14] Y. Wang, "Numerical Prediction of Resistance of Planning Vessel with RANS Method," Int. Conf. Comput. Sci. Autom. Eng., no. Iccsae 2015, pp. 287–293, 2016.
DOI: 10.2991/iccsae-15.2016.55.

[15] A. De Marco, S. Mancini, S. Miranda, R. Scognamiglio, and L. Vitiello, "Experimental and numerical hydrodynamic analysis of a stepped planing hull," Appl. Ocean Res., vol. 64, pp. 135–154, 2017.
DOI: 10.1016/j.apor.2017.02.004.

[16] M. Bakhtiari, S. Veysi, and H. Ghassemi, "Numerical Modeling of the Stepped Planing Hull in Calm Water," Int. J. Eng., vol. 29, no. 2, 2016.
DOI: 10.5829/idosi.ije.2016.29.02b.13.

[17] A. Dashtimanesh, A. Esfandiari, and S. Mancini, "Performance prediction of two-stepped planing hulls using morphing mesh approach," J. Sh. Prod. Des., vol. 34, no. 3, pp. 236–248, 2018.
DOI: 10.5957/JSPD.160046.

[18] F. Roshan, A. Dashtimanesh, and R. N. Bilandi, "Hydrodynamic charactrisrics of tunneled planing hull in calm water," Brodogradnja, vol. 71, no. 1, pp. 19–38, 2020.

[19] A. Tafuni, I. Sahin, and M. Hyman, "Numerical investigation of wave elevation and bottom pressure generated by a planing hull in finite-depth water," Appl. Ocean Res., vol. 58, pp. 281–291, 2016.
DOI: 10.1016/j.apor.2016.04.002.

[20] D. Savitsky, "Hydrodynamic Design of Planing Hulls," Mar. Technol., vol. Vol. 1, no. No. 1, p. PP. 71-95, 1964.

[21] K. Potgieter, "Planing Hulls." South Africa, pp. 1–5,

2018.

[22] G. Fridsma, “A Systematic Study of the Rough-Water Performance of Planing Boats,” 1969. [Online]. Available: http://oai.dtic.mil/oai/oai?verb=getRecord&metadataPrefix=html&identifier=AD0708694.

[23] F. De Luca and C. Pensa, “The Naples warped hard chine hulls systematic series,” Ocean Eng., vol. 139, no. March, pp. 205–236, 2017.
DOI: 10.1016/j.oceaneng.2017.04.038.

[24] F. M. White, Fluid mechanics, 7th ed. Boston: (Mcgraw-Hill series, 2003.

[25] M. Rabaud and F. Moisy, “Ship wakes: Kelvin or mach angle?,” Phys. Rev. Lett., vol. 110, no. 21, 2013.
DOI: 10.1103/PhysRevLett.110.214503.

[26] J. N. Newman, Marine Hydrodynamics, 40th ed. Cambridge: MIT press, 1977.

[27] D. Frisk and L. Tegehall, “Prediction of High-Speed Planing Hull Resistance and Running Attitude. A Numerical Study Using Computational Fluid Dynamics,” CHALMERS UNIVERSITY OF TECHNOLOGY, Gothenburg, Sweden, 2015.

[28] W. M. H K Versteeg, An introduction to computational fluid mechanics., 2nd ed., vol. M. Perason Prentic Hall, 2007.

[29] B. Andersson, R. Andersson, L. Håkansson, M. Mortensen, R. Sudiyo, and B. van Wachem, Computational Fluid Dynamics for Engineers. Cambridge University Press, 2011.

[30] L. Davidson, An Introduction to Turbulence Models. Gothenburg: Chalmers university of technology, 2018.

[31] D. C. Wilcox, Turbulence Modeling for CFD, Third edit. La Canada, California: DCW Industries, Inc, 2006.

[32] I. F. Training, “Modeling Turbulent Flows [REVISIT],” 2006, [Online]. Available: http://www.southampton.ac.uk/~nwb/lectures/GoodPracticeCFD/Articles/Turbulence_Notes_Fluent-v6.3.06.pdf.

[33] T. Bardina, J., Huang, P., Coakley, “Turbulence Modeling Validation , Testing , and Development,” California, 1997.

[34] M. G. Morabito, “Planing in Shallow Water at Critical Speed,” J. Sh. Res., vol. 57, no. 2, pp. 98–111, 2013, doi: 10.5957/josr.57.2.120031.

[35] Marshall R, "All about Powerboats: Understanding design and performance," McGraw-Hill Professional, 2002.

Nomenclature

Latin Symbols

L	Length of planing hull (m)
B	Beam (m)
h	Depth of water (m)
U	Speed of the vessel (m/s).
g	Gravitational acceleration (m/s^2)
R_T	Total resistance (N)
R_V	Viscous resistance (N)
R_A	Air resistance (N)
R_S	Spray rail resistance (N)
R_M	Wave making resistance (N)
L_F	Lift force (N)
F_n	Froude number $F_n = U/\sqrt{g * L}$
Cv	Beam Froude number, $Cv = U/\sqrt{g * b}$
F_h	Depth Froude number$F_h = U/\sqrt{g * h}$
P	Pressure (N/m^2)
t_w	Sheer stress (N/m^2)
C_f	Frictional resistance
V	Speed of a wave (m/s)
Lc	Chine wetted length (m)
L_K	Length of the keel (m)
N	Dynamic normal force (N)
$C_{L\beta}$	Lift coefficient
C_{L0}	Lift coefficients atβ = 0◦
$F_{L\beta}$	Lift force (N)
F_{L0}	Lift force at β= 0◦

Greek Symbols

α	Kliven angle (degree)
β	Deadrise angle (degree)
ρ	The density of the fluid (kg/m^3)
τ	Trim angle of planing hull (radian).
v	Kinematic viscosity (m^2/s)
λw	Mean wetted length-to-beam ratio, $\lambda w = 0.5(L_C+L_K/B)$, Taken rang $\lambda w \leq 4$.
τ_{deg}	The trim angle of the planing hull (degree) take rang 2◦≤ τ_{deg}≤ 15◦

Abbreviation

FDM	Finite Different Method
FVM	Finite Volume Method
FEM	Finite Element Method
BEM	Boundary Element Method
2D	Tow dimension
3D	Three dimensions
VOF	Volume of Fluid
CFD	Computational Fluid Dynamic
RANSE	Reynolds Navier Stokes Equation
ACV	Air Cushion Vehicles
SES	Surface-Effect Ships
SWATH	Small water-plane-area twin-hull
ITTC	International Towing Tank Conference
PDE	Partial Differential Equation
DNS	Direct Numerical Simulation
SPH	Smoothed Particle Hydrodynamics

NASS
NAN YANG ACADEMY OF SCIENCES

Tel:+65 65881289
E-mail:contact@nassg.org
Add:12 Eu Tong Sen Street #07-169 Singapore 059819

ISSN 2661-3158
01
9 772661 315212